ALMA MATER STUDIORUM · UNIVERSITÀ DI BOLOGNA

Scuola di Scienze
Corso di Laurea Magistrale in Fisica

Nano-scale morphological and electrical characterization of nc-SiO_xN_y thin layers for photovoltaic applications

Relatore:	**Presentata da:**
Prof.ssa Daniela Cavalcoli	**Maria Antonietta Fazio**

Correlatore:
Dott.ssa Martina Perani

Anno accademico 2014/2015
Sessione II

Contents

Abstract

Il presente lavoro di tesi propone uno studio approfondito di proprietà morfologiche e di trasporto di carica di film sottili di $\mathrm{SiO_xN_y}$ amorfi (a-$\mathrm{SiO_xN_y}$) e nanocristallini (nc-$\mathrm{SiO_xN_y}$) che trovano importanti applicazioni in celle fotovoltaiche ad eterogiunzione in Silicio. Queste celle sono interessanti in quanto presentano l'efficienza massima tra le celle al Si (intorno al 25%), utilizzando un materiale facilmente reperibile e a basso costo. Lo studio è condotto mediante caratterizzazione elettrica e morfologica attraverso tecniche di microscopia a forza atomica (AFM).

Per quanto riguarda il materiale amorfo (a-$\mathrm{SiO_xN_y}$), sono stati studiati campioni cresciuti con tecnica PECVD (Plasma Enhanced Chemical Vapor Deposition), in cui è stata variata unicamente la distanza tra gli elettrodi durante la deposizione. Infatti, da studi recenti, è stata verificata una correlazione tra la distanza dagli elettrodi, il tipo di crescita e le qualità passivanti di questi materiali.

Per quanto riguarda il materiale nanocristallino, sono stati studiati campioni di nc-$\mathrm{SiO_xN_y}$, cresciuti con PECVD con una differente percentuale di $\mathrm{N_2O}$ come gas precursore e un differente tempo di annealing, dato che queste condizioni di crescita sembrano influenzare sensibilmente proprietà ottiche ed elettroniche.

In entrambi i casi si tratta di un materiale innovativo, le cui proprietà fisiche di base, nonostante le numerose recenti applicazioni, sono ancora poco studiate, visto che il materiale presenta fasi amorfe e cristalline e possibili formazioni di clusters e/o inclusioni di N e O.

L'analisi morfologica, condotta mediante microscopia a forza atomica (AFM) e successiva analisi statistica delle immagini, ha permesso di determinare alcune grandezze quali la lunghezza di correlazione laterale, la rugosità superficiale e il diametro medio dei grani. L'analisi statistica è stata validata controllando la possibile presenza di errori sistematici dovuti all'applicazione del software di analisi dati. Questo metodo di analisi si è dimostrato stabile e consistente per lo studio di questo tipo di strutture, in quanto errori sistematici dell'ordine del 5% contribuiscono per meno del 4%

all'errore sul valore della grandezza stimata.

Lo studio delle proprietà di trasporto è stato condotto mediante acquisizione di mappe di corrente a polarizzazione costante (tecnica conductive-AFM, c-AFM). In questo modo si è ottenuta una mappa di conducibilità locale, con risoluzione nanometrica, che permette di comprendere come avviene il meccanismo di trasporto nel materiale, che ruolo hanno fasi e grani cristallini e la concentrazione di O e N nel processo di trasporto.

Per quanto riguarda i materiali amorfi analizzati, i risultati hanno mostrato che la distanza tra gli elettrodi in fase di deposizione PECVD produce delle modifiche nella superficie dei campioni analizzati. La lunghezza di correlazione dei campioni a-$\mathrm{SiO_xN_y}$ varia tra 11.1 e 12.5 nm, il diametro medio dei grani misurati varia tra 7.8 e 8.0 nm ed infine la rugosità superficiale ottenuta è molto bassa ($\sim$0.85 nm).

Per quanto riguarda i campioni nanocristallini nc-$\mathrm{SiO_xN_y}$, si è ottenuto che il processo di annealing causa variazioni delle strutture superficiali. Infatti tempi di annealing crescenti provocano sia un incremento della grandezza dei grani, con un diametro che varia tra 16.4 e 19.3 nm, sia una variazione del clustering dei grani, raggiungendo una lunghezza di correlazione di 26.6 nm. La rugosità superficiale rimane pressochè invariata in un range da 0.87 a 0.90.

Dallo studio della conducibilità elettrica alla nanoscala si evince inoltre che i campioni non sono omogenei a queste scale. Sia i campioni amorfi che quelli nanocristallini, infatti, mostrano conducibilità locali, che derivano da differenze nella composizione o nella fase (amorfa/cristallina). I materiali di nc-$\mathrm{SiO_xN_y}$ con minore percentuale di $\mathrm{N_2O}$ durante la fase di deposizione presentano valori di conduttanza locale più grandi, il cui massimo raggiunge $1 \cdot 10^{-7}$ S, sia rispetto ai campioni amorfi sia rispetto a campioni cresciuti con una più alta percentuale di $\mathrm{N_2O}$ come gas precursore. L'introduzione di una quantità ridotta di $\mathrm{N_2O}$ nella fase di deposizione e il successivo processo di annealing generano una disuniformità nella distribuzione della conducibilità superficiale, con la presenza di alcuni grani fortemente conduttivi immersi in un insieme di grani caratterizzati da una conducibilità molto più bassa. Allo stesso tempo, un campione con queste caratteristiche presenta un comportamento maggiormente simmetrico con l'applicazione di voltaggi sia positivi che negativi.

L'analisi di questo materiale mediante tecniche a microscopia di sonda ha permesso di evidenziare che l'annealing produce nei materiali nanocristallini sia un clustering della struttura osservabile dall'aumento delle dimensioni dei grani, sia un significativo aumento della conducibilità locale del materiale. Inoltre la distanza tra gli elettrodi in fase di deposizione ha un effetto sulle proprietà morfologiche con un leggero aumento delle dimensioni dei grani. È da notare inoltre che su questi campioni si sono osservate variazioni locali della conducibilità alla nanoscala. I metodi utilizzati ci hanno permesso di condurre un'analisi accurata delle proprietà dei materiali studiati che porterà ad una comprensione più approfondita delle loro proprietà morfologiche e di trasporto elettronico.

Introduction

According to scientists, human activity is the dominant cause of global warming since the middle of the 20th century [1]. Due to the heavy development of industrialization, climate changes are mostly induced by land usage and by greenhouse gases (GHGs) emissions [2]. If not reduced, the increasing concentration of these gases in the atmosphere will lead to catastrophic scenarios, with a warming trend of air and oceans water temperature, as well as a shrink of the Arctic ice coverage [3]. In particular, electrical power production is one of the main activities which generates the largest part of humanity's fossil fuel derived GHGs emissions.

Within this framework, a development in the renewable energies field, considered the best alternative to fossil fuels for energy production, is necessary. Among all the available renewable energy sources, photovoltaics is one of the widest and most promising, as solar energy is free, widely distributed over the Earth and drives to a low release of pollutants. Moreover, solar cells technology is nowadays easily available, can be installed piecemeal with the highest job-generating potential among the other solar technologies [4, 5].

Actual research on solar cells is focused on efficiency improving, as well as cost reduction and optimization of production processes feasible at commercial and industrial scale. From the 1970s, crystalline silicon (c-Si) technology has controlled almost the 90% of the whole photovoltaic market, since silicon is abundant, non-toxic and stable material, with well-known physical properties due to its huge application in microelectronic field [6]. In order to further reduce costs and better use the solar spectrum, heterojunction solar cells with thin films were produced. These devices are based on the concept of multi-junction, with layers of different band gap materials stacked together [7]. The record efficiency of 25.6% was reached by a Si Heterojunction (SHJ) with Intrinsic Thin layer for a cell of practical size in 2014 [8]. In SHJ solar cells a doped amorphous silicon layer (a-Si:H) is deposited on top of the crystalline silicon (c-Si) active material, in order to create the electric field of the pn junction [6]. Due to a reduction of the layer thickness, additional passivation layers of intrinsic a-Si:H are introduced in these devices between the absorber and the emitter layers to avoid surface recombination. Notwithstanding the good passivation qualities of *a*-Si:H, carriers with short lifetime are generated in this material and a large fraction of them recombine, causing a high parasitic light absorption [9].

Within thin-films solar cells technology, silicon oxy-nitride ($\mathrm{SiO_xN_y}$) turned out to be a promising material as a substitute for *a*-Si:H in the role of window layer or intermediate reflector in SHJ solar cells [10, 11]. It has already been shown that the employment of amorphous silicon oxide (a-$\mathrm{SiO_x}$) or amorphous $\mathrm{SiO_xN_y}$ (*a*-$\mathrm{SiO_xN_y}$) as emitter layers in SHJ solar cells can lead to a further increase of the solar cell efficiency [12, 9]. Indeed, the substitution of a-Si:H with $\mathrm{SiO_xN_y}$ leads to a reduction of the parasitic absorption in the emitter layer, due to its higher band gap. An additional efficiency gain can be expected introducing nanocrystalline $\mathrm{SiO_xN_y}$ (nc-$\mathrm{SiO_xN_y}$) as the doped layer in the emitter stack, for its high conductivity and low resistance with the anti-reflecting coating above it [13].

Notwithstanding those promising properties, the structure of these materials is complex due to the coexistence of different phases and compositions, and many issues on the correlation between deposition conditions and the material properties have not been studied yet.

This thesis aims to investigate various samples of both *a*- and nc-$\mathrm{SiO_xN_y}$ thin layers in their morphological and electrical properties at the nano-scale with AFM and conductive-AFM techniques. A study of the statistical errors due to an incorrect parameter setup for morphological analysis has been driven, to confirm the consistency of the method for the statistical analyses and extraction of morphological parameters. The effects of the oxygen incorporation during the deposition and of the annealing on the nc-$\mathrm{SiO_xN_y}$ thin films properties have been studied. Moreover, a series of *a*-$\mathrm{SiO_xN_y}$ samples with different electrode distances during the deposition have been investigated.

The outline of the thesis is the following: in Chapter 1 the energy problem and the need for renewable energy production is introduced; then, the working principles and the state of the art of photovoltaics are described, leading to the structure of SHJ solar cells. The initial part of Chapter 2 is focused on the samples description and its known properties, while various AFM techniques and strategies used for the morphological and electrical analysis is deeply illustrated in the second part. In Chapter 3 the results of all the measurements on different samples are described, for nc- and *a*-$\mathrm{SiO_xN_y}$ thin layers, respectively. Finally, a discussion and some conclusions about the obtained results are presented.

Chapter 1

Photovoltaics: an Introduction

1.1 A challenge for renewable energies

Human activity is regarded as the dominant cause of global warming since the middle of the 20th century, due to the heavy development of industrialization. Human influence on the climate system is extensively growing, causing effects across all continents and oceans. The Fifth Assessment Report (AR5) of the Intergovernmental Panel on Climate Change (IPCC) shows that the more human activities disrupt the climate, the greater will be the risks of critical and irreversible effects for people and ecosystems, and of long-lasting changes in the climate system [1].

Global warming has lead to a rise in the atmosphere and ocean temperatures and to a reduction of the amounts of snow and ice, promoting an increase of the sea level. In fact, the Earth's surface has been progressively warmer in the last three decades than any preceding decade since 1850. Multiple independently existing datasets have shown a warming of 0.85 ℃ (from 0.65 to 1.06 ℃) of the globally averaged combined land and ocean surface temperature over the period 1880-2012. Figure 1.1(a) points out an ascending linear trend of Earth's mean surface temperature over the last 60 years, while Figure 1.1(b) shows the observed change in surface temperature in 1901-2012. Moreover, near the surface, the ocean warmed by 0.11 ℃ (from 0.09 to 0.13 ℃) per decade between 1971 and 2010. In addition, the industrial era has brought to a heavy acidification of the ocean, due to an increase of the concentration of carbon dioxide. The pH of the ocean water close to the surface has decreased by 0.1, which corresponds to an acidity increased of 26%. Moreover, during the last century, the shrink of the glaciers has been causing a rise of the sea level. While in Antartica there are regions in which ice extent rises and diminishes, in the Artic area the amount has decreased in

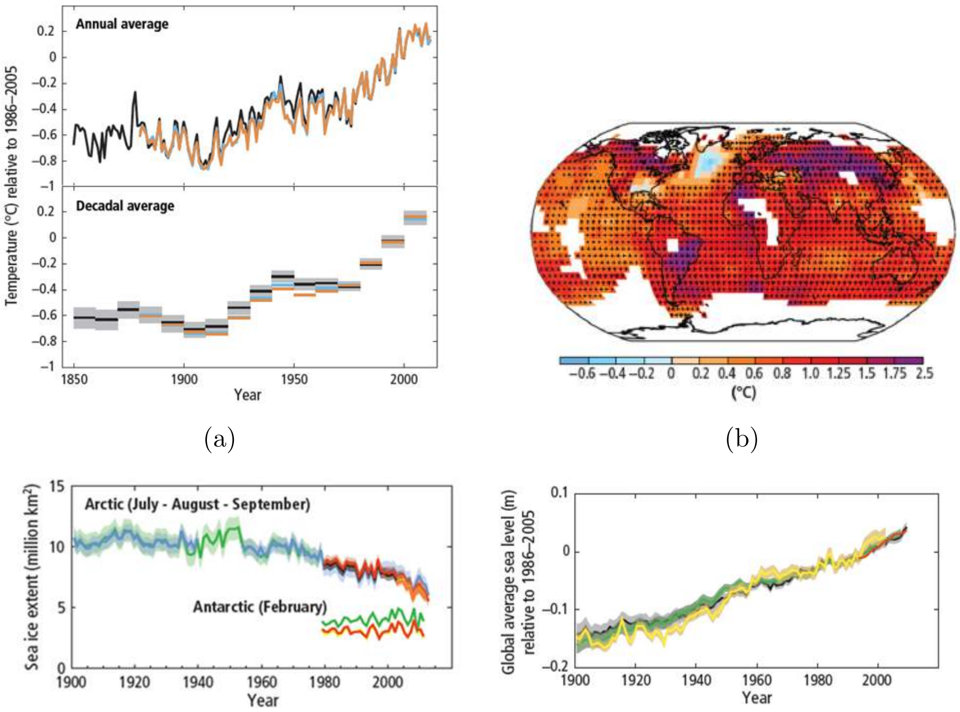

(a) (b)

(c) (d)

Figure 1.1: a) Observed globally averaged combined land and ocean surface temperature anomaly 1850-2012 as annual and decadal averages (grey shading indicates the decadal mean uncertainty). b) Observed change in surface temperature 1901-2012. Grid boxes where the trend is significant, at the 10% level, are indicated by a + sign. c) Arctic (July to September average) and Antarctic (February) sea ice extent. d) Global mean sea level relative to the 1986-2005 [1].

every season and in every successive decade since 1979. For the summer sea ice minimum, the decrease ranged from 0.73 to 1.07 million km^2 per decade (Figure 1.1(c)). At last, in the past 50 years, the rate of sea level rise has been faster than the mean rate of the previous two millennia. Figure 1.1(d) presents the global mean sea rise by 0.19 m over the period from 1901 to 2010 [1].

Changes in the ecosystem, which are strictly correlated with extreme climate changes, are mostly induced by land usage, i.e. deforestation, which modifies Earth surface reflectivity, and by greenhouse gases (GHGs) emissions [2]. These gases allow direct sunlight (visible and ultraviolet portion) to freely reach Earth's surface, whereas they absorb and re-emit infrared radiation towards the atmosphere, 'trapping' heat in its lower part. Many

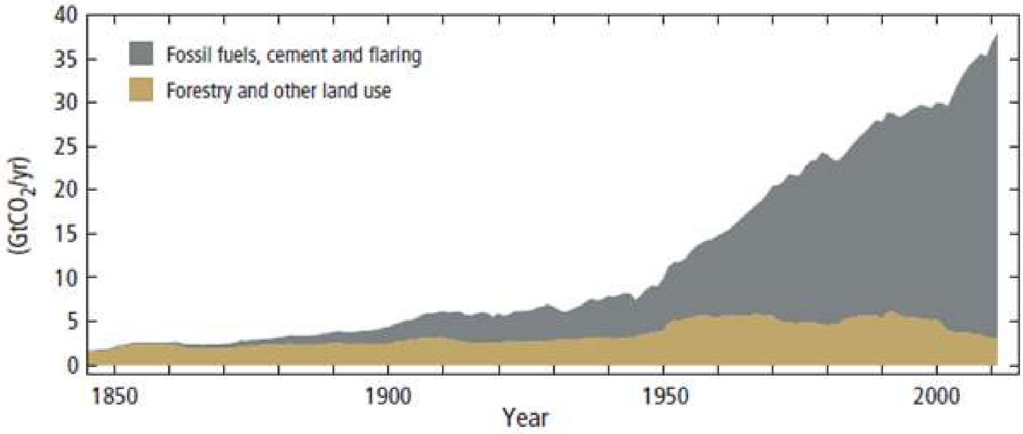

Figure 1.2: Global anthropogenic CO_2 emissions in gigatonne of CO_2-equivalent (CO_2eq) per year [1].

greenhouse gases are naturally present in the atmosphere, such as carbon dioxide (CO_2), methane (CH_4), water vapor and nitrous oxide (N_2O), while others are synthetic [14]. Since 1750, atmospheric concentrations of CO_2, CH_4 and N_2O incremented of 40%, 150% and 20% respectively. Between 1750 and 2011, (2040 ± 310) Gt of CO_2 have been emitted by anthropogenic source. The 40% of this amount has remained in the atmosphere, while the 30% has been absorbed by the oceans, causing a greater acidification. Figure 1.2 indicates the trend of global anthropogenic emissions from different sources [1].

If not reduced, GHGs will create catastrophic scenarios, also in the short term (up to 2035) [3]. The warming trend of air and oceans water temperature, as well as a further shrink of the Arctic ice coverage, will lead to the extinction of several terrestrial and marine species and the degradation of the whole ecosystem [1]. It is an ethical duty for international governments to manage a way out of these catastrophic consequences, reducing human GHGs emissions. Atmospheric GHGs concentrations would need to range between 445-490 ppm CO_2eq in the atmosphere, to achieve an equilibrium global temperature increase of only 2 ℃ to 2.4 ℃ with respect to pre-industrial values (CO_2-equivalent measures the emissions of a given GHG, using CO_2 emissions as a reference). This implies a decrease of global emissions of CO_2 by 50 to 85% below 2000 levels, starting no later than 2015 [5].

One of the main activities which contributes to the increased generation of GHGs is electrical power production. With its 18 000 TWh per year, it leads to the formation of 10 gigatonnes of carbon dioxide, the largest part of humanity's fossil-fuel derived emissions. One way to reduce this damaging situation, without ignoring the increasing electrical request, is the use of renewable energies (RE) [4]. This would be a good choice for both meeting basic human energetic needs and providing low environmental impacts and low GHGs emissions. RE represent any form of energy from solar, geophysical or biological sources, replenished by natural processes at a rate equal or faster than its rate of use. RE include resources such as biomass, solar energy, geothermal heat, hydropower, tide and waves, ocean thermal energy and wind energy. Of the approximate 300 GW of the new electricity generated globally from 2008 to 2009, 140 GW came from RE additions [5].

1.2 Photovoltaics: a brief review

Among the four major types of direct solar energy technologies (solar thermal, photovoltaic, concentrating solar power, solar fuels), photovoltaics (PV) represents the production of electricity via direct conversion of the solar energy through the use of photovoltaic cells.

The increase in manufacturing capacity and the dropping of the costs have led to a remarkable growth in the PV industry during the first years of the 21st century. From a power of 550 MW of cells installed worldwide in 2002, after five years the values had increased six times [4]. In 2009, solar cell production reached about 11.5 GW per year: China accounted for $\sim 51\%$ of world production, Europe about 18%, Japan about 14% and the USA about 5% [5].

Apart from GHGs reduction, the employment of solar energy drives to a lower release of pollutants, such as particulates and noxious gases, with respect to fossil fuel factories. Electricity production, with solar thermal and PV technologies, does not generate any type of solid, liquid or gaseous by-products. In this perspective, solar cells fabrication has a reduced environmental impact, especially in solar home systems [5]. In fact, a great advantage of PV is its possibility of being installed piecemeal, house by house and business by business [4]. Moreover, in those communities in which a connection to a main grid would be cost prohibited, solar home systems and local PV-powered community grids can provide low-cost electricity. Supported by a wide public acceptance, solar PV holds also the highest job-generating potential among the family of solar technologies [5]. PV module materials can be recycled and reused and during their lifetime do not require any kind of maintenance. PV energy payback time, which represents the time needed by the module to produce the same quantity of energy spent for its production, is very short; from one-and-a-half to three years in 2006, it could reach values of 0.5 years by 2020 [15, 16].

The price for PV modules dropped from USD_{2005} 22/W in 1980 to less than USD_{2005} 1.50/W in 2010s [5]. The costs for installation are not included in these estimations; indeed, the price to build a full system reaches normally about twice the price of the cells [4]. However, the price in USD/W for an entire system, including the module, the balance of systems (BOS, which comprises inverters, storage, charge controllers, system structures and energy network) and installation costs, has also decreased steadily, reaching values of USD_{2005} 2.72/W for some thin-film technologies by 2009. According to the European Strategic Energy Technology Plan (SET-Plan), intensifying research and development (R&D) and demonstration activities can help reducing significantly the cost of all low carbon energy technologies, up to 30-80% from current levels by 2050. Figure 1.3(a) shows a steeper projected drop in the costs of PV utilities up to 2020, making it the cheapest RE source. Diversified Supply Technologies (DST) scenarios predict reduced capital costs of power generation technologies, as a consequence of the impact of research, development, innovation and capital investments on the decarbonized energy systems (Figure 1.3(b)) [17].

Research along the whole PV production chain, from raw material processing, cell and module manufacturing to power electronics and system integration including local storage options, is needed in order to improve the cost competitiveness of the European PV industry. In the last few years, the research in PV devices has seen major advances in efficiency, reliability and reproducibility; for a further progress, additional steps are still to be done in understanding material properties and fabrication processes. A fundamental role is performed by supporting a development in every different aspect of PV module fabrication, i.e. efficiency, stability, lifetime, high productivity manufacturing, environmental sustainability and applicability [17]. Built PV modules have an estimated lifetime of 30 years, promising a great long-term performance (over the 80% of the initial performance after 25 years) [15].

Nowadays, PV cells are made of both organic or inorganic materials. Inorganic cells are based on silicon or non-silicon technology and are classified as wafer-based cells or thin-film cells. Wafer-based silicon modules can be of two different types: monocrystalline and multicrystalline (sometimes called "polycrystalline").

Until now, various PV technologies have been developed in parallel. Commercially available PV technologies include wafer-based crystalline silicon PV, as well as the thin-film technologies of copper indium/gallium disulfide/(di) selenide (CIGS), cadmium telluride (CdTe), thin-film silicon (amorphous and microcrystalline silicon) and dye-sensitized solar cells [5]. In 2009, silicon-based solar cells and modules represented about 80% of the worldwide

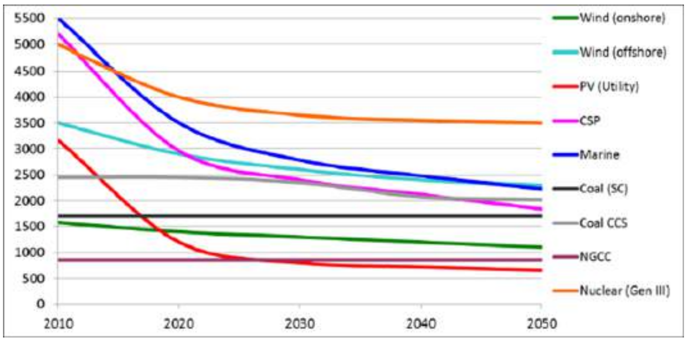

(a)

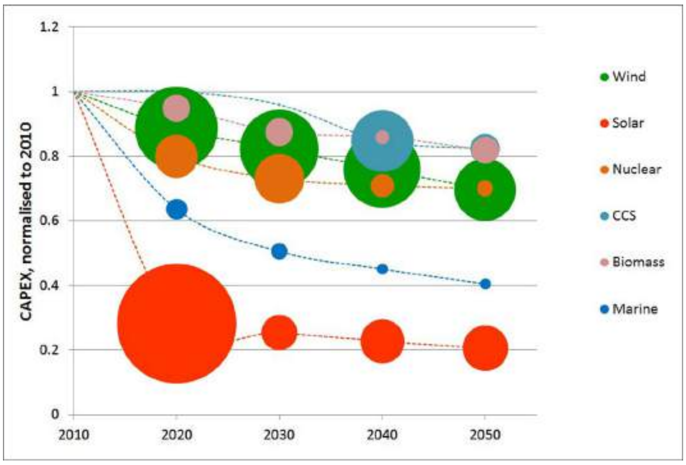

(b)

Figure 1.3: a) Trends in capital costs of selected energy technologies (€/kW). b) Reduction of capital costs of power generation technologies compared with those of 2010. The disc size indicates the savings achieved by the reduction of capital costs of each technology per decade [17].

market, while the remaining 20% mostly included cadmium telluride, amorphous silicon and CIGS solar cells [5]. From the 1970s, crystalline silicon (c-Si) has controlled almost the 90% of the whole photovoltaic market. This trend derives from peculiar characteristics of this material: it is abundant (the second most abundant material in the Earth's mass), non-toxic and stable, with well-known physical properties. In addition, its extraordinary success in microelectronic field brought to an expert and mature technology [6].

Although today direct solar energy provides only a small fraction of the world energy supply, it remains the energy source with the wider potential future perspectives [5].

1.3 Single junction solar cells: working principles and definitions

Solar cells convert sunlight directly into electrical power employing the electrical properties of materials known as semiconductors (for example silicon), by photovoltaic effect. The first scientist who observed a light-dependent voltage between electrodes immersed in an electrolyte was Alexandre-Edmond Becquerel (Paris, March 24, 1820 - May 11, 1891) in 1839. After attempts with selenium and cuprous oxide solar cells during the 19th century, a first silicon cell was reported in 1941, even though a device with reasonable efficiency was not announced until 1954 [18]. It was reported by Daryl Chapin, Calvin S. Fuller and Gerald Pearson and converted sunlight with an efficiency of 6% [19]. The first application of these cells was as a power source in spacecrafts from 1958 and this remained its major employment over the following decade [18]. In the 1950s, there was the discovery of a way to manufacture p-n junctions in silicon, that turned out to have better rectifying properties and PV behavior than the Schottky barriers used in the 19th century [19]. In the early 1970s, because of a fruitful period of silicon cells development and the energetic crisis of the oil-dependent western world, there was a rebirth of interest in its terrestrial use [18].

1.3.1 The Sun as a power source

As PV power source, sunlight is an unlimited, free and widely distributed fuel reaching the Earth surface with a power of 10^5 TW [20]. The Sun can be approximated to a black-body (perfect emitter and absorber of electromagnetic radiation) and its spectral distribution of emission follows Planck's radiation law; according to this law, as temperature rises, there is an increase in emitted radiation with a peak emission shift towards shorter wavelengths (Figure 1.4) [18].

Although temperatures can reach $2 \cdot 10^7$ K near the Sun's center, Sun can be modelled as a 6000 K black-body from an Earth perspective. This is due to the absorption of most radiation by its external layer of negative hydrogen ions. The radiant power per unit area perpendicular to the direction Sun-Earth before light enters the atmosphere is called "solar constant" or "air mass zero" (AM0) radiation and is essentially a constant parameter (1353 kW/m^2). Figure 1.5 exhibits the differences between an ideal black-body and AM0 radiation (two upper curves), because of the different transmissivity of the Sun's atmosphere at different frequencies. Solar cells response varies with wavelengths, therefore a thorough knowledge of the distribution of energy in

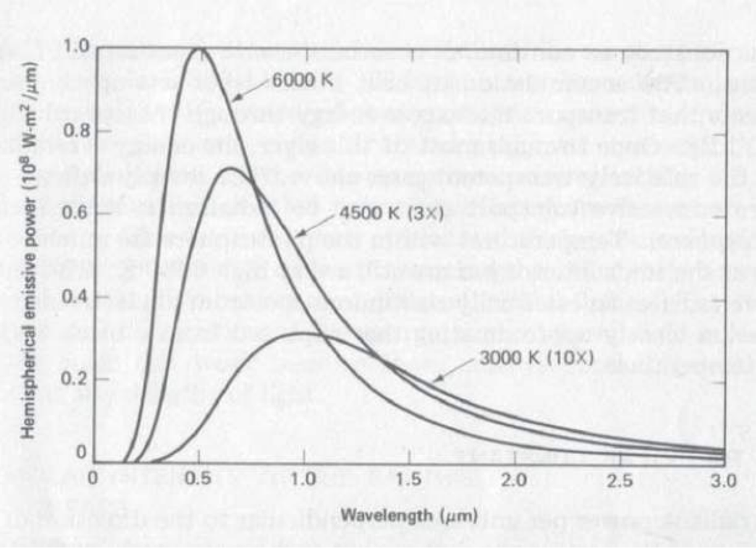

Figure 1.4: Black-body radiation distributions at different temperatures [18].

sunlight is mandatory. Earth's atmosphere causes a sunlight attenuation of over the 30%, due to scattering and absorption events by its constituent gases and particles. The lower curve in Figure 1.5 represents a typical sunlight radiation which reaches the Earth surface. The spectral distribution depends on the ray's path length. The shortest is the one with the Sun directly at the zenith and it is associated with an "air mass one" (AM1) radiation. At an angle θ respect to the zenith, the air mass is given by:

$$Air\ mass = \frac{1}{\cos\theta} \tag{1.1}$$

Because of the great variability of terrestrial light, in 1977 AM1.5 was chosen as its standard, for a total power density content of 1 kW/m^2 (Figure 1.5) [18].

An important component of sunlight is its diffuse part, which represents from 10-20% in clear and cloudless skies to nearly the whole total radiation at the surface during days with a notable lack of sunshine. This emission is characterized by a spectrum richer in the shorter wavelengths, contributing to further changes in the spectral composition [18].

The energy of visible photons can be large enough to promote electrons in semiconductors up to conduction band, where they are free to move. After excitation, the electrons quickly recombine. In PV devices there is a built-in electric field which separates electrons from holes before they recombine, giving birth to a potential difference. If the device is connected to a load, this force drives the electrons, producing electrical work. The efficiency of a

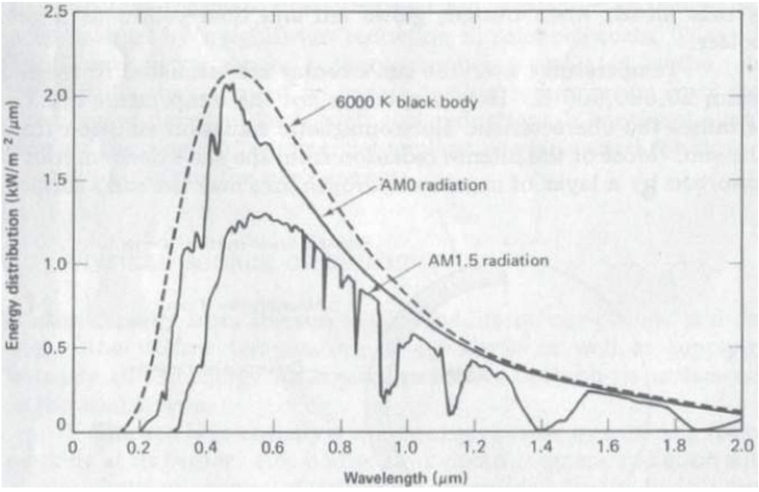

Figure 1.5: Spectral distribution of sunlight, diversifying 6000 K black-body, AM0 and AM1.5 radiation [18].

solar cell depends on the choice of the absorbing material and of the external circuit.

1.3.2 Circuital characteristics and definitions of a solar cell

As the basic structure in a PV system, the solar cell can be considered as a two terminal device acting like a diode in the dark and producing photovoltage when illuminated by the Sun. The surface is treated to reduce the reflected visible light as much as possible. A pattern of metal contacts is imprinted on the surface in order to create electrical contacts. Not loaded, a common basic unit generates a DC photovoltage of 0.5 - 1 V when illuminated by the Sun; whereas in short circuit conditions photocurrent reaches some tens of mA/cm^2. Because of the low voltage created, to produce useful DC voltages, the cells are connected in series and encapsulated into modules (28 - 36 cells for 12 V). Different modules are usually connected in parallel or in series into arrays. A change in the illumination during the day forces the presence of a charge storage system [19].

The solar cell, illuminated by light, can be seen as a battery in a simple electronic circuit. The voltage developed with isolated terminals is defined as open circuit voltage V_{oc}. The current created when the terminals are connected together is defined as the short circuit current I_{sc}. When an intermediate load resistance R_{L} is introduced, the voltage developed ranges between 0 and V_{oc}, with the current $I(V)$ determined by the current-voltage characteristic of the cell under illumination. The short circuit current density J_{sc} is an useful parameter to compare different cells [19]. In order to achieve better performances of the PV device, it is necessary to maximize both J_{sc} and V_{oc}. To obtain high values of J_{sc}, the material should have high minority carrier lifetime, high mobility and absorption over a wide range of wavelengths, whereas V_{oc} is linked to the band gap of the material and to the kind of transport mechanism involved [21]. J_{sc} depends on the incident light through the cell's quantum efficiency $QE(E)$, that is the probability of an incident photon of energy E to deliver one electron to the external circuit, that is:

$$J_{\mathrm{sc}} = q \int b_{\mathrm{s}}(E) QE(E) dE \tag{1.2}$$

where b_{s} is the number of photons of energy between E and $E + dE$ incident to an unit area in a unit time and q is the electronic charge. QE is the best quantity to judge solar cell performance under different conditions, because it does not depend on the incident spectrum [19].

A solar cell has the same behavior of a p-n junction, when not illuminated; therefore, free carriers transport constitutes the dark current density J_{dark} under an applied bias V, which flows in the opposite direction with respect to the photocurrent and follows an exponential law:

$$J_{\mathrm{dark}}(V) = J_{\mathrm{o}}(e^{q\mathrm{V}/Ak_{\mathrm{B}}\mathrm{T}} - 1) \tag{1.3}$$

where J_{o} is the reverse saturation current of the diode, A is the ideality factor, k_{B} is Boltzmann's constant and T is the temperature. The net current can be approximated as the sum of the short circuit photocurrent and the dark current (superposition approximation). The net current density $J(V)$ is:

$$J(V) = J_{\mathrm{dark}}(V) - J_{\mathrm{sc}} \tag{1.4}$$

with the sign of the photocurrent taken conventionally negative and $J_{\mathrm{dark}}(V)$ given by Equation 1.3. The open circuit voltage V_{oc} is the voltage at the contacts when photocurrent and dark current exactly cancel out:

$$V_{\mathrm{oc}} = \frac{Ak_{\mathrm{B}}\mathrm{T}}{q} \ln\left(\frac{J_{\mathrm{sc}}}{J_{\mathrm{o}}} + 1\right) \tag{1.5}$$

so it increases logarithmically with light intensity [19]. Figure 1.6 illustrates typical idealized characteristic curves $J(V)$ both in the dark and under illumination [21].

With respect to its circuital properties, a solar cell is equivalent to a current generator in parallel with an asymmetric non linear resistive element,

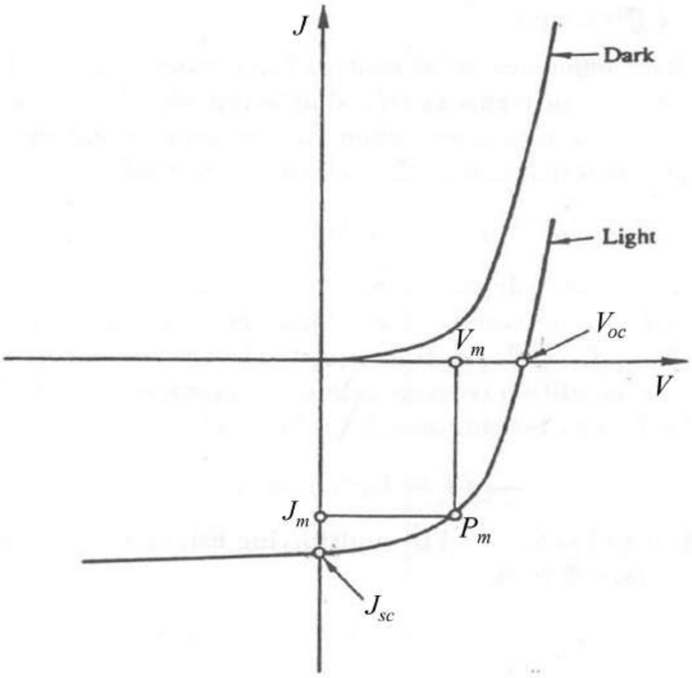

Figure 1.6: Characteristic curves of net current density charged by light and in the dark versus voltage for a solar cell. Plots adapted from [21].

i.e. a diode, as shown in Figure 1.7(a). The operating range of the solar cell is from 0 to V_{oc}. In this regime the cell delivers a power density of:

$$P = JV \tag{1.6}$$

The maximum value of P is reached at the cell's operating point, at some voltage V_{m} and a current density J_{m} (Figure 1.6). The "squareness" of the $J-V$ curve is described by the fill factor FF:

$$FF = \frac{J_{\mathrm{m}}V_{\mathrm{m}}}{J_{\mathrm{sc}}V_{\mathrm{oc}}} \tag{1.7}$$

The efficiency η is defined as the ratio between the power density generated at operating point and the incident light power density P_{rad}:

$$\eta = \frac{J_{\mathrm{m}}V_{\mathrm{m}}}{P_{\mathrm{rad}}} \tag{1.8}$$

Short circuit current density, open circuit voltage, fill factor and efficiency represent the performance characteristics of a solar cell under a particular illumination condition [19].

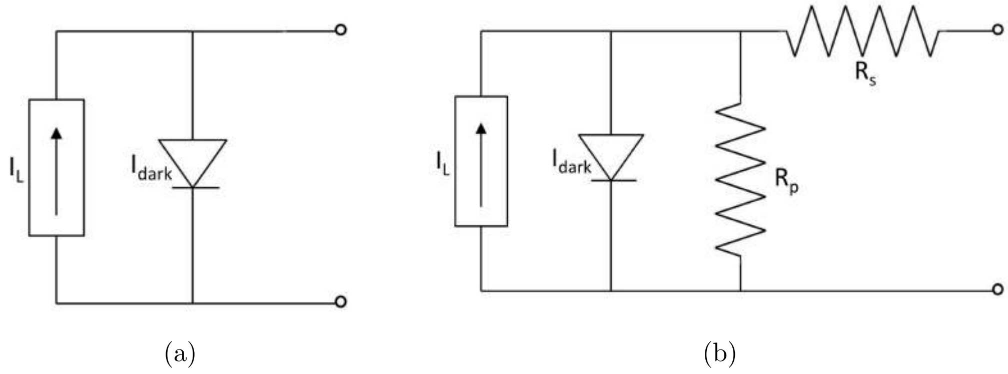

(a) (b)

Figure 1.7: a) Equivalent circuit of an ideal solar cell [19]. b) Schematic view of the equivalent circuit of a real solar cell [21].

The equivalent circuit for a real solar cell is depicted in Figure 1.7(b); power dissipation is due to the resistance of the contacts and to leakage currents around the sides. These effects can be summarized considering the presence of parasitic resistances in series (R_s) and in parallel (R_p). This non ideal behavior causes a reduction of the fill factor [19].

A photoconverter should have the following properties in order to be more efficient as possible.

i. First of all, the energy gap E_g of the material used as absorber should be high enough to avoid easy recombination events, but also not too wide, in order to exploit incident photons of various energies to promote carriers [21].

ii. Secondly, in order to promote diffusion of the produced carriers before they recollect, the diffusion length of minority carriers has to be as large as possible. The value of this parameter is strictly correlated to the choice of the material of the solar cell [21].

iii. Moreover, to produce carriers within one diffusion length away from the junction with good chances to be accelerated by the electrical field at the interface and delivered in the external circuit, the absorbing layer has to be thinner with respect to the other portion of the junction (a few tens or hundreds of microns thick) [21].

iv. At last, to collect charges with less energetic losses as possible, the material should be a good electrical conductor. This means that carriers do not recombine at impurity levels and defect centers and do not transfer energy to the bulk. It is useful also to employ low resistance metal contacts, with an ohmic junction behavior [19].

1.3.3 Photogeneration and recombination processes in a doped semiconductor

In a solar cell, the photocurrent is determined by a balance between light absorption, charge generation and recombination. Transport in a semiconductor is dictated by two conservation laws. The first assumes that each type of carrier is conserved, that is for electrons:

$$\frac{\partial n}{\partial t} = \frac{1}{q}\nabla \cdot \mathbf{J}_{\mathrm{n}} + G_{\mathrm{n}} - U_{\mathrm{n}} \tag{1.9}$$

and for holes:

$$\frac{\partial p}{\partial t} = \frac{1}{q}\nabla \cdot \mathbf{J}_{\mathrm{p}} + G_{\mathrm{p}} - U_{\mathrm{p}} \tag{1.10}$$

where n/p is the electron/hole concentration, $G_{\mathrm{n/p}}$ is the volume rate of generation of electrons/holes, $\nabla \cdot \mathbf{J}_{\mathrm{n/p}}$ represents the spatial variation of the current densities and $U_{\mathrm{n/p}}$ is the volume rate of recombination. The second law is the Poisson's equation:

$$\nabla^2 \phi = \frac{q}{\epsilon_{\mathrm{s}}}\left(-\rho_{\mathrm{fixed}} + n - p\right) \tag{1.11}$$

where ϕ is the electrostatic potential due to the carriers charges, ϵ_{s} is the dielectic permittivity of the semiconductor and ρ_{fixed} represents the local density of the fixed charge [19].

Carrier generation is an electronic excitation event leading to an increase of the number of the carriers; it requires an energy input that could derive from phonons, photons, as well as from other carriers. It could promote an electron from the valence band or from a defect level in the band gap to the conduction band; the most important generation event in a solar cell is for sure an optical generation.

On the other hand, recombination reduces the number of the carriers; this process causes an energy release, due to an electron that loses energy and decays to a lower energy state. This results in an energy loss, for example through the emission of a photon (radiative recombination) or in the form of heat through phonon emission (non-radiative recombination). Auger recombination could also be present, resulting in the promotion of another carrier in a free state. According to the microscopic reversibility principle, every time a generation process occurs, an equivalent recombination process follows, and viceversa. At a finite temperature, thermal energy can stimulate both carrier generation (its transition from the valence band to a trapped level or to the conduction band) and recombination. These two situations are called *thermal generation* and *thermal recombination*, respectively. The rate of these processes increases as the temperature rises. Microscopically, with the approximation of the source of energy as a perturbative Hamiltonian and of a two-state transition, electronic excitement and decay follow Fermi's Golden Rule [19].

Photogeneration leads to the production of mobile carriers and it is the most important process in a semiconductor solar cell irradiated by such photons. Other optical processes are present such as free carrier absorption, phonons generation, promotion of an electron in a localized state and photon scattering. The first two events happen if the photon energy is much smaller than the band gap (<100 meV) and the first occurs only in a high carrier density system. When photons with energies close to the band gap are involved, band to band and defect state to band transitions are the most probable. Scattering is an undesirable process, caused by surfaces and inhomogeneities in the material, because it wastes light without generating any carrier. Photogeneration is represented as the current generator in the equivalent circuits of both ideal and real solar cells in Figures 1.7(a) and 1.7(b).

Macroscopically, absorption is described by means of the absorption coefficient α, that shows how a material attenuates light intensity during its path through it and can be considered as the sum of the absorption cross sections per unit volume of the different optical processes in the material. For a non-uniform material, at a depth x, the intensity $I(x)$ is given by:

$$I(x) = (1 - R(E)) I_{\mathrm{s}} e^{-\int_0^x \alpha(E,x')dx'} \tag{1.12}$$

where I_{s} is the incident light intensity and R is the normal reflectivity at the surface [19]. If α is uniform, then Equation 1.12 becomes the exponential Beer-Lambert law [19]. At depth x, the rate of carrier generation per unit volume is the following:

$$g(E,x) = (1 - R(E))\alpha(E) b_{\mathrm{s}}(E) e^{-\int_0^x \alpha(E,x')dx'} \tag{1.13}$$

where $b_{\mathrm{s}}(E)$ is the photon incident flux. To calculate the total generation rate, the value found in Equation 1.13 has to be integrated over all the photon energies. Photogeneration depends on the number of photons and not on their energy (it is important only that it exceeds band gap energy) [19]. The extra energy that a carrier absorbs is then lost through a process called *thermalization*, as can be seen in Figure 1.8 [19].

The absorption coefficient α dependence on the energy band gap E_{g} can be calculated and it is different in the cases of a direct or indirect gap semiconductor. If the bottom part of the conduction band occurs at the same momentum value k as the upper part of the valence band, then the semiconductor has a direct gap, as depicted in Figure 1.9(a). If the minimum and the

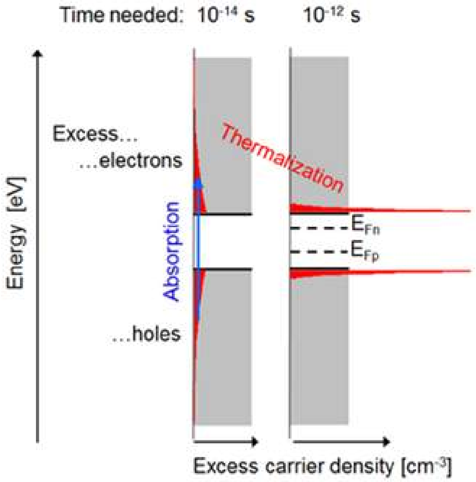

Figure 1.8: An example of absorption of a photon with energy higher than the band gap, followed by thermalization process (E_{Fp} and E_{Fn} are the quasi Fermi levels in the non-equilibrium situation) [22].

maximum are situated at different k values, the band gap is indirect, as in the case of silicon, and a carrier transition from the valence to the conduction band always involves a phonon, in order to conserve the crystal momentum (Figure 1.9(b)) [23].

While the absorption coefficient in a direct semiconductor reflects the shape of individual densities of states, following the rule:

$$\alpha(E) \propto (E - E_{\mathrm{g}})^{1/2} \tag{1.14}$$

the absorption coefficient in an indirect semiconductor has a very different behavior [19], that is:

$$\alpha(E) \propto (E - E_{\mathrm{g}})^{2} \tag{1.15}$$

As regards recombination, it can be divided into two categories: unavoidable and avoidable processes. The firsts result from optical generation, spontaneous and stimulated emission, as well as Auger recombination, while the seconds are transitions related to impurities and defects in the material [19].

Even if a large number of materials exhibits a photovoltaic behavior, there are not many materials that could achieve high efficiency (more than 20%) and stability at low cost [21].

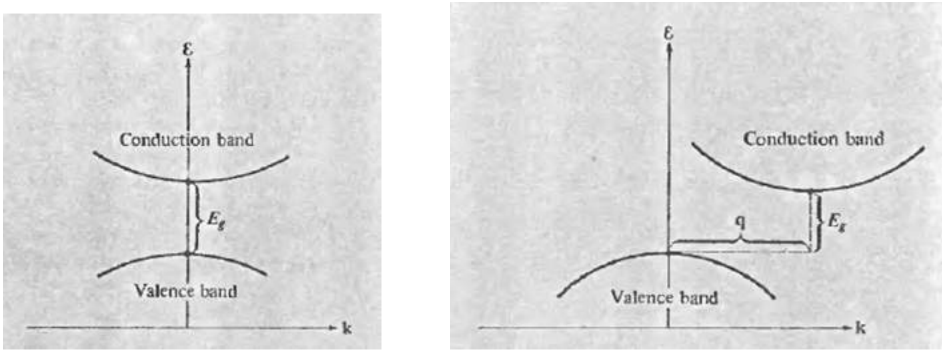

(a) (b)

Figure 1.9: Schematic view of a a) direct and b) indirect band gap semiconductor [23].

1.3.4 Homojunctions and heterojunctions

Among different types of single junction that can be produced, the following discussion is focused on two particular cases: homojunctions and heterojunctions.

A homojunction is made of two portions of the same semiconductor, one doped as a p-type and the other as an n-type. Since the work function $q\phi_W$, defined as the difference between the vacuum level E_{vac} and the Fermi level E_F of a semiconductor, is different in the two portions, the band bending generates an electric field at the junction. The typical shape of the bands in a homojunction is shown in Figure 1.10(a) [21]. The difference between the work functions of the two portions $(q\phi_{W_p} - q\phi_{W_n}) = q\phi_D$ is called diffusion potential; this potential is due to the attempt of the mobile carriers to equalize the Fermi level in the n- and p-type sides, depleting the n-type region near the junction from electrons and leaving fixed positive charges in it. Photoexcitation induces the generation of free minority carrier electrons in the p-type region and free minority carrier holes in the n-type region [21]. They diffuse toward the junction and, if they do not recombine with each other, they diffuse through the semiconductor reaching the external circuit. To promote diffusion, the illuminated part must be thin and it can reach very small thicknesses if the semiconductor has direct band gap. This property can be counter-productive since it introduces a great number of surface states, that can promote recombination between the mobile carriers. The fragile balance between both small thicknesses and recombination rates, underlines the importance of producing a material with well defined properties and structure and high quality [21].

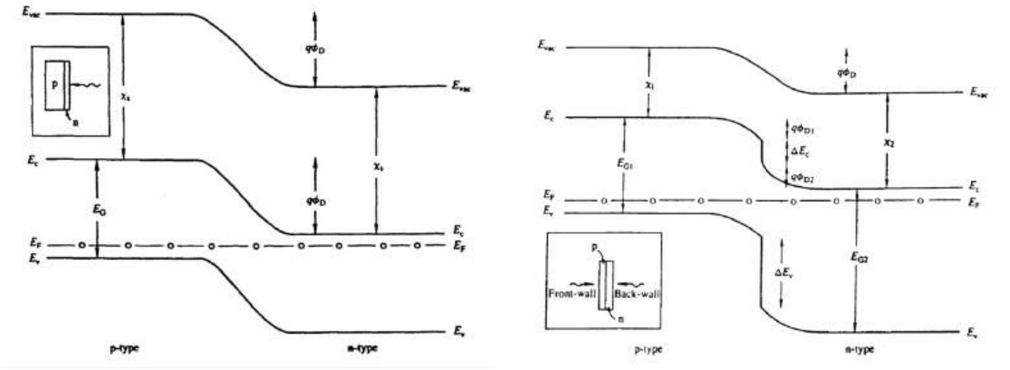

(a) (b)

Figure 1.10: a) Energy-band diagram of a p-n homojunction, with the same level of doping in the two portions (χ_s is the electron affinity). b) Energy-band diagram of a p-n heterojunction, with the same level of doping in the two portions, with the following choices: $\chi_1 < \chi_2$ and $E_{G1} < E_{G2}$ [21].

A heterojunction, on the other hand, is made of two materials, with different band gaps and electron affinities. In a semiconductor, electron affinity χ is the difference in energy between the vacuum level E_{vac} and the bottom of the conduction band E_{c} [24]. A typical band bending of a heterojunction, with the assumption that the energy gap of the p-type portion E_{G1} is smaller than that of the n-type E_{G2}, is described in Figure 1.10(b). According to the Anderson abrupt-junction model, all effects of interface dipoles and states are neglected and the differences between the band properties of the two materials determine only the presence of discontinuities in both conduction (ΔE_c) and valence (ΔE_v) bands [21]. The choice of $\chi_1 < \chi_2$ has been made in order to avoid spikes near the discontinuities, that could act as barriers in the electron transport. With respect to the homojunction, photoexcitation can occur both in the n- and p-type materials, called back- and front-wall, respectively. When there is a back-wall photoexcitation, the n-type semiconductor acts as a window layer which allows photons to penetrate in the junction with minimum losses [21]. Sometimes, to avoid or at least diminish junction currents that could cause a decrease of V_{oc}, an insulating layer is introduced between the semiconductors, giving birth to a Semiconductor-Insulator-Semiconductor (SIS) junction. This strategy is used in Heterojunctions with Intrinsic Thin layer (HIT$^{\text{TM}}$) solar cells, which will be described in Section 1.5 [6].

1.3.5 Shockley-Queisser limit

After various semiempirical calculations of an upper limit of efficiency for a single junction solar cell, in 1961 W. Shockley (London, February 13, 1910 - Stanford, August 12, 1989) and H. J. Queisser (Berlin, July 6, 1931) derived the first theoretical limit, known as the Shockley-Queisser (SQ) limit [25].

The efficiency of a solar converter, in principle, can be brought to the thermodynamic limit (Carnot efficiency) by means of reflectors and concentrators. However, a single solar cell can approach a much lower limit that depends on its energy gap, geometrical factors linked to radiation and material properties such as the absorption coefficient. The most significant parameter that affects the SQ limit is the fraction of radiative recombination between holes and electrons; this quantity impacts on minority carrier lifetime. The calculation implies an hypothesis known as detailed balance [25]. According to this assumption, the photons absorbed by the cell must be compensated by the emission of less energetic (thermal) photons and it forces electron concentration to be constant in the steady state [19]. If the radiative recombination is only a fraction f_r among all possible recombination events, then the efficiency that could be reached will be lower with respect to the maximum efficiency possible. It is not possible to calculate experimentally this quantity f_r for each material.

The efficiency η is calculated as a function of four different variables. First of all, the calculation involves the ratio x_c of the temperatures of the cell T_c and the Sun T_s, that is:

$$x_\mathrm{c} = \frac{T_\mathrm{c}}{T_\mathrm{s}} \tag{1.16}$$

and the ratio x_g between the energy gap E_g and the energy associated with the temperature of the Sun:

$$x_\mathrm{g} = \frac{E_\mathrm{g}}{k_\mathrm{B} T_\mathrm{s}} \tag{1.17}$$

Efficiency also depends on a factor f in which all the geometric properties of radiation are summarized and on the probability t_s that an incident photon with energy greater than E_g is able to create an electron-hole pair (that the detailed balance forces to be unity). Following this theoretical calculations, efficiency can be written as:

$$\eta(x_\mathrm{g}, x_\mathrm{c}, t_\mathrm{s}, f) = t_\mathrm{s} u(x_\mathrm{g}) v(f, x_\mathrm{c}, x_\mathrm{g}) m(v x_\mathrm{g}/x_\mathrm{c}) \tag{1.18}$$

where $u(x_\mathrm{g})$ is the ultimate efficiency (derived with ideal photoelectric processes with a single cutoff frequency in a device maintained at 0 K and

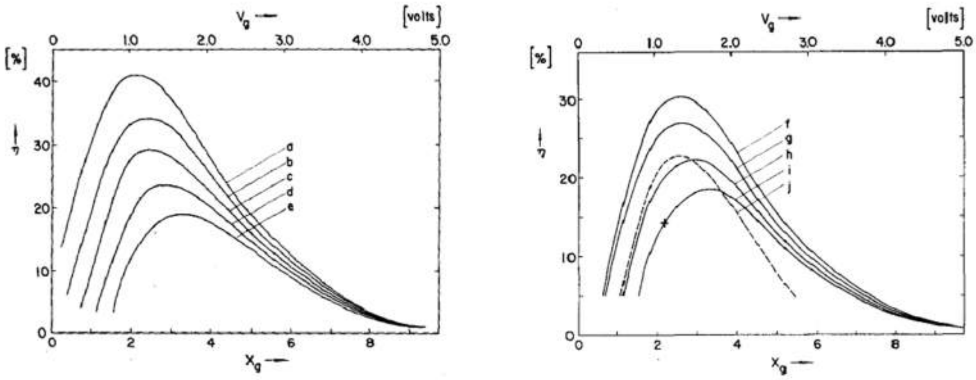

(a) (b)

Figure 1.11: a) Efficiency as a function of energy gap for different values of f: curve **a** $f = 1$; **b** $f = 10^{-3}$; **c** $f = 10^{-6}$; **d** $f = 10^{-9}$; **e** $f = 10^{-12}$. b) Efficiency for a solar cell as a function of the energy gap: curve **f** is the detailed balance limit of efficiency, with $t_\mathrm{s} = 1$; **j** is the semiempirical limit calculated by Prince; **g**, **h** and **i** correspond to 90% of radiation absorbed with different values of f, $0.68 \cdot 10^{-5}$, $0.68 \cdot 10^{-8}$ and $0.68 \cdot 10^{-11}$, respectively [25].

surrounded by a 6000 K black-body radiation), $v(f, x_\mathrm{c}, x_\mathrm{g})$ is the ratio of the open circuit voltage with respect to the energy gap of the cell and $m(vx_\mathrm{g}/x_\mathrm{c})$ is the impedance matching factor, that is a function of the ratio between the open circuit voltage and the thermal voltage of the cell.

Figures 1.11(a) and 1.11(b) show the efficiency behavior with the variation of the energy gap and the geometrical factor f, respectively. There is a decrease of efficiency with the decrease of the parameter f and a peak of the curve at intermediate energy band gaps. Figure 1.11(b) points out the difference between the theoretical curves found by Shockley and Queisser with the semiempirical results achieved by Prince and Loferski [25].

It can be demonstrated that a maximum efficiency η of 33% corresponds to an E_g of 1.4 eV, for the standard AM1.5 solar spectrum. The materials which almost match the best value of energy gap are the III-V compound semiconductors gallium arsenide (GaAs) and indium phosphide (InP) with E_g of 1.42 eV and 1.35 eV respectively. Even though silicon has a smaller indirect band gap (1.12 eV), its low cost, abundance and non-toxicity properties make it the most used material in PV applications [19].

According to the SQ limit theory, the maximum energy conversion efficiency turns out to be of 31%, for a single-junction cell with an energy band gap of crystalline silicon [25]. However, single-junction wafer-based c-Si cells have been independently verified to have experimental record energy conversion efficiencies of 25.0% for monocrystalline silicon cells and 20.3% for multicrystalline cells under standard test conditions (i.e. irradiance of 10^3 W/m^2, AM1.5, 25 ℃) [5, 26].

1.4 Solar cells generations

In 2003 most solar cells sold were based on the so-called *first generation* technology. Because of the high volumes of the materials used, i.e. silicon wafers, its economics was dominated by the costs of these materials (which represented in this first development period over the 70% of total manufacturing costs), with little potential in cost reduction. These cells are mainly used to develop modules installed on the rooftops (Figure 1.12), reaching an efficiency of about 15-20% and having high stability.

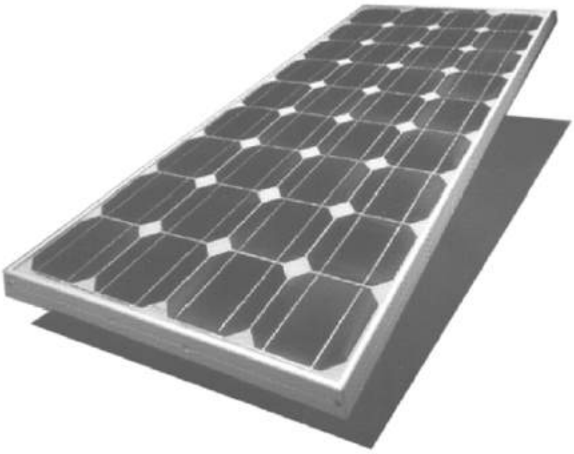

Figure 1.12: Example of first generation technology [27].

From the early 1980s, PV industry was going to switch towards a *second generation* of thin-film solar cell technology (i.e. amorphous silicon, CIGS and CdTe). With a lower material consumption, the first aim of this PV technology was to lower material costs, keeping the efficiency in an acceptable range (10-15%). One approach to a further progress is a substantial increase of conversion efficiency. In this framework, the goal of a *third generation* technology is to improve of 2-3 times the efficiency, keeping low-cost production. This will make PV one of the cheapest options for future energy production. The plot in Figure 1.13 shows that the energy conversion efficiency ranges together with production costs per unit area for the three generations mentioned above [27].

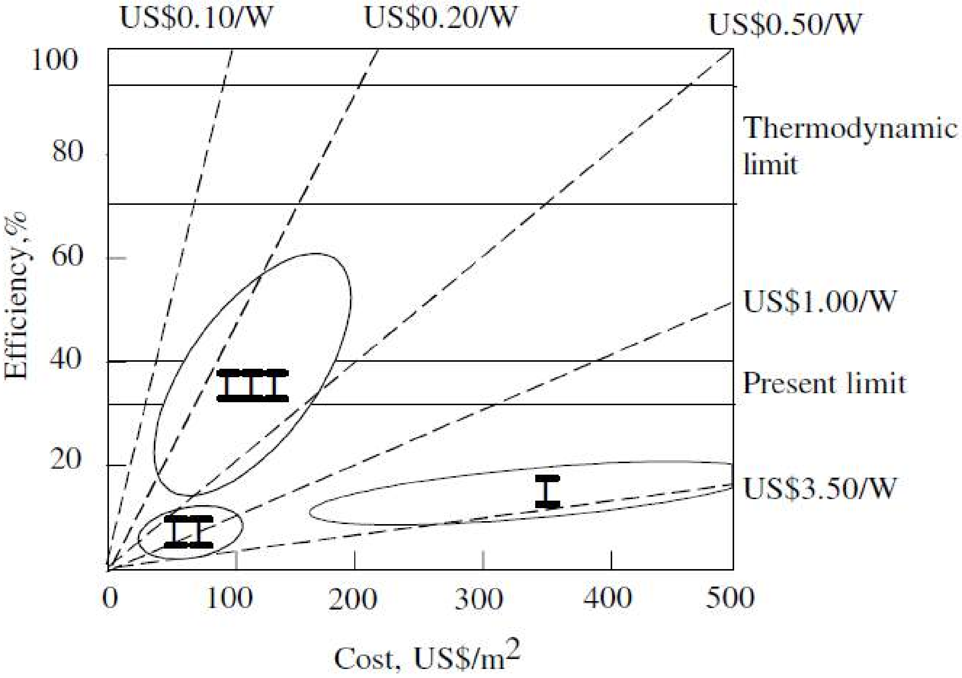

Figure 1.13: Efficiency as a function of areal cost for the three generations of solar cell technology (wafers, thin films and advanced thin films) in USD_{2003} [27].

If efficiency can be improved substantially with third generation technology, even with a moderate increase in areal processing costs, overall electricity production costs will be lower anyway [27].

1.5 Towards SHJ solar cells

Crystalline silicon PV cells remain the most popular solar cells on the market, providing the highest efficiencies in the industrial production. Figure 1.14 shows the structure of a typical commercial monocrystalline solar cell [28]. Standard cells use two different boron-doped p-type silicon substrates: monocrystalline and polycrystalline. A textured coverage on the front surface of the cell is made in order to reduce reflection loss of incident light. A further reduction is achieved with an overlayed anti-reflection coating of silicon nitride (SiN_x) or titanium oxide (TiO_x). In these cells, p-n junctions are constituted by highly phosphorous-doped n^+ (electron-producing) regions on the front surface of boron-doped p-type (electron-accepting) substrates. Back-surface field p^+ regions are positioned on the back surface of the silicon substrate to avoid recombination of minority carriers. Mobile electrons, which are generated in the silicon bulk and diffusion layers, are then collected by silver contacts on the front and on the back of the silicon surfaces [28].

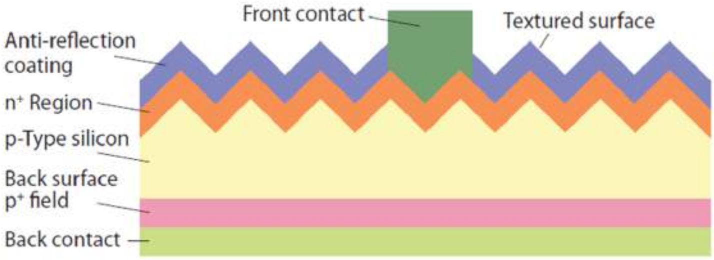

Figure 1.14: Schematic cross-section of a commercial monocrystalline silicon solar cell [28].

Several implementations of wafer-based crystalline silicon (c-Si) PV cells have been developed, in order to reduce costs and increase efficiency. As an example, heterojunction solar cells were introduced to prevent surface recombination due to further reduction of the layers thickness, thanks to the introduction of a passivating layer [5]. Reducing the thickness of the cell, in fact, could lead to a decreased output power, as a consequence of two factors. First of all, there is a reduction of the light absorption, which lowers J_{sc}; secondly, surface recombination is increased, driving to lower values of V_{oc} [29]. From this perspective, the presence of a passivation layer is essential for efficiency increase.

In silicon heterojunction (SHJ) solar cells, in fact, the recombination is reduced since metal contacts are electrically separated from the active material by means of a wider band gap layer; this strategy aimed to increase open circuit voltages, reaching higher efficiencies and lower costs [6]. These buffer layers with a higher band gap have the role of a semi-permeable membrane for carrier extraction [6]. For SHJ devices, hydrogenated amorphous silicon (a-Si:H) thin films are appealing materials for this use: their band gap is slightly wider, with respect to c-Si, and they can be doped relatively easily, enabling the production of both n- and p-type heterojunctions [6]. Hydrogenation of Si dangling bonds is essential to obtain passivation; this important step deeply reduces surface defects. Si dangling bond defect has an amphoteric behavior: according to the position of the Fermi level, it can be a neutral, positively charged or negatively charged state, accomodating 1, 0 or 2 electrons, respectively [6].

Heterojunction technology reaches efficiencies above 20% at the industrial production scale [6]. Indeed, the record efficiency of 25.6% was reached by a SHJ for a cell of practical size (over 100 cm^2) in 2014 as reported in the global efficiency chart made by the National Center for Photovoltaics (NREL) in Figure 1.18 [8, 30]. In the HIT^{TM} structure, a buffer layer of *a*-Si:H is added between the doped emitter and the Si wafer, in order to reduce interface state density [6]. This addition gives a great benefit to the open circuit voltage V_{oc}. A rear buffer layer has also been introduced, promoting a further increase of efficiency beyond 18%, in a final structure illustrated in Figure 1.15 together with its band diagram [6]. In this structure, transparent conductive oxide (TCO) with a low sheet resistance, is deposited as anti-reflecting coating on top and bottom of the silicon layers.

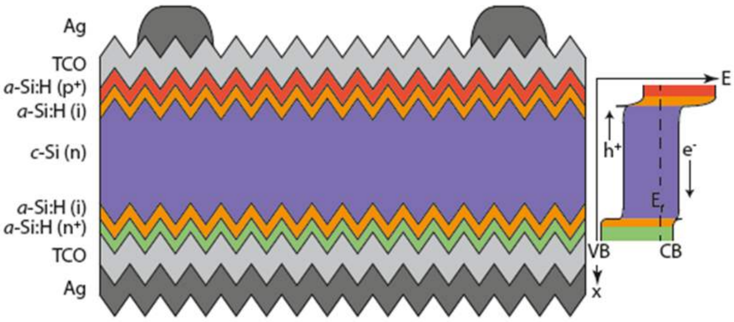

Figure 1.15: Sketch of a HIT^{TM} solar cell as first developed by Sanyo. On the right its band diagram. The wafer is n-type c-Si [6].

Figure 1.16(a) shows the minority carrier lifetime for different layouts. Passivation through doped layers n/c-Si/p (red curve) turns out to be less effective with respect to i/c-Si/i structure (green curve). This severe passivation loss is almost certainly due to doping-related defect generation in the amorphous host matrix. [6]. In order to build a junction for carrier extraction, a ni/c-Si/ip structure should be formed. Passivation values slightly decrease compared with the i/c-Si/i case (blue curve in Figure 1.16(a)) [6].

Another advantage of SHJ solar cells is a lower temperature coefficient, that represents how quickly the efficiency of a solar cell decreases while the temperature of the system increases. The efficiency of conventional c-Si solar cells declines with elevating ambient temperature at a rate of -0.45%/°C, while the heterojunction cells show a lower rate of -0.23%/°C, which makes them comparable to amorphous silicon solar cells (Figure 1.16(b)) [29].

In addition to hydrogenation, annealing can be employed to enhance electronic passivation properties of interfaces between the wafer and the amor-

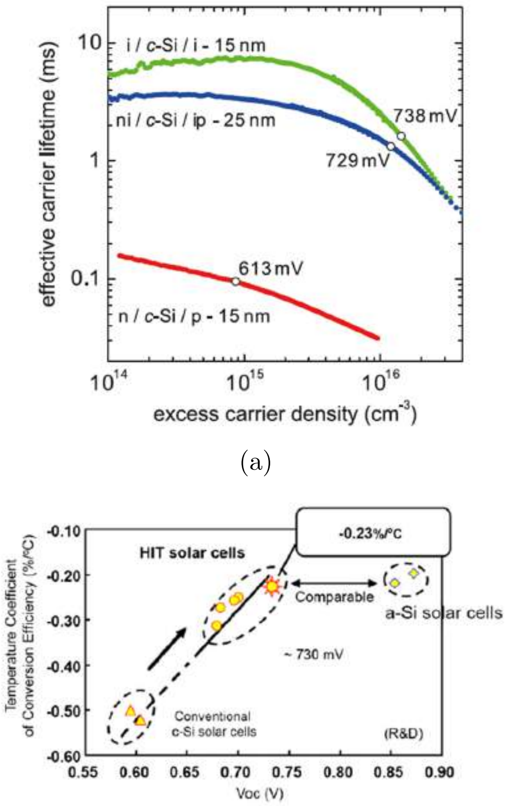

(a)

(b)

Figure 1.16: a) Minority carrier lifetime for *a*-Si:H passivated layer for three different structures. The voltages correspond to the implied V_{oc} under 1 sun illumination [6]. b) Temperature coefficient of the conversion efficiency of a HIT^{TM} solar cell [29].

phous layer. Figure 1.17 shows how the time of isothermal annealing t_{ann} can affect the effective carrier lifetime, τ_{eff}. The curve can be fitted with satisfying accuracy with an exponential law with the form:

$$\tau_{eff}(t_{ann}) = {\tau_{eff}}^{SS}\left[1 - exp\left[-\left(\frac{t_{ann}}{\tau}\right)^{\beta}\right]\right] \tag{1.19}$$

where β is the dispersion parameter ($0 < \beta < 1$), τ is the effective time constant and ${\tau_{eff}}^{SS}$ is the steady-state value of τ_{eff}. This means that diffusion of hydrogen atoms from the higher atomic layers to the surface between *a*-Si:H and c-Si is present [6].

A variety of surface-passivation layers were studied over the years for this

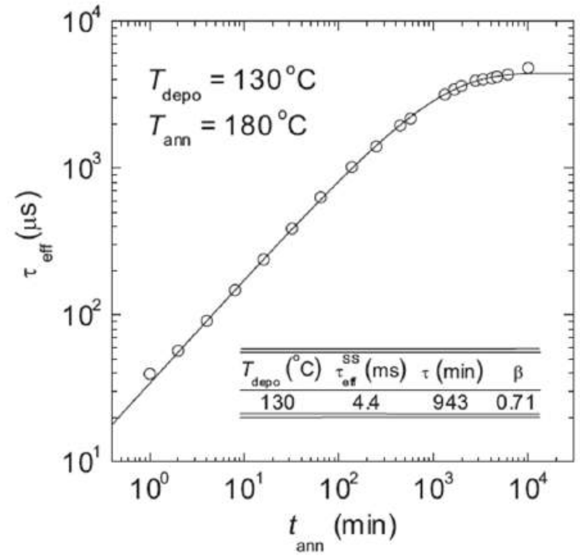

Figure 1.17: Measured values (empty circles) for τ_{eff} as a function of t_{ann}, with annealing at 180 °C. The solid line represents the curve that fits the data [6].

purpose. Starting from silicon dioxide SiO_2, other PV-suitable dielectrics, like *a*-SiN_x:H, SiO_2-*a*-SiN_x:H stacks and aluminum-oxide (Al_2O_3) were used [6]. Despite the good passivation qualities of *a*-Si:H, carriers with short lifetime are generated in this material and a large fraction of them recombine. Moreover, this material suffers for light degradation caused by Staebler-Wronski effect, leading to an unstable behavior.

For these reasons, new materials have been investigated and silicon oxynitride (SiO_xN_y) has been studied as a promising substitute of *a*-Si:H in both intrinsic and doped layer of the hetero-emitter (red and orange layers in Figure 1.15) [9].

SiO_xN_y has recently been investigated due to its application in different and innovative fields, together with its low-cost fabrication technology. Indeed, the tunability of both optical band gap and refractive index makes it a very good candidate in optoelectronic devices, ultra-thin films transistors and LED [31, 32, 33, 34, 35]. Thanks to its reduced parasitic light absorption and higher band gap, SiO_xN_y can boost the solar cell efficiency, in the role of the hetero-emitter [31]. In fact, non stoichiometric SiO_xN_y films in both amorphous and nano-crystalline phase already exhibited high band gap (2.5 *e*V) and high conductivity (44 S/cm) [31]. Moreover, nanocrystalline-(nc) SiO_xN_y could obtain excellent transport properties, in particular a lower contact resistivity with the TCO with respect to an amorphous layer, while amorphous (*a*-) $\mathrm{SiO_xN_y}$ shows elevated passivation properties [36]. The substitution of both these layers in the hetero-emitter stack of the solar cell, will lead to a further increase of the efficiency of the device, which already reached very high values (25.6%).

However, the structure of these films is complex, since different phases and compositions coexist. Few studies have recently been done on conductivity and optical band gap of these materials and their correlation to the oxygen content [31, 10, 11]. Moreover, a study on the structure and the formation of the crystalline phase still lacks and the effect of the crystalline fraction and the oxygen content on $\mathrm{SiO_xN_y}$ optical and electrical properties is still unclear. In this framework, a study of nano-scale electrical and morphological properties of these innovative materials is mandatory. This is the purpose of this thesis.

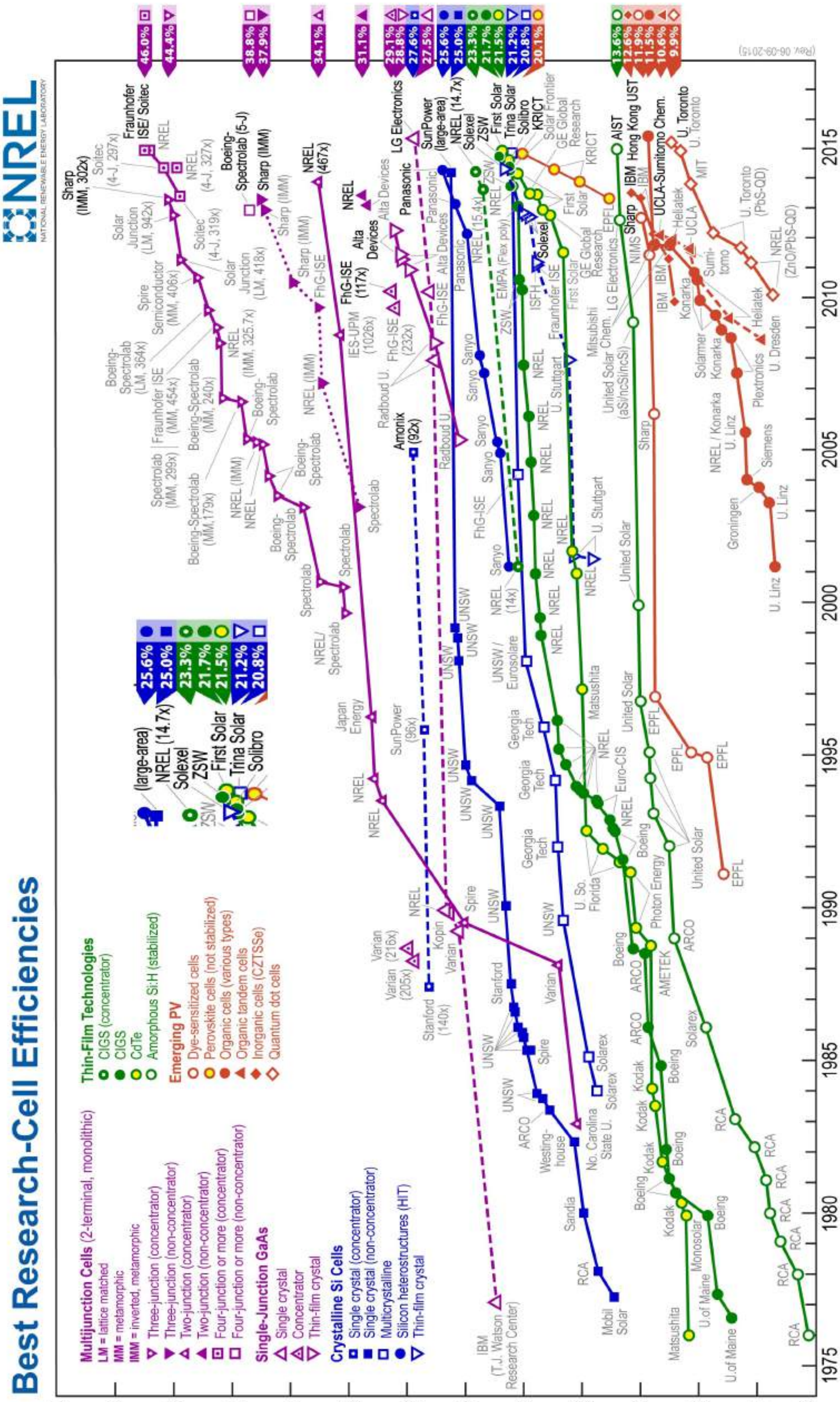

Figure 1.18: Record cell efficiency chart updated to 2015 [30].

Chapter 2

Materials and Methods

2.1 Materials

In this thesis, two series of different materials have been investigated by Atomic Force Microscopy techniques, described in detail in Section 2.2: silicon oxy-nitride ($\mathrm{SiO_xN_y}$) thin layers in nano-crystalline p-type doped (nc) and intrinsic amorphous (a) forms. These can be suitable materials in SHJ solar cells application, since they have suitable electrical and optical properties to substitute doped and intrinsic layers, respectively, in the hetero-emitter stack on top of c-Si layer in the device in Figure 1.15. Both nc- and a-$\mathrm{SiO_xN_y}$ layers are grown by Plasma Enhanced Chemical Vapor Deposition (PECVD) using a commercial system (PlasmaLab 100 from Oxford Instrument) in a parallel plate configuration operating with radiofrequency (RF) of 13.56 MHz [31, 37]. The materials are grown at the Department of Physics of the University of Konstanz, Photovoltaic Division.

This technique is a particular branch of a wider group of materials-processing technology called Chemical Vapor Deposition (CVD). CVD has been used to deposit a wide range of materials in many different application areas. Its major employment involves applying solid thin-film coatings to surfaces, but CVD is also used to grow high-purity bulk materials and powders, as well as in the production of composite materials via infiltration techniques [38]. The basic CVD procedure involves the flow of a precursor gas into a chamber in which one or more heated objects to be coated are present. Chemical reactions between the gases and the substrates occur on and near the hot surfaces and the deposition of a thin film is generated. This process is accompanied by the production of unwanted chemical by-products that are delivered out of the chamber together with unreacted precursor gases. CVD is characterized by several advantages. Its deposition rate is fast and can produce an homogeneous layer of a wide variety of materials, reaching a very high purity [39, 38]. PECVD or plasma-assisted CVD involves a variety of reactor designs, in which a plasma is used to dissociate the CVD precursor gas creating smaller, more reactive, molecules. Plasma is generally created by an RF or DC discharge between two electrodes, the space between which is filled with the reacting gases [38]. The presence of this catalyst allows higher rates of thin film deposition, that can occur at lower temperatures [38]. A simplified scheme of a PECVD instrument is given in Figure 2.1.

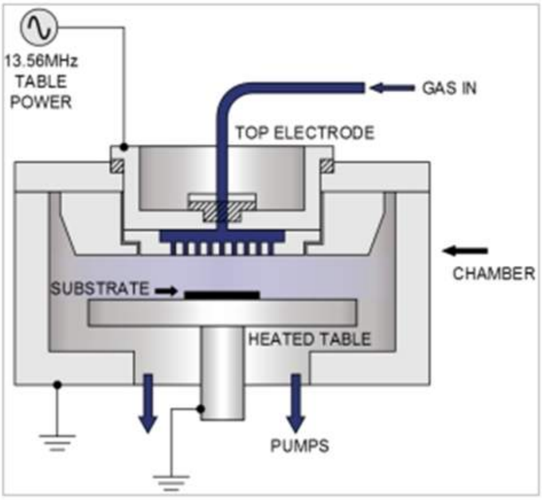

Figure 2.1: Schematic view of a PECVD device structure [40].

For the deposition of both SiO_xN_y series of samples, different precursor gases have been employed. In order to evaluate their influence on morphological and electrical properties of the materials, different deposition parameters have been varied in the two series.

Previous studies on hydrogenated a-SiO_xN_y thin films have been carried out to investigate their properties as passivating layers in SHJ structures [9]. These new materials can be a valid substitute for intrinsic amorphous silicon (a-Si:H), which already provided an excellent surface passivation quality, reaching a high efficiency potential above 20%. The greater drawback of a-Si:H is the heavy parasitic absorption of light which is the cause of low values of short circuit current. This absorption can be reduced with the introduction of a wider band gap material. Indeed, the optical band gap of a-SiO_xN_y layers can be widened up to 2.2 eV, thanks to the incorporation of oxygen and nitrogen into the amorphous network [9]. Moreover, passivation quality and dark conductivity, which are correlated to oxygen and nitrogen contents, can be improved. Combining intrinsic (with high effective minority carrier lifetime of 2.5 ms) and doped *a*-SiO_xN_y thin films (with conductivities up to $4.5\cdot 10^{-3}$ S/cm for the n-type and $3.9\cdot 10^{-4}$ S/cm for the p-type doping) to hetero-emitter stacks on c-Si base lead to a high open circuit voltage of 733 mV [9]. A further efficiency increase can be expected substituting the amorphous emitter with a nano-crystalline one, for a higher conductivity and a lower contact resistance with the TCO layer [31, 13].

2.1.1 nc-SiO_xN_y

nc-SiO_xN_y thin layers were deposited by PECVD at 300 ℃ on Float Zone silicon (FZ-Si) and glass substrates, using silane SiH_4, hydrogen H_2 and nitrous oxide N_2O as precursor gases, while diborane B_2H_6 is added to achieve a p-type doping [31, 32]. Diborane is diluted in hydrogen (0.5%). The flow of nitrous oxide and the ratio of diborane are both referred to their dilution in silane. Then, N_2O and B_2H_6 ratios must be defined, respectively, as:

$$R_{N_2O} = \frac{[N_2O]}{[N_2O] + [SiH_4]} \tag{2.1}$$

$$R_{B_2H_6} = \frac{[B_2H_6]}{[B_2H_6] + [SiH_4]} \tag{2.2}$$

where the square brackets represent the gas concentrations. All the samples under investigation in this work were deposited with $R_{B_2H_6} = 2.34\%$ and were then annealed at 800 ℃ in a nitrogen atmosphere to promote nanocrystal formation. An equivalent effect could have been achieved with an enhancement of the hydrogen dilution during the deposition phase, but an annealing step turned out to be necessary due to the technical limitation of the system used in the H_2 to SiH_4 ratio. Table 2.1 shows the deposition parameters of all the samples, where the thickness was measured by ellipsometry and the corresponding growth rate was evaluated.

Table 2.1: List of deposition parameters of nc-SiO_xN_y thin films.

Sample name	Annealing time (h)	R_{N_2O} (%)	$R_{B_2H_6}$ (%)	Rate (Å/s)	Thickness (nm)
C	0, 3, 6	9.09	2.34	2.32	209
E	3	47.4	2.34	3.14	283

A Scanning Electron Microscope (SEM) image of the cross section of similar nc-SiO_xN_y sample (with $R_{N_2O} = 16.7\%$ annealed for 3h, 224 nm thick) in

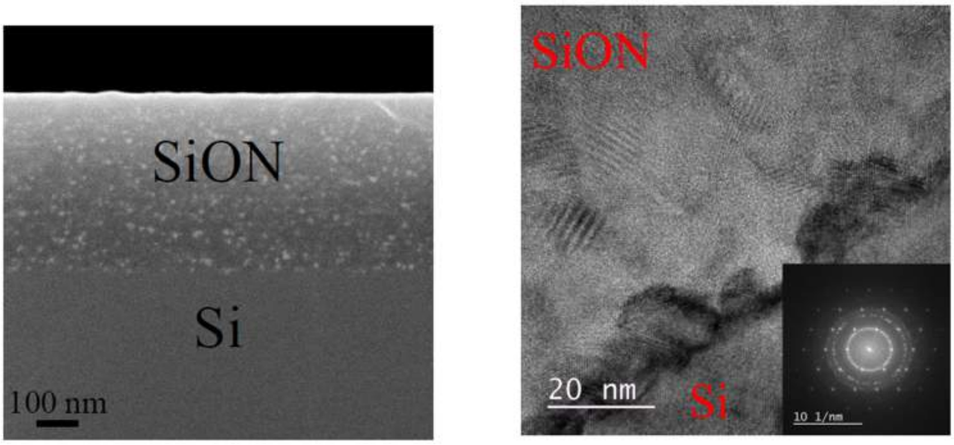

(a) (b)

Figure 2.2: a) A cross section SEM image of a nc-SiO_xN_y sample grown on silicon. b) HR-TEM picture of a nc-SiO_xN_y sample with its relative diffraction pattern on the bottom right [41].

Figure 2.2(a) points out different areas due to the presence of nano-crystals (NCs) [31, 41]. In High-Resolution Transmission Electron Microscope (HR-TEM) image (Figure 2.2(b)), these crystals clearly form randomly without a preferred crystalline orientation in a different sample ($R_{N_2O} = 28.6\%$ annealed for 6h). The inset of Figure 2.2(b), in which the diffraction pattern of the layer is depicted, confirms the absence of a preferred NCs orientation and reveals the presence of an amorphous network (rings and diffused halo in the pattern) [41].

By Raman spectroscopy measurements, the crystalline fraction χ of the samples was evaluated on layers deposited on a glass substrate. The following expression was employed to evaluate this quantity:

$$\chi = \frac{I_\mathrm{C}}{I_\mathrm{C} + I_\mathrm{A}} \tag{2.3}$$

where I_A represents the integrated area of the peak at 480 cm^{-1} associated to the amorphous component and I_C is the integrated area of the peak at 520 cm^{-1} of the crystalline phase, as is depicted in Figure 2.3 [41]. The introduction of the parameter χ is useful to compare the crystallinity of different samples [31].

A thorough analysis of a complete series of nc-SiO_xN_y thin layers, to which samples investigated in this work belong, leads to the result that crystalline fraction rises with the addition of the thermal treatment, with respect

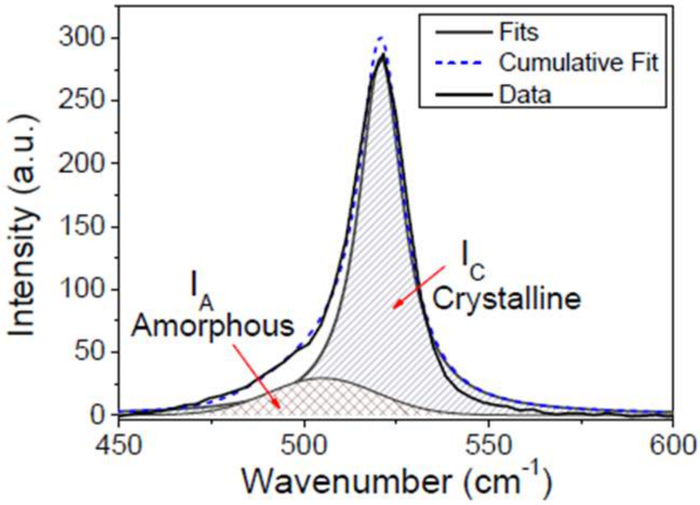

Figure 2.3: Raman spectrum of a nc-SiO_xN_y sample with R_{N_2O} = 9.09% annealed for 3h. Both individual fits of amorphous and crystalline fits and the cumulative fit are highlighted [41].

to the as-deposited samples, but saturates after 3h of annealing in the oven, as plot in Figure 2.4(a) depicts [31]. On the other hand, crystallinity diminishes with the increase of N_2O dilution, ranging from 44% to 83%, as shown in Figure 2.4(b). The first result demonstrates that the annealing process promotes NCs formation, while the second asserts that the increase of oxygen content in the sample limits the crystalline fraction [41, 9]. Moreover, it follows that lower crystalline fractions are reached in the as-deposited samples with respect to annealed ones, whose χ are always above 85%. A higher N_2O content induces an increase of disorder due to an incorporation of nitrogen and oxygen within the amorphous phase, causing a drop in the crystallinity fraction [9]. The absolute concentration of oxygen and nitrogen of hydrogenated a-SiO_xN_y (:H) was analyzed by means of secondary-ion mass spectroscopy (SIMS) [9]. SIMS measurements demonstrated that higher N_2O dilutions lead to a linear increase of oxygen content, while nitrogen content remains almost constant, as Figure 2.4(c) illustrates [9].

Previous studies of the lateral conductivity in the dark σ_{dark} determined by IV characteristic measurements of the layers (deposited on glass after the deposition of titanium/palladium/silver contacts on top of them by electron beam evaporation) have demonstrated that this parameter follows the same decrease of χ with rising R_{N_2O} (Figure 2.5(a)) [31]. A very high dark conductivity of 44 S/cm is reached for the nc-SiO_xN_y sample with R_{N_2O} = 9.09%

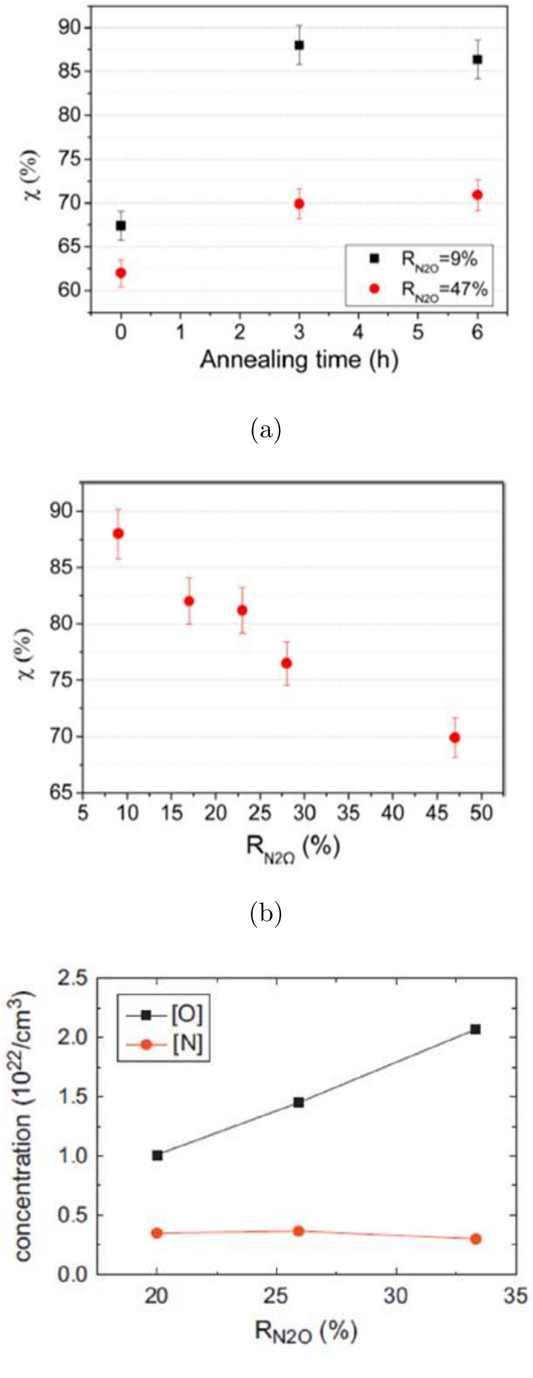

(a)

(b)

(c)

Figure 2.4: a) Crystalline fraction χ depending on the annealing time for two nc-SiO_xN_y samples with different N_2O dilution. b) Crystalline fraction χ dependence on N_2O dilution in samples 3h annealed [31]. c) Oxygen and nitrogen concentration of a-SiO_xN_y:H films as a function of N_2O concentration [9].

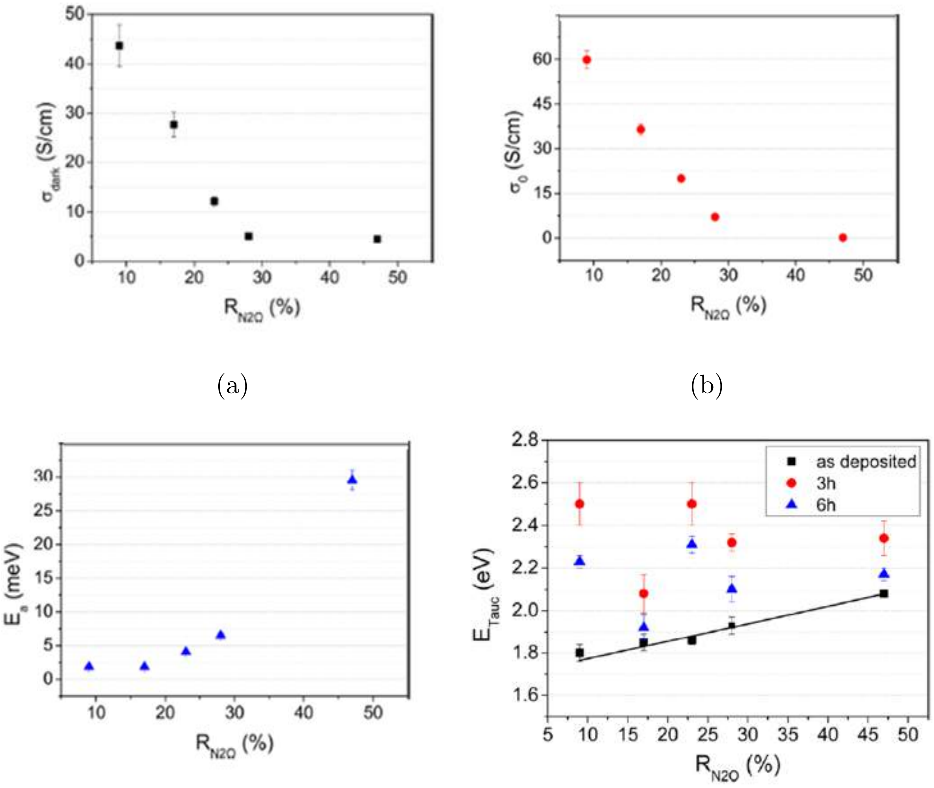

(a) (b)

(c) (d)

Figure 2.5: a) Room temperature dark conductivity σ_{dark}, b) pre-exponential factor σ_0 and c) activation energy E_{a} as a function of $\mathrm{R}_{\mathrm{N_2O}}$ in samples 3h annealed. d) E_{Tauc} as a function of the $\mathrm{R}_{\mathrm{N_2O}}$ for different annealing times [31].

annealed for 3h. To gain more information about the conduction mechanism, temperature-dependent IV measurements were performed between 150 and 300 K. For semiconductors, electrical conductivity follows an exponential law, that is:

$$\sigma = \sigma_0 \exp\left[-\frac{E_{\mathrm{a}}}{k_{\mathrm{B}}T}\right] \tag{2.4}$$

where σ_0 is the pre-exponential factor and E_{a} is the activation energy requested for conduction to occur. While σ_0 follows approximately the same trend of the χ, E_{a} increases with higher values of $\mathrm{N_2O}$ dilution (Figures 2.5(b) and 2.5(c)) [31]. This effect is probably due to a higher disorder promoted by the larger oxygen content in the layers [31].

As regards the optical properties, both absorption coefficient α and Tauc gap E_{Tauc} of nc-$\mathrm{SiO_xN_y}$ layers were estimated from transmission and reflection spectra measurements of the layers deposited on glass [31]. The first parameter α was approximated by the law:

$$\alpha\left(h\nu\right)=\frac{1}{d}\ln\left(\frac{1-R\left(h\nu\right)}{T\left(h\nu\right)}\right) \tag{2.5}$$

where $R\left(h\nu\right)$ and $T\left(h\nu\right)$ are the measured transmission and reflection spectra, respectively, while d is the thickness of the layer [42, 31]. The Tauc gap E_{Tauc} is correlated to the absorption spectra and the incident light as in Equation 1.15 for a semiconductor with indirect band gap; this law can be rewritten in the following form [43, 31]:

$$\left(\alpha h\nu\right)^{1/2}\propto\left(E_{\mathrm{Tauc}}-h\nu\right) \tag{2.6}$$

The Tauc gap increases linearly with N_2O dilution in the as-deposited state, possibly due to a higher oxygen incorporation in the film (black squares in Figure 2.5(d)). In annealed samples, no trend of E_{Tauc} with N_2O dilution was observed, but values are generally larger with respect to as-deposited samples (red dots and blue triangles in Figure 2.5(d)). This rise could be correlated to two different effects: quantum confinement effects resulting from NCs formation and the presence of O-rich areas. A decrease of the energy gap from 3 to 6h annealing can be related to a reduced quantum confinement since NCs dimensions become greater [31].

At last, Fourier Transform Infrared (FTIR) spectroscopy gave information on Si-O-Si, Si-H and Si-H_2 bonds within the nc-SiO_xN_y thin layers [41]. In the as-deposited state (black squares in Figure 2.6(a)), the peak position of the Si-O-Si bonding signal shifts linearly with the increase of N_2O dilution towards higher wavenumbers [31]. The linearity of this shift is due to a homogeneous distribution of Si-Si and Si-O-Si bonds within the layers [44, 45]. Moreover, the intensity of the Si-O-Si peak increases for greater values of R_{N_2O} (Figure 2.6(b)), evidence of a higher oxygen incorporation within the layers [31]. The thermal treatment causes a shift of the peak position toward higher wavenumbers in all nc-SiO_xN_y thin films (Figure 2.6(a)) and its non-linearity indicates a phase separation in annealed layers of Si-rich and O-rich areas [31].

After these preliminary and complementary studies, a deeper analysis of morphological and electrical properties at the nano-scale on nc-SiO_xN_y thin layers is mandatory. The choice of the series of samples under investigation in this work, with the parameters described in Table 2.1, was made considering the best and the worst electrical and structural properties of the whole series. Sample C with 3h of annealing demonstrated to have the highest crystalline fraction up to 88% (Figure 2.4(b)), the highest dark conductivity $\sigma_{\mathrm{dark}}=$

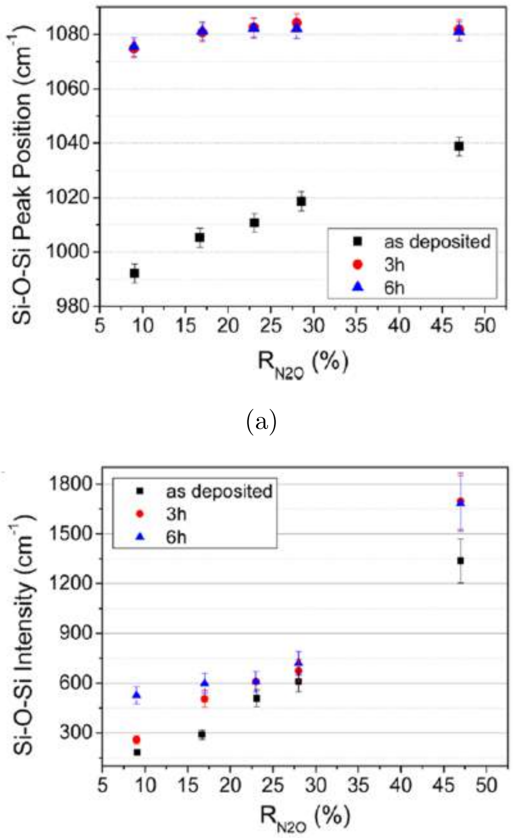

(a)

(b)

Figure 2.6: a) FTIR Si-O-Si peak position and (b) its intensity for different nc-SiO_xN_y samples [31].

$(44 \pm 4)\ S/cm$ (Figure 2.5(a)) and the highest energy gap $E_{\mathrm{Tauc}} = (2.5 \pm 0.1)\ eV$ (Figure 2.5(d)). For this reason Sample C is the best candidate in substituting nc-Si:H in HJ solar cells. In this work the effect of annealing on the nano-scale properties is also investigated.

2.1.2 *a*-$\mathrm{SiO_xN_y}$

Amorphous intrinsic $\mathrm{SiO_xN_y}$ (*a*-$\mathrm{SiO_xN_y}$) thin films have been deposited by PECVD at 175 ℃, using silane ($\mathrm{SiH_4}$), nitrous oxide ($\mathrm{N_2O}$) and hydrogen ($\mathrm{H_2}$) as precursor gases. $\mathrm{N_2O}$ ratio defined in Equation 2.1 for these samples has been kept at 13% with a deposition time of 30 s. In this series, which consist of four samples, all the deposition parameters have been kept constant with the exception of the electrode distance, which varies between 22 and 55 mm [46]. Characteristics of the samples investigated are reported in Table 2.2.

Table 2.2: List of deposition parameters of *a*-$\mathrm{SiO_xN_y}$ thin films.

Sample name	Electrode distance (mm)	Thickness (nm)
1	22	24
2	30	22
3	40	21
4	55	16

Ellipsometry measurements have shown a linear trend of thickness with the deposition time (see Figure 2.7(a)), except for Sample 1, that suffers of fast growing in the first 30 s of deposition. Minority carrier lifetime has been investigated in relation to both the annealing time (at 300 ℃ up to 20 min in ambient air) and the electrode distance, as Figure 2.7(b) illustrates. Lifetime increases during the first 12 min of annealing, while it saturates for higher times [46]. Sample 3 has achieved the best passivation qualities reaching a lifetime of 296 μs. FTIR spectroscopy measurements have revealed the presence of three different peaks in Si-H bonding region, probably due to the presence of different atoms (Si/O) back-bonding to the Si-H band [46]. The position of these peaks increases with higher values of electrode distance, as the plot in Figure 2.7(c) illustrates. This trend is probably due to a greater incorporation of O and N atoms, which determines a higher electro-negative surrounding region of the Si-H bond [46].

In this perspective, an investigation on morphological and electrical properties at the nano-scale can be interesting, to see in which way these char-

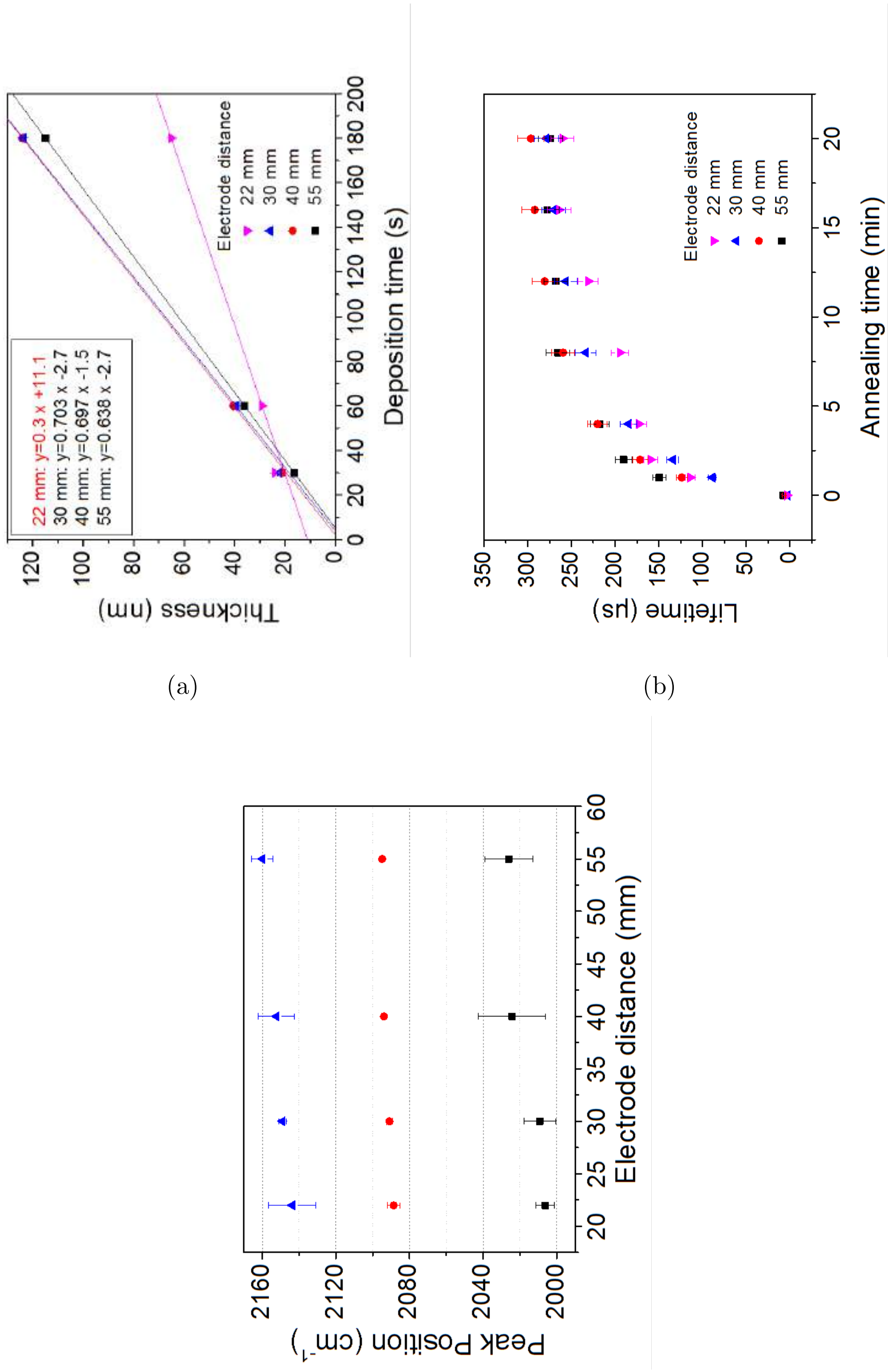

(a)

(b)

(c)

Figure 2.7: a) Thickness dependence on deposition time for the *a*-SiO$_x$N$_y$ layers under investigation. (b) Minority carrier lifetime as a function of annealing time for the *a*-SiO$_x$N$_y$ layers. c) Position of the FTIR peaks in the Si-H bond region as a function of the electrode distance [46].

acteristics can or cannot be affected by variant electrode distance in the deposition process.

2.2 Experimental Methods

Both series of nc- and a-SiO$_x$N$_y$ thin films have been investigated by Atomic Force Microscopy and conductive-Atomic Force Microscopy techniques, to achieve both morphological and electrical information at the nanoscale.

2.2.1 Scanning Probe Microscopy

With the advent of nanostructured materials, new experimental techniques were needed. Before the idea of Scanning Probe Microscope (SPM) techniques came out, morphological analysis of surfaces were realized by means of electronic microscopes. In these techniques an electron beam, extracted from a conductor by photoelectric effect, passes through the sample and the prevalent radiation which is collected is that of secondary electrons [47]. This portion of radiation is constituted by low energy electrons ($<$ 50 eV), therefore, only electrons of the first layers of the sample have enough energy to reach the detectors. Unfortunately, these tools, Scanning and Transmission Electron Microscopes (SEM and TEM, respectively), require Ultra High Vacuum (UHV) as well as high voltages to accelerate the electronic beam, properties that make them expensive techniques. Moreover, the energetic beam inevitably corrupts the sample and the information collected belongs to a subtle surface layer, not isolating the first atomic layer of the sample [47]. In this framework, the development of devices capable of analyzing sample surfaces became necessary and SPMs were introduced to reach this goal.

The first SPM was realized in 1981 by Gerd Binnig (Frankfurt, July 20, 1947) and Heinrich Roher (Buchs, June 6, 1933 - Wollerau, May 16, 2013) in 1981. This system maintains a small gap of few angstroms (Å) between tip and sample, controlled by the tunnel current flowing between them [48]. With one electrode shaped into a tip, current flows only, in the best case, from a specific orbital of the apex atom; therefore, a lateral resolution of atomic dimensions can be achieved.

The brilliant attitude of the two researchers was demonstrated in giving solutions to the main instrumental problems: for example, the employment of soft suspensions in the microscope within a vacuum chamber, in order to protect the probe from vibrations and acoustic noise; or the introduction of

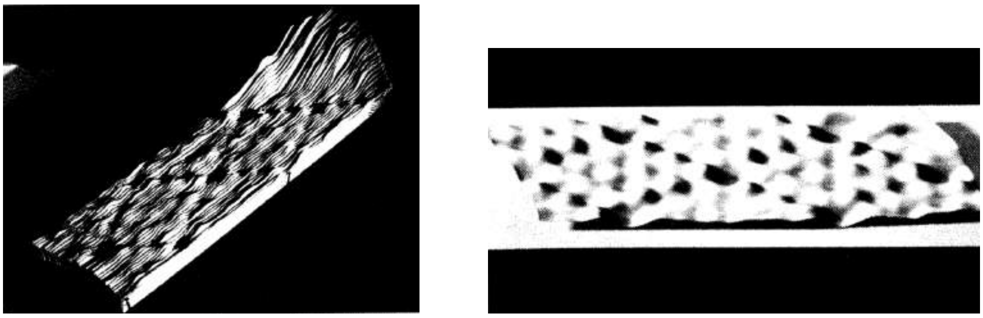
(a) (b)

Figure 2.8: a) Picture from the original recorded traces and b) processed image of 7 × 7 reconstruction of Si(111) [48].

a piezoelectric material, which links electronics and mechanics, to move the tip with an extreme accuracy [48]. After several attempts prolonged for 27 months, the night of March 16, in 1981 they obtained their first exponential dependence of the tunnel current from the tip-sample separation, with a tunnel-barrier height of more than 4 eV, a value compatible with vacuum tunneling.

By means of this unique technique, which is called Scanning Tunneling Microscopy (STM), in the Autumn of 1982 Binnig and coworkers were able to observe the 7×7 reconstruction of Si(111) surface (Figures 2.8(a) and 2.8(b)). They were finally able to see what they still call the *color of the atoms* [48]. After years of skepticism, STM was finally accepted from the research world in 1985. The year after, Binnig and Roher were awarded of the Nobel Prize in Physics "for their design of the scanning tunneling microscope" [49].

Despite STM subangstrom resolution in all three dimensions, its characterization was restricted to conductive and semiconductive materials only, with vacuum as an essential element [47]. As a consequence, in 1985 G. Binnig and C. F. Quate introduced a new type of probe, this time based on atomic interactions between the tip and the sample, which they called Atomic Force Microscope (AFM) [50]. AFM can work in air or in liquid ambient and provides three-dimensional surface topography at nanometer lateral and subangstrom vertical resolution on insulators and conductors [47].

In previous time, SPM consisted of techniques which employ a sharp tip for scanning a sample surface, creating a high resolution image monitoring the interaction. In addition to AFM, several SPM techniques have been developed for industrial and scientific applications, which exploit different types of sample-tip interactions to provide information on differences in friction, hardness, electric and magnetic fields, carrier concentration, temperature distribution and conductivity [47].

With respect to a SEM, AFM can also acquire information and 3D topography from small sections of surfaces (reaching areas with sides of fractions of micrometers). Considering their differences, electronic microscopes and AFM can be complementary in the study of surface properties of thin films. The peculiar characteristics of AFM make it a unique instrument for the investigation on thin films, determining changes in morphology and composition with variations of deposition parameters, such as precursor gases percentages, time of annealing, temperature, pressure, etc.

2.2.2 Atomic Force Microscopy

The instruments used to acquire images of all samples in this work are two AFMs: a NT-MDT Solver P47H Pro and a Park NX10. In general, an AFM consists of several elements that can work in different operating modes, depending on the aim of the measurement.

The working principle behind an AFM is the measurement of sample-tip interaction, by means of an elastic lever with a pointed tip fixed in its free part. The force applied on the tip produces a measurable bending of the cantilever, that can provide information of the interaction itself. The tip, with the shape of a needle, has a working part of more or less ten nanometers (nm), whereas the usual tip-surface distance is about 0.1 - 10 nm. [51]. The interactive forces between the tip and the sample can be modeled as van der Waals forces between two atoms at a distance r, described by Lennard-Jones (LJ) potential:

$$U_{LJ}(r) = U_0 \left[-2 \left(\frac{r_0}{r} \right)^6 + \left(\frac{r_0}{r} \right)^{12} \right] \tag{2.7}$$

where r_0 represents the equilibrium distance between the atoms and corresponds to a minimum in the potential. The first term describes the attractive force of a dipole-dipole polarization, while the second is related to the short range repulsion (Pauli principle) [51]. The curve described by Equation 2.7 is depicted in Figure 2.9.

In this framework, the tip is attracted at large distances and repelled at small distances from the sample.

2.2.3 AFM: Instrumental Apparatus

The principal constituents of an AFM are the same of all Scanning Force Microscopes (SFM): a force sensor, an optical system that measures the cantilever bending, a piezoelectric scanner, an anti-vibration system and an

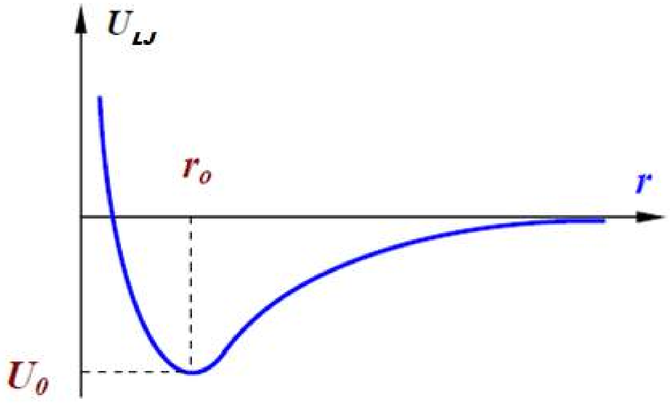

Figure 2.9: Qualitative shape of LJ potential. U_0 represents the minimum of the curve [51].

electronic system for both feedback control and image acquisition [52]. A schematic view of the whole instrument is shown in Figure 2.10.

Surface sensors in AFM are special probes made of a very flexible cantilever with a sharp tip on its free end. The force F between the tip and the sample can be simplified by Hooke's law, that is:

$$F = -k \cdot \Delta z \tag{2.8}$$

where k is the elastic constant of the cantilever and Δz is the tip displacement caused by the cantilever bending [51]. According to the type of instrument and the information aimed to be collected, it is possible to choose from a variety of both cantilevers and tips. Cantilevers differ in several properties like normal (k_N) and lateral (k_L) elastic constants, resonance frequency (ω_res), dimensions (length l, thickness t and width w) and shape, while tips have diverse curvature radii, can be made of a variety of materials and can be coated for electrical measurements [52]. In order to obtain high resolution and reproducible topographies, the probes must have the following properties. First of all, to reduce sensibility to external vibrations and thermal noise, probes have particular geometries aimed to produce elevated ω_res. However, values for resonance frequencies are limited, since they are inversely proportional to the maximum scan area. A compromise is reached and typical values of ω_res are 10 - 100 kHz [51]. Moreover, to obtain atomic resolution, the normal spring constant of the cantilever should be weaker than the equivalent spring between atoms, i.e. 10 N/m [52]. A minimum value of 10^{-2} N/m is

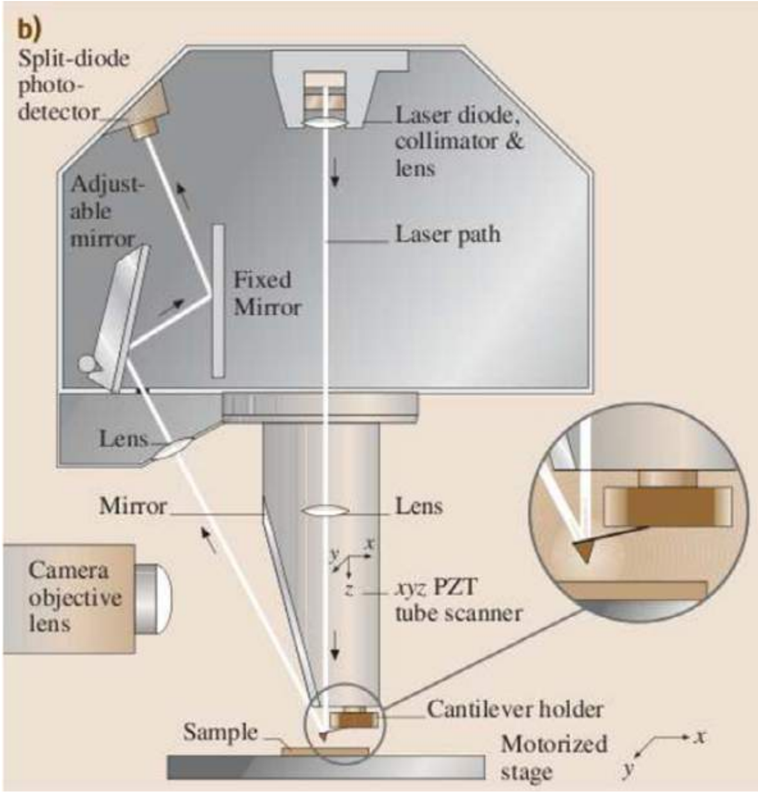

Figure 2.10: Schematic view of a typical configuration of a SFM [52].

recommended, since k_N is correlated to ω_{res} in the function:

$$\omega_{res} = \sqrt{\frac{k_N}{m_{probe}}} \tag{2.9}$$

where m_{probe} is the probe mass. The mass of the cantilever must be reduced, in order to combine requirements of a low spring constant and a high resonant frequency [52]. Another fundamental property for estimating probe efficiency is the *quality factor* Q, defined as:

$$\mathrm{Q} = \frac{\omega_{res} m_{probe}}{\gamma} \tag{2.10}$$

where γ is the damping constant. This quantity determines the sensitivity of the measurement, then a high value of Q is essential (100-1000) especially in non-contact mode. Moreover, an elevated k_N is required to avoid significant errors in the normal forces detection, while a reflective coating (Al, Au) on the top of the cantilever increases reflectance. At last, a centered and very

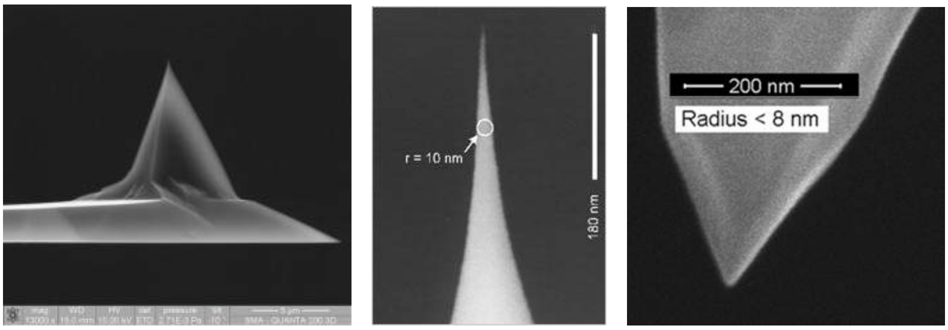

(a) (b) (c)

Figure 2.11: SEM images of a) NSG10 and CSG10/Pt, b) Nanosensors SSS-NCHR and c) RMN-25PT300B tips for AFM [53, 54, 55, 56].

thin tip is necessary in order to distinguish nanometric structures [51]. Cantilevers can be synthesized by photolithography techniques, chemical plasma etching and ionic implantation. The most common materials employed in the production are Si_3N_4, Si and diamond [51]. For electrical and magnetic measurements special coatings are added, which cause an increase in the dimensions of the tip. In this work, different tips are used and their SEM images are shown in Figure 2.11(a), 2.11(b) and 2.11(c) [53, 54, 55, 56]. Semi-contact, contact and conductive analysis have been obtained and all tips characteristics are described in Table 2.3.

Table 2.3: Characteristics and parameters nominal values of the tips employed in the measurement. S-CONTACT stands for SEMI-CONTACT.

Tip	**NSG10**	**CSG10/Pt**	**SSS-NCHR**	**25PT300B**
AFM	NT-MDT	NT-MDT	PARK	PARK
Mode	S-CONTACT	CONTACT	S-CONTACT	CONTACT
l (μm)	100	250	125	300
w (μm)	35	35	30	100
ω_{res} (kHz)	255	20	330	20
k_{N} (N/m)	11.5	0.1	42	18
Radius (nm)	10	35	5	< 20
Coating	-	Pt	-	-

To detect the cantilever bending, an optical system is employed (Figure 2.12(a)). A collimated beam from a diode-laser is focused on the lever and then reflected toward the center of a four-section split photodiode (Figure 2.12(b)) [51]. In this work, both AFMs used in the image acquisition of

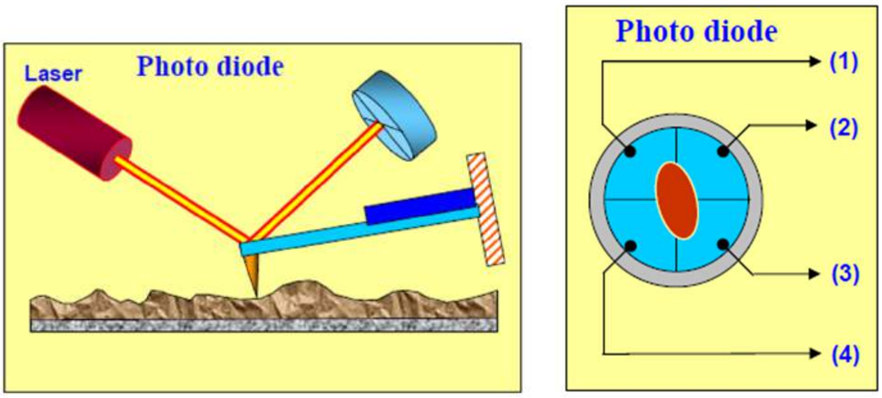

(a) (b)

Figure 2.12: a) Schematic view of the optical system in an AFM. b) Four-section split photodiode [51].

the samples have this kind of bending detection system.

This division in the photodiode allows the detection of two forces: the cantilever bending due to attractive or repulsive forces (DFL) and the cantilever torsion due to lateral components (LF) [51]. The differences between the photocurrents of the four sectors determine these quantities, in fact:

$$\mathrm{DFL} = (\Delta I_1 + \Delta I_2) - (\Delta I_3 + \Delta I_4) \tag{2.11}$$

$$\mathrm{LF} = (\Delta I_1 + \Delta I_4) - (\Delta I_2 + \Delta I_3) \tag{2.12}$$

where ΔI_i is the difference in the photocurrent in presence and absence of interaction in the i-th sector of the photodiode. In the absence of sample-tip interaction, laser is positioned at the photodiode center. When the tip lands on the sample, its bending causes a beam displacement. The photocurrent in each sector of the photodiode, measured in each scanned point of the sample, enables an estimation of the bending intensity and direction [52]. The optical system has a great influence on the sensitivity limitation of the device. It can be affected by saturation effects of the photodiode and diffraction phenomena, while shotnoise signal, thermal noise and quantum-mechanical uncertainty generate errors in the calculation of sample-tip distance variations (orders of $10^{-11} - 10^{-17}$ meters) [52].

DFL value is sent as an input parameter in a feedback loop of the microscope, which keeps it constant by means of a piezoelectric transducer (scanner), which controls the tip-sample distance in order to maintain the bending Δz always equal to the value Δz_0 chosen by the operator before scanning (Figure 2.10) [51]. The accuracy can reach a value of almost 0.01 Å and a superficial topographic map at the nano-scale can be acquired, assigning the variance from the set parameter to each pixel of the scan area [57].

Piezoelectric trasducers have the ability of changing dimensions when exposed to electric fields. The scanner can be composed of a single tubular element, with a particular configuration of electrodes that can be seen in the right part of Figure 2.13. There is a single electrode inside, while the external one is divided into four sectors. A difference in potential between the internal and external electrodes leads to a lengthening or reduction of the tube, while a bipolar tension in two opposite sectors of the external electrode causes a tube bending. The first movement is correlated to a vertical deflection of the cantilever (z axis), while the latter allows an xy-scanning [51]. NT-MDT AFM employs a tubular scanner like the one described above, while Park has decoupled xy and z scanner stages allowing for reduced image distortions. Several phenomena in piezoceramic materials can occur and introduce errors and distortions in map acquisitions. First of all, a non-linear function correlates the deformation and the electric field: with fields of high intensity, typically above 100 V/mm, the linearity is compromised and a curved image occurs. Moreover, the feedback loop can have a delayed reaction to an abrupt and fast change of the voltage, creating further distortions in AFM images. At last, a little hysteresis phenomenon correlates the piezoelectric deformation to the sign of previously applied electric field [51]. In Figure 2.14 all phenomena are illustrated. In order to avoid a deformation of the AFM map, small electric fields are applied and delays in the control system are introduced.

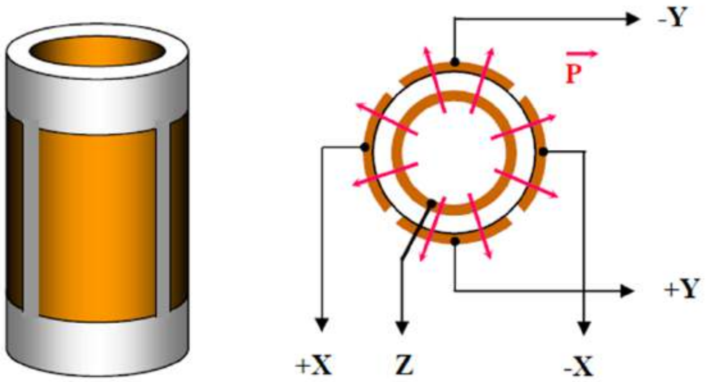

Figure 2.13: Schematic view of tubular transducer structure [51].

In every SPM, the sample-tip system is an oscillating system with its resonance frequency ω_{res}. External mechanical vibrations with frequencies

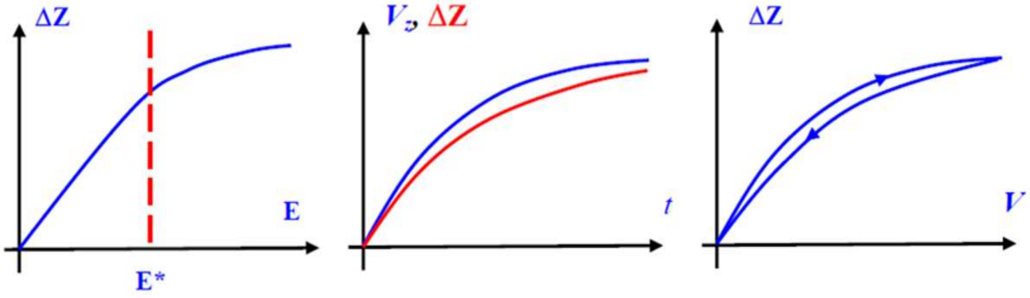

Figure 2.14: From the left, non-linearity effects of the piezotube deformation from the applied electric field. Time diagrams of changes in control voltages during scanning (blue lines) and of the corresponding scanner shifts along Z axis (red lines), due to creep effect. Dependence of deformation from the value and direction of control tension, correlated to hysteresis phenomenon [51].

near ω_{res} can produce periodic fluctuations in the maps of the sample. To reduce this effect, several anti-vibration systems can be added, both passive and active, in addition to the selection of a tip with a high resonance frequency [51]. Among passive systems, an elastic platform can be inserted under the mechanical apparatus to create a mass-spring system with a very low resonance frequency (i.e. 5 - 10 Hz); an example can be springs employed to suspend the head of the instrument (NT-MDT system used). For what concerns active systems, electromechanical devices with a vibration detector and an actuator, which stabilizes the vibration-insulating platform, are introduced; an example is a balance table, which is employed for the stability of the Park AFM [51].

In an Atomic Force Microscope several modes of operation can be used to investigate different sample properties: non-contact, semi-contact and contact modes [58]. These modes differ in the range of sample-tip distance. Interactions are different when changing this parameter, as can be seen in Figure 2.9. In contact mode, the tip is in contact with the sample and the interaction can be placed in the repulsive region of the curve, below the equilibrium distance r_0; the monitored parameter is the tip static deflection and this also gives contact mode the name of ‘Static AFM’ [58]. Semi-contact and non-contact modes are classified under the name of ‘Dynamic AFM’: the cantilever vibrates close to its resonance frequency and the interaction is correlated to the variation of different parameters. The amplitude, the resonance frequency and the phase shift of the oscillation of a vibrating tip are connected to the tip-surface interactions. For this reason they can be used as feedback parameters to acquire sample topographies [59].

2.2.4 Modes of Operation: Dynamic AFM

The exact mathematical description of the interaction between the oscillating cantilever and a surface positioned at a few nanometers from it is quite complex. However, it can be easily described through approximated models. The probe can be modeled as a point-like damped harmonic oscillator with mass m, spring constant k and damping coefficient β [59]. The general equation for an oscillator in 1D, since only the vertical dimension is considered, is:

$$m\ddot{z}(t) + \beta\dot{z}(t) + kz(t) = \sum_i F_i \tag{2.13}$$

where F_i are the external forces and $z(t)$ is the mass displacement. When there are no external forces, the second term of Equation 2.13 is zero and the solution to this second order homogeneous differential equation can be written as:

$$z(t) = e^{-\gamma t}\left[c_1 e^{+\sqrt{\gamma^2-\omega_{\mathrm{res}}^2}t} + c_2 e^{-\sqrt{\gamma^2-\omega_{\mathrm{res}}^2}t}\right] \tag{2.14}$$

where γ and ω_{res} are respectively:

$$\gamma = \frac{\beta}{2m} \quad \text{and} \quad \omega_{\mathrm{res}} = \sqrt{\frac{k}{m}} \tag{2.15}$$

and c_1 and c_2 are constants correlated to the boundary conditions [59]. In Dynamic AFM, the external forces are due to the a piezo-vibrator, which induces forced oscillations on the cantilever, and to gravity force. The second term is a constant contribute and it only affects the equilibrium point position of the system, without modifying frequency, amplitude or phase of the oscillation; for this reason it can be neglected in calculations [51]. Supposing that the piezo-vibrator exciting force is cosinusoidal, with an angular frequency ω, Equation 2.13 becomes:

$$m\ddot{z}(t) + \beta\dot{z}(t) + kz(t) = ku_0\cos\omega t \tag{2.16}$$

Moving the problem in the domain of complex numbers, the general solution is a superposition of a damped oscillation with decrement $\delta = \omega_{\mathrm{res}}/2Q$ (where Q is the quality factor) and persistent forced oscillations with frequency ω [51]. The amplitude $A(\omega)$ and the phase $\phi(\omega)$ of the forced oscillations can be derived and they are [51]:

$$A(\omega) = \frac{u_0\omega_{\mathrm{res}}^2}{\sqrt{(\omega_{\mathrm{res}}^2-\omega^2)^2 + \dfrac{\omega^2\omega_{\mathrm{res}}^2}{Q^2}}} \tag{2.17}$$

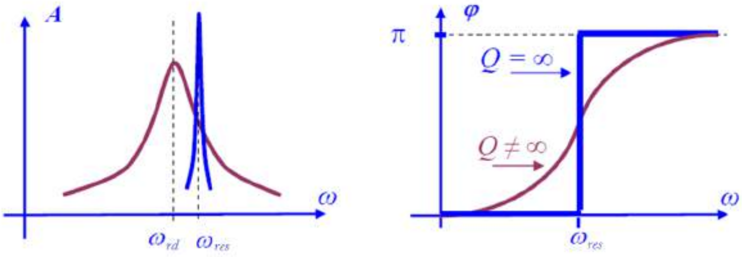

(a) (b)

Figure 2.15: a) Amplitude and b) phase responses with ($Q < \infty$) or without ($Q = \infty$) dissipation. Adapted from [51].

$$\phi(\omega) = \arctan\left[\frac{\omega\omega_{\text{res}}}{Q\left(\omega_{\text{res}}^2 - \omega^2\right)}\right] \tag{2.18}$$

From Equation 2.17 is possible to deduce that the amplitude at the resonance frequency is $A(\omega_{\text{res}}) = Qu_0$, i.e. proportional to the quality factor. Moreover, the dissipation in the system shifts the resonance frequency. Then the response curve shifts toward lower frequencies of a quantity:

$$\Delta\omega = \omega_{\text{res}} - \omega_{\text{rd}} = \omega_{\text{res}}\left(1 - \sqrt{1 - \frac{1}{2Q^2}}\right) \tag{2.19}$$

as can be seen in Figure 2.15(a). In Figure 2.15(b) the phase response with or without dissipation can be appreciated [51].

When the sample is sufficiently close to the oscillating probe, tip-sample forces F_{st} must be considered. These van der Waals forces can be considered as a slowly varying function of the distance [57]. For this reason they may be approximated by the first (linear) term in the series expansion:

$$F_{\text{st}}(z) = F_0 + \left.\frac{\partial F_{\text{st}}}{\partial z}\right|_{z=z_0}(z - z_0) + \frac{1}{2}\left.\frac{\partial^2 F_{\text{st}}}{\partial z^2}\right|_{z=z_0}(z - z_0)^2 + \ldots \simeq F_0 + F_z' z \tag{2.20}$$

where the distance between the tip and the sample ranges around z_0. Summing this term to Equation 2.16 in the excitation forces, it becomes:

$$m\ddot{z}(t) + \beta\dot{z}(t) + kz(t) = F_0 + F_z' z + ku_0 \cos\omega t \tag{2.21}$$

Therefore, the presence of a force gradient results in a change of the effective stiffness of the system:

$$k_{\text{eff}} = k - F_z' \tag{2.22}$$

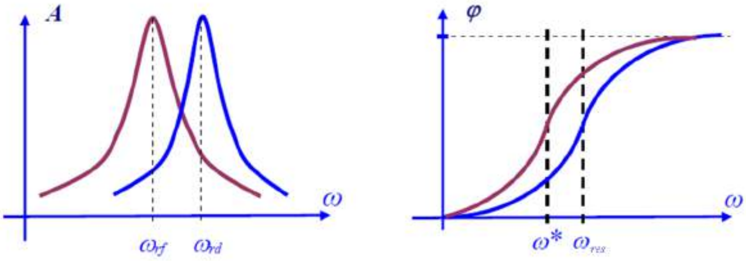

(a) (b)

Figure 2.16: a) Amplitude and b) phase responses with or without sample-tip interaction. Plots adapted from [51].

Repeating the calculations carried out for the free cantilever, amplitude-frequency characteristic and phase response can be derived:

$$A(\omega) = \frac{u_0 \omega_{\text{res}}^2}{\sqrt{\left(\omega_{\text{res}}^2 - \omega^2 - F_z'/m\right)^2 + \dfrac{\omega^2 \omega_{\text{res}}^2}{Q^2}}} \tag{2.23}$$

$$\phi(\omega) = \arctan\left[\frac{\omega \omega_{\text{res}}}{Q\left(\omega_{\text{res}}^2 - \omega^2 - F_z'/m\right)}\right] \tag{2.24}$$

The presence of a gradient in the tip-surface interaction force also results in additional shift of the amplitude and phase response curves. The interaction force determines an additional shift of the amplitude-frequency characteristic:

$$\Delta\omega = \omega_{\text{rd}} - \omega_{\text{rf}} = \omega_{\text{rd}}\left(1 - \sqrt{1 - \frac{F_z'}{m\omega_{\text{rd}}}}\right) \tag{2.25}$$

illustrated in Figure 2.16(a) [51]. From Equation 2.24, the inflection point in the phase response curve shifts toward a point ω^*, with a displacement:

$$\Delta\omega = \omega_{\text{res}} - \omega^* = \omega_{\text{res}}\left(1 - \sqrt{1 - \frac{F_z'}{k}}\right) \tag{2.26}$$

as can be seen in Figure 2.16(b) [51].

At last, the proximity to the sample causes an additional tip phase shift, that is proportional to the force gradient, through the relationship:

$$\Delta\phi \simeq \frac{QF_z'}{k} \tag{2.27}$$

This last effect is employed to acquire phase contrast AFM images [51].

This simplified model illustrates quite well how Amplitude Modulation (AM-) or tapping mode AFM works. In this kind of map acquisition, the cantilever is excited at a fixed frequency, usually near or at the free resonance frequency. Amplitudes in the 10-100 nm range are involved [59]. The great values of amplitude lead the tip get in contact with the sample surface in the lower semioscillation, that correspond to the repulsive region in the force-distance diagram. The working point of the tapping mode can be appreciated in Figure 2.17. Short-range repulsive forces cause an amplitude reduction, which is then indicated by A [60]. The feedback system keeps the normalized amplitude A/A_0 constant during tapping mode imaging to acquire the topography of the surface (A_0 is the oscillation amplitude with the tip far from the sample) [60]. The peculiarity of this mode of operation is the coexistence of two stable oscillation states, a low and high amplitude solution. This presence is due to both attractive and repulsive components in the interaction force, with their non-linear character [59]. During the measurements, the normalized amplitude is set to guarantee an interaction only attractive or repulsive, without allowing a transition between the two states.

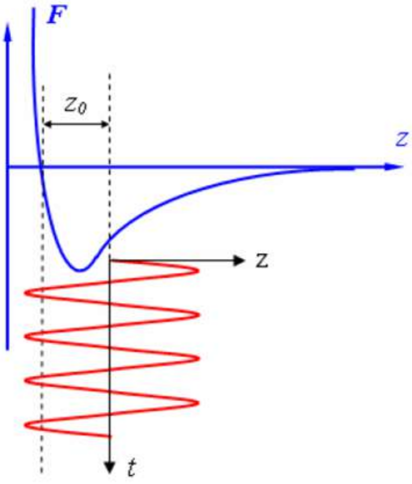

Figure 2.17: Working point in AM-AFM mode of operation in a force-distance diagram [51].

AM-AFM allows to obtain simultaneously both topographic and compositional contrasts in heterogeneous samples [59]. Maintaining the amplitude of the oscillation constant, information on the distance between the tip and the sample is collected, that is the morphology of the sample. If, on the other hand, a variation of the phase is registered, then information on the type of

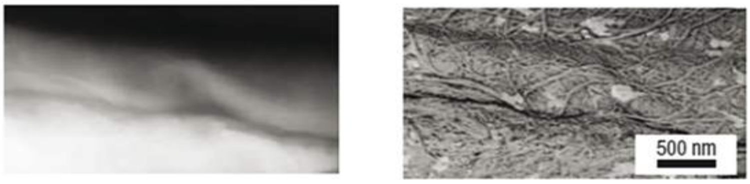

(a) (b)

Figure 2.18: a) Topography and b) phase image of the same area of a wood-pulp fiber [60].

atoms that constitute the sample is taken. Since phase shifts are closely related to tip-surface inelastic processes, the acquisition of phase imaging can lead to information of energy dissipation processes at nanometer scale [59]. The correlation between phase-shift measurements and energy-dissipation values enables to investigate material properties such as stiffness, elasticity, viscosity or surface-adhesion energy [60]. The phase-shift lag $\Delta\phi$ is related to the normalized amplitude, the average energy dissipated in the sample E_{dis} and in the environment E_{med} when $\omega = \omega_{\text{res}}$, with the relationship:

$$\sin\left(\Delta\phi\right) = \frac{A}{A_0}\left(1 + \frac{E_{\text{dis}}}{E_{\text{med}}}\right) \tag{2.28}$$

With A/A_0 and E_{med} maintained constant during AM-AFM imaging, the change in phase shift is strictly related to a local change in the energy dissipated in the sample under investigation [60]. Typical dissipated values per cycle for high resolution experiments are in the 0.5 - 50 eV range, which imply a dissipated energy per bond from 0.001 to 0.1 eV, for a spatial resolution of 2 nm [60]. Figures 2.18(a) and 2.18(b) illustrate the topography and the phase image, respectively, of a wood pulp fiber. Topography image shows height variations in the micrometer range, while is uninformative about the sample composition. In contrast, phase image reveals also white deposits of different composition (amorphous lignin) [60]. Tapping-mode AFM has provided a variety of non-destructive ways to image heterogeneous materials in their natural environment and state with high spatial resolution [60].

This mode of acquisition is employed to obtain both topography and phase maps of the sample with NT-MDT AFM.

Non-contact mode is also called Frequency Modulation AFM (FM-AFM), since frequency shift and excitation amplitude are used as feedback parameters to track topography and composition of a surface [59]. In this type of scanning, the equation of motion is formally identical to Equation 2.21, apart from the excitation term which is no longer a pure harmonic driving force and it is quite complicated. In FM-AFM regime, tip deformation and friction effects are eliminated; thanks to this feature, this technique is a promising way to achieve true atomic resolution. UHV measurements can be performed, contrary to AM-AFM. Indeed, in the latter operation mode very high values of the quality factor Q, due to UHV environment, would reduce the bandwidth of the system in slope detection [59]. In both cases, the increase of the factor Q implies extremely slow feedback responses. In FM-AFM mode, the cantilever is kept oscillating at its current resonant frequency, which differs from the initial resonant frequency for the tip-sample interaction, with a constant amplitude. During the scanning, the distance from the surface is varied to maintain a constant frequency shift; in this way the topography is acquired [59].

FM-AFM mode is employed in topography acquisitions by Park AFM, in what is called True Non-Contact$^{\text{TM}}$ Mode. In this new technology, the spacing between the tip and the sample is of the order of tens to hundreds of angstroms [61]. A stiff cantilever is employed with relatively high resonance frequency, between 100 and 400 kHz with a vibration amplitude of few nanometers [61]. The sensitivity of this technology is raised by a very fast tracking of changes due to tip-sample interaction thanks to the employment of a very high performing z-servo feedback [62]. True Non-Contact$^{\text{TM}}$ Mode is actually the best choice for high resolution imaging, with angstrom vertical resolution, without damaging the sample [61].

2.2.5 Modes of Operation: Static AFM

In the repulsive region of the interaction, the curve has a steep slope, so very little variations of sample-tip distance produce large changes of the interaction force [51]. When the probe is far from the sample, the reflected beam must be positioned at the center of the photodiode; this forces both DFL and LF to be zero. When the tip lands on the sample, the surface applies a pressure on it, bending the cantilever. This bending deflects the beam and changes DFL value [63]. Pressure can be controlled by the user changing SetPoint parameter, that is linked to the electrical DFL signal when the tip lands at the sample. Selecting the right value for this parameter is always a consequence of a compromise: great pressures lead to a great stability and sensibility, as well as to a rapid damage of the tip or the sample.

Contact mode topography can be carried out maintaining a constant height or a constant force between the sample and the tip [51]. In Constant Height mode of operation the scanner of the AFM maintains the fixed end of the cantilever on a constant height value. So, deflection of the can-

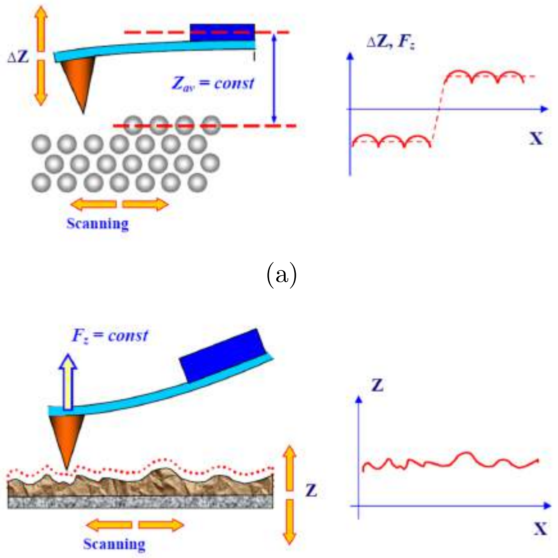

(a)

(b)

Figure 2.19: a) Constant Height and b) Constant Force topographies [51].

tilever is measured and reflects topography of sample under investigation (Figure 2.19(a)) [64]. Despite high scanning speeds that can be reached, this mode of operation has a great disadvantage: it can only be used with samples sufficiently smooth. Heights can produce artifacts due to great bending of the tip and, in the worst cases, tip can broke or sample can be destroyed by scratching of the probe [64]. In Constant Force mode, the deflection of the cantilever is maintained constant by the feedback circuit. The topography of the sample is created by the vertical displacement between the tip and the surface during the scanning (Figure 2.19(b)). The main advantage of this operation mode is its possibility of high resolution measurements of both topography and other local properties of the sample, i.e. friction forces, spreading resistance, etc [64]. For this reason, this technique is preferred rather than the previous one, even though its restricted speed of scanning correlated to the response time of the feedback system.

It is possible to investigate on characteristics of the sample, other than the topography. If the tip is conductive, an acquisition of nano-scale spreading resistance of the sample can be possible [65]. If a voltage bias is applied to the tip, the resulting current through the sample can be measured as a function of the tip position on the surface, during the acquisition of topography in Constant Force mode. If the tip-surface contact resistance is constant during the scanning, the measured current for a given bias is proportional

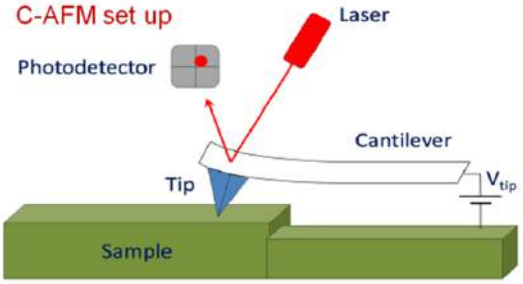

Figure 2.20: Schematic view (not in scale) of a C-AFM setup [41].

to the local resistivity of the sample [65]. A typical C-AFM setup is illustrated in Figure 2.20, in which a bias voltage is applied to the tip, while the sample is grounded [41]. In specific points chosen from the researcher, IV characteristics can be acquired; the system linearly varies the bias applied to the tip and the current that is consequently produced can be registered. Spreading resistance imaging can be also applied to samples with complicated structures, to study the privileged paths of current and changes in electrical resistance due to differences of composition [65].

A particular innovation in conductive-AFM (c-AFM) measurements is PinPoint^{TM} c-AFM [66]. With this new technique current can be measured repetitively in one specific location of the sample surface, with the possibility of varying tip pressures. In PinPoint^{TM} Conductive mode, the tip approaches towards the sample surface until a predefined threshold point, measures the Z scanner's height and, after the acquisition, it rapidly retracts. In this way, measurements of very high accuracy and precision can be achieved, allowing a frictionless conductive scanning with reduced tip deterioration [66]. The tip can approach the same point several times and then record the mean value of all acquisitions; this procedure can be reproduced in all points of a selected grid of the sample surface. The acquisition takes a longer time with respect to a classical c-AFM scanning; is useful then to select a small interesting area of the sample for the acquisition. Figures 2.21(a) and 2.21(b) show topography and current maps, respectively, of nc-SiO_xN_y sample E 3h annealed, acquired with Pin Point technique. For this acquisition, the tip goes up-and-down 5 times and current is measured each time at the threshold z-point. The result is an average of the data and this procedure is repeated for each point of the map.

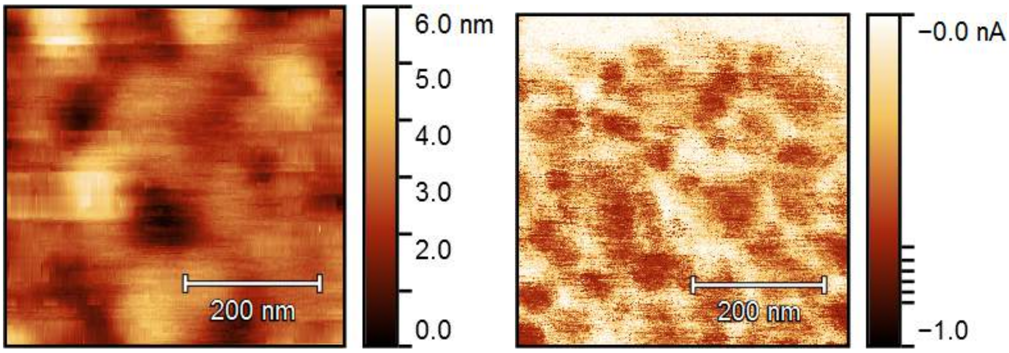

(a) (b)

Figure 2.21: a) Height and b) current maps of nc-SiO_xN_y sample E 3h annealed acquired with Pin Point technique with an applied bias of -0.1 V.

2.2.6 Image Processing

An Atomic Force Microscope is a complex apparatus and both hardware and software parts play a fundamental role in the acquisition of non distorted images of the sample. Software also includes routines for image acquisition and analyses. For the acquisition of *a*- and nc-SiO_xN_y maps the software supplied by the device has been employed: NOVA and XEP, for NT-MDT and Park AFMs, respectively [67, 68]. A software called *Gwyddion* has been employed to obtain all analyses of the samples, for its versatility and completeness [69]. AFM images can be affected by several distortions, due to apparatus imperfections or interactions between the tip and the external ambient [51]. Therefore, AFM data require special processing in order to eliminate these artifacts [70]. Artifacts can occur as a result for wrong choices of the acquisition parameters, for example, SetPoint, scanning rate, as well as feedback or lock-in gains. In tapping mode acquisition, a wrong SetPoint can create instability between the attractive and repulsive modes, causing scars or even big spots along the scanning lines, as Figure 2.22(a) and 2.22(b) show. High values of the SetPoint, if the area to scan is large and rough, can bring the tip at heights high enough to loose interaction with the sample during the investigation (Figure 2.22(c) and 2.22(d)). Furthermore, too fast or too slow scanning rates can stretch the image in one direction and tense it in the other one giving birth to a distorted map; an example of this distortion is in Figure 2.23(a) and 2.23(b). At last, an elevated increase of the pre-amplifier gain factor can generate very noisy acquisitions (Figure 2.23(c) and 2.23(d)). Most of these distortions are difficult to remove even by means of software processes; for this reason, a careful choice of these parameters have to be done before the scanning in order to obtain good quality maps. Nevertheless, some adjustments can be performed through Gwyddion software processes.

2.2.7 Image Processing: Subtraction of polynomial surfaces

Surface images usually show inclination. This effect is due to several reasons. Indeed, inclination may be a result of a tilted installation of the sample onto the scanner or caused by non-flatness of the sample itself; it might be correlated to a temperature drift for the tip shifting with respect to the sample; it could be linked to non-linearity of the piezo-scanner movement, which were described in Section 2.2.3. If the image is inclined, this slope takes a large portion of z-axis, with the effect of losing the clearness of small image details [51]. Moreover, the non-linearity and hysteresis phenomena of the scanner are not completely removed by the device hardware and the choice of scanning mode. Therefore, shifts in the tip-surface distance occur during the xy-scanning, leading to surface images as superposition of the real topography and a surface of the second (or higher) order [51, 70]. For this reason, plane leveling is usually one of the first processes applied to raw SPM data. A polynomial plane that fits the data is then subtracted [69]. Figure 2.24(a) shows the image of an a-SiO_xN_y sample as acquired, while in Figure 2.24(b) a polynomial plane is subtracted by a software tool.

2.2.8 Image Processing: Filtering

Another distortion is due to the continuous changes in the tip-sample distance during scanning, for micro-movements in elements of the head structure or capture by the tip apex of a micro particle from the ambient. These events produce steps parallel to the direction of scanning on the acquired image. A procedure of line-by-line average can remove such defects, as can be seen in Figure 2.24(c) [51].

Local faults of the closed loop can occur during the scanning and, therefore, scars, stripes or strokes can appear and corrupt the SPM image and they are usually parallel to the scanning axis. With a Gwyddion function, these scars can be found and removed, using neighbourhood lines as a reference to fill-in the gaps [69]. An example of this processing is shown in Figure 2.25(a) and 2.25(b).

Fourier filtering can be used, in order to eliminate luminous spots of the transformed image linked to noise sources. This process requires the ability

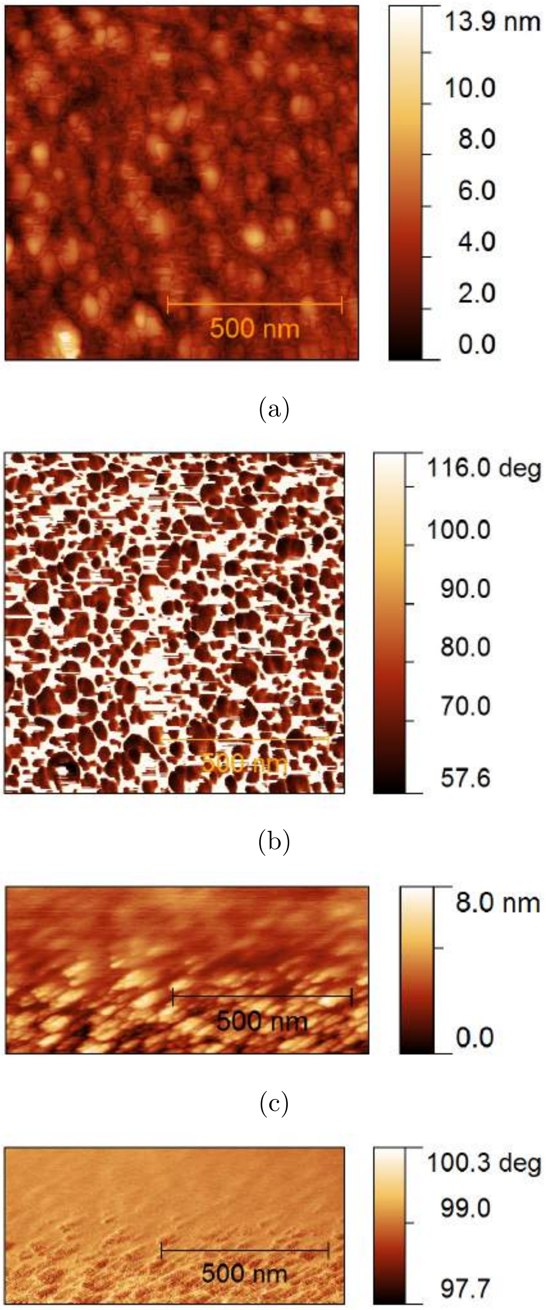

(a)

(b)

(c)

(d)

Figure 2.22: a) Instability due to a wrong choice of parameters in topography and b) phase maps. c) Loss of interaction in topography and d) phase maps.

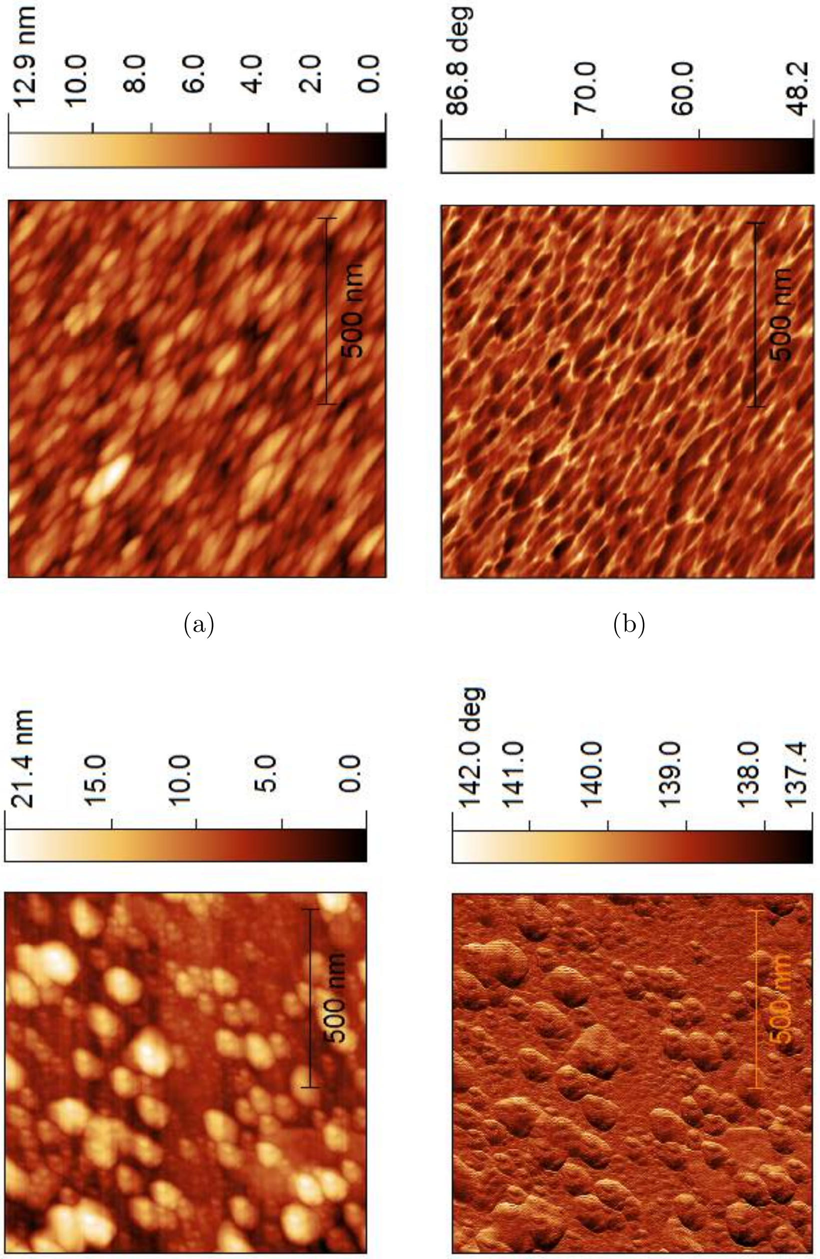

(a) (b)

(c) (d)

Figure 2.23: a) Stretching and distortion in a topography and b) phase maps. c) Noisy topography and d) phase maps. [51].

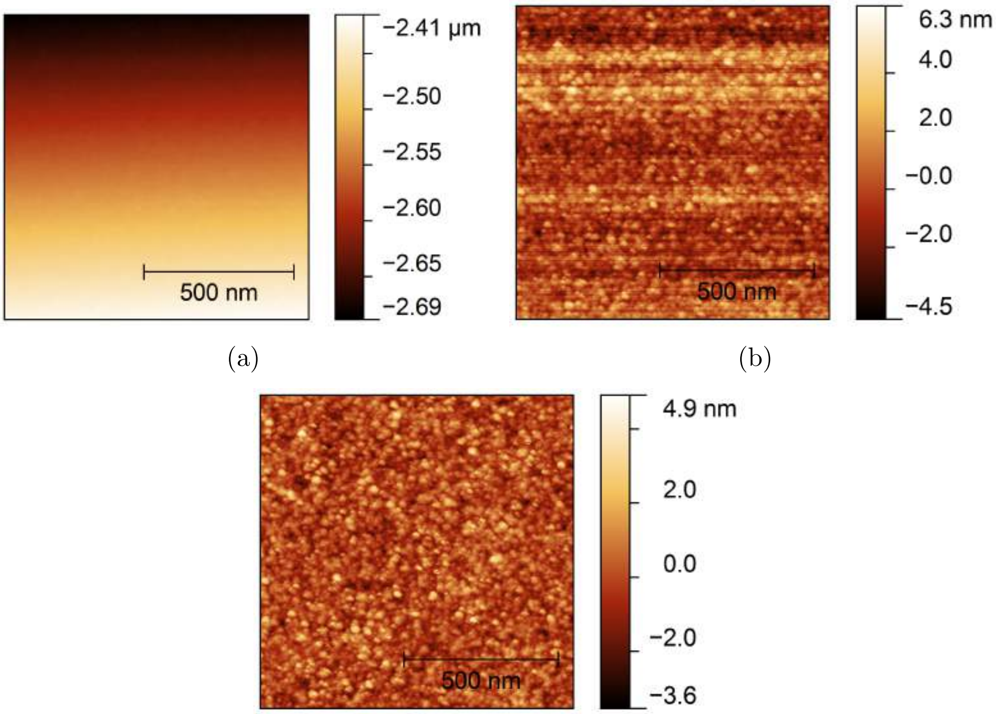

(a)

(b)

(c)

Figure 2.24: An image of an a-SiO_xN_y sample is shown: a) as acquired, b) with a polynomial surface subtracted, c) after a line averaging.

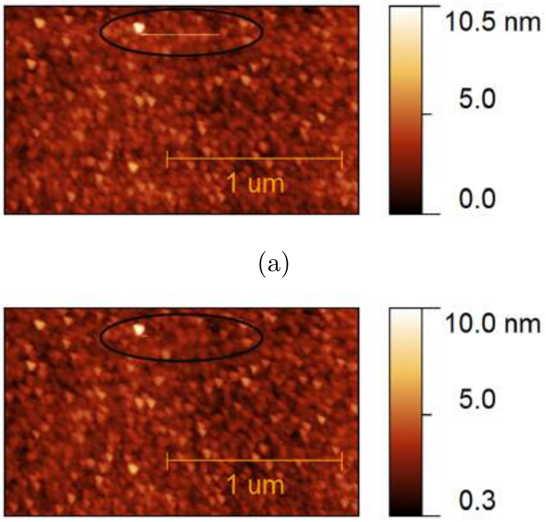

(a)

(b)

Figure 2.25: A partial distorted image of an a-SiO$_x$N$_y$ sample is shown: a) before and b) after a scar correction.

of the researcher to correctly identify the spots, since a wrong choice can lead to signal loss. However, the Fourier transform of the map can be employed to prove that the steps of image processing are correct or to remove periodic oscillations due to acoustic noise [71, 72, 73].

2.2.9 Image Processing: Tip convolution

One of the intrinsic limits of SPM scanning is the finite size of the tip. This property causes distorted surface features in size and shape, especially in samples with high aspect ratio irregularities (i.e. a high ratio between vertical and horizontal dimensions) [51, 70]. Each data point in the image always represents a spatial convolution of a tip and a surface geometry. If the tip radius is smaller than the peak (valley) size, the image of a feature closely approximates its real size and shape. On the other hand, if the tip radius exceeds the size of a peak (valley), the image considerably widens and the effect of the tip shape becomes relevant [70]. If the tip has a known shape, the real SPM image can be partially reconstructed with digital manipulation. The most effective mode of reconstruction is numerical deconvolution, using the tip image obtained experimentally by scanning test structures with a well-known topography. A figurative example is shown in Figure 2.26(a) and 2.26(b), where the tip shape is described by the function $P(x)$, the

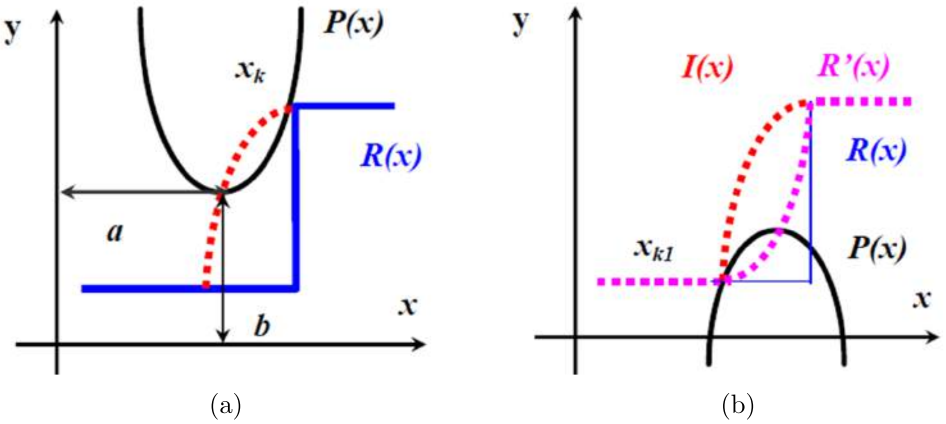

Figure 2.26: a) Schematic view of image acquisition b) and restoration processes [51].

surface topography by the function $R(x)$ and the SPM image is given by $I(x)$. Subtracting the tip shape to the SPM image (point per point procedure), a restored image $R'(x)$ can be achieved [51]. This operation is successful only if the tip is small enough to touch all points of the surface once at the time.

Most common procedures involve special test structures with known topography and a periodic pattern, used for calibration and determination of the form of the working part of the tip.

In addition to the intrinsic limits due to its finite size, the tip can cause further artifacts if it is broken or damaged. The constant rubbing with the surface, several landings, together with the presence of micro-particles of dust on the sample, compromise the tip integrity, with a consequent increase of its radius. As a consequence, a series of identical structures with the same orientation appear in the acquired map, loosing the real image and structures of the sample. An example is shown in Figure 2.27(a) and 2.27(b). In conductive-AFM measurements, high current peaks, the presence of rough structures or the unavoidable degradation due to a prolonged use of the same tip can erode the conductive coating, making the tip useless to investigate the nano-scale electrical properties of the sample (Figure 2.27(c)).

In this work, a preliminary calibration procedure in the z direction has been done and periodically repeated during the measurements [65]. Gratings of a well-known step structure with different heights are employed, to control and correct the sensitivity of the device. Several maps of different areas of all the sample have been acquired, to verify the reproducibility of the measurements. A particular attention was given to the instrument setup and the best upstream choice of the parameters before the acquisition. Lots

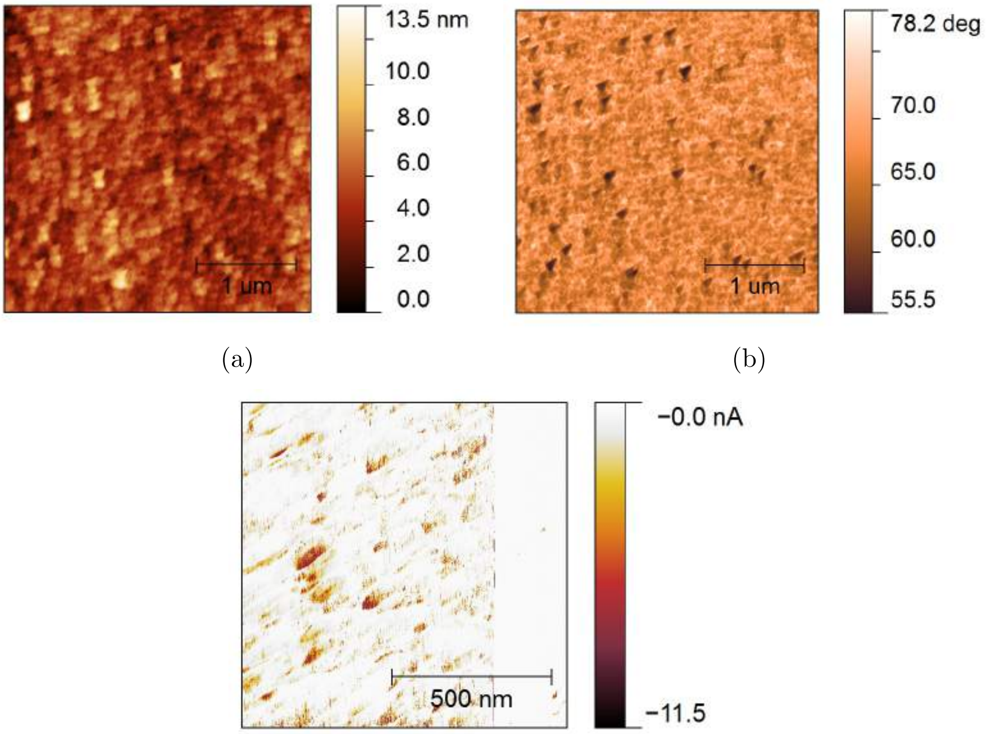

(a)

(b)

(c)

Figure 2.27: a) The tip degradation causes repeated triangle figures in both topography and b) phase maps. c) In the right part of this current map, the tip has lost its conductive coating.

of images with distortions or artifacts that could not be avoided by software processing were discarded. A gallery of some artifacts that can be seen during the experimental work is shown in the Appendix. Whereas, maps evaluated good enough to be investigated in morphological and electrical characterization underwent all steps of image processing described in the previous paragraphs, before the statistical analysis.

2.2.10 Morphological analysis

After all image processing described in Sections 2.2.6 to 2.2.8 is done, topography maps of the samples are ready for morphological analysis. Maps in attractive tapping mode or non-contact mode are used for this type of investigation, since they have the highest resolution in the z direction. A morphological analysis of samples deposited with different parameters helps in understanding how and if different choices can affect structural properties.

A first step of the statistical analysis is done using Gwyddion 2.38 tools. In this way it is possible a quick estimation of statistical parameters and functions about the surface roughness, as well as grains dimensions and arrangement [69].

Among several statistical quantities that can be extracted, the following were considered the most significant to have a global and complete range of sample morphological properties. First of all, Gwyddion tools allow to obtain statistical parameters of surface roughness. Considering an AFM map as a matrix, numerical characteristics of each row or column can be extracted as functions of their position and an average value with its error is directly calculated by the tool [69]. In this way, two statistical parameters can be obtained: Roughness Average R_a and Root Mean Square Roughness RMS.

R_a is the arithmetical mean deviation of all points from a mean value, that is:

$$R_\mathrm{a} = \frac{1}{N}\sum_{j=1}^{N} |r_j - \bar{r}| \tag{2.29}$$

where N is the number of pixels on a row/column, r_j is the value of the j-th point and $\bar{r}$ is the mean value over the evaluation length [69].

On the other hand, the Root Mean Square (RMS) roughness can be obtained as is the standard deviation of the points from the mean value [69]:

$$\mathrm{RMS} = \sqrt{\frac{1}{N}\sum_{j=1}^{N} (r_j - \bar{r})^2} \tag{2.30}$$

In order to reduce noise effects over the scanning line, both R_a and RMS can be calculated row/column wide and their average over the map, respectively called R^* and R_q, can be suited as an estimation of the surface roughness [69].

Another powerful one-dimensional statistical function is the Height-Height Correlation Function (HHCF)supplied by Gwyddion tools, defined as [69]:

$$\mathrm{HHCF}(r) = \frac{1}{N(M-m)} \sum_{l=1}^{n} \sum_{n=1}^{M-m} \left(z_{n+m,l} - z_{n,l}\right)^2 \tag{2.31}$$

where N and M are the dimensions in pixels of the map, z is the recorded height for each point of the matrix and m is linked to the sampling interval Δx of the AFM measurement, as follows [69]:

$$m = \frac{r}{\Delta x} \tag{2.32}$$

in which r is the lateral separation of two surface heights [74]. This function can be obtained by using Gwyddion tool and can be used to extract useful parameters describing surface features. Assuming the surfaces of all the samples approximately self-affine, the HHCF can be written in a simple exponential form and several parameters can be estimated from it [74]. Within the self-affine model, a surface isotropic profile $z(x)$ follows the equation:

$$|z(x+r) - z(x)| \sim (mr)^\alpha \tag{2.33}$$

where the exponent α is called the roughness exponent for the surface and m denotes the local slope of the surface profile [41, 74]. The left-hand side of Equation 2.33 represents the local roughness of the surface. In one dimension it follows that:

$$|z(\epsilon x + \epsilon r) - z(\epsilon x)| \sim (\epsilon m r)^\alpha \tag{2.34}$$

and this equation can be rearranged in the form [74]:

$$|\epsilon^{-\alpha} z(\epsilon x + \epsilon r) - \epsilon^{-\alpha} z(\epsilon x)| \sim (mr)^\alpha \tag{2.35}$$

Comparing Equations 2.33 and 2.35, the profile can be expressed as:

$$z(x) \sim \epsilon^{-\alpha} z(\epsilon x) \tag{2.36}$$

and a profile with such property is called self-affine [74]. α represents the short-range roughness of a self-affine surface: larger values of α ($\alpha \approx 1$) corresponds to a rougher profile, while small values ($\alpha \approx 0$) are linked to smoother ones [74]. Examples of two surfaces with different values of α are

Large α ($\alpha \approx 1$)

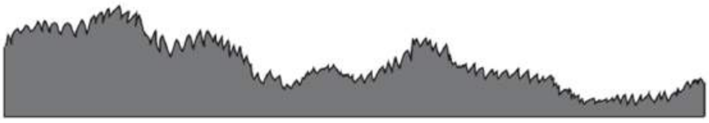

Small α ($\alpha \approx 0$)

Figure 2.28: Local surface morphology for surfaces with different values of α ($0 < \alpha < 1$). Top figure: smoother surfaces with larger values of α. Bottom figure: rougher surfaces with $\alpha \sim 0$ [74].

depicted in Figure 2.28. It can be noted that surfaces with different α values could give rise to very similar roughness values.

If the surface height profile obeys Equation 2.36, then the correlation functions have analogous scaling properties [74]. For an isotropic self-affine surface, HHCF of Equation 2.31 can be fitted by the functional form:

$$\mathrm{HHCF}(r) = 2R_{\mathrm{HHCF}}^2 \left[1 - \exp\left[-\left(\frac{r}{\xi} \right)^{2\alpha} \right] \right] \tag{2.37}$$

where R_{HHCF} represents the surface roughness, α is the roughness exponent and ξ is the lateral correlation length [74, 75]. ξ can be defined in this way: two surface heights are significantly correlated on average if their lateral separation r is less than the lateral correlation length [74]. Moreover, this quantity gives information about grains arrangement in the sample. Finite sampling produces a HHCF oscillatory behavior for $r >> \xi$ (Figure 2.29(b)) with respect to a simulated surface (Figure 2.29(a)) [74, 75]. When several maps are acquired, the average HHCF (thick line) exhibits a reduced oscillatory behavior with respect to single maps (thin lines), as Figure 2.29(b) shows [75]. Therefore the acquisition of several AFM maps can be considered equivalent to a more extended sampling. This choice can lead to an accurate estimation of the roughness parameter and the lateral correlation length, maintaining a high resolution on each single map [41].

At the end of this part of the analysis, the roughness R_{HHCF} obtained from the fitting of the HHCF can be compared with the average values of R^* and R_{q} [41].

The Segmentation method is the powerful tool implemented by the soft-

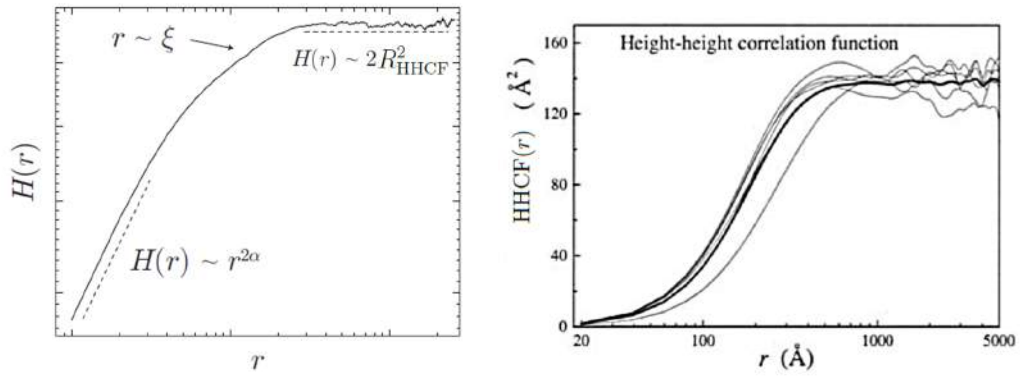

(a) (b)

Figure 2.29: a) HHCF obtained from a simulated self-affine surface. The plot is on a log-log scale. Adapted from [74]. b) HHCF calculated from the AFM images scanned from the amorphous Si film, where the thin curves are obtained from different single images, while the thick curve represents the average of ten thin curves. Adapted from [75].

ware Gwyddion for marking and segmentation of the grains [69]. This new method is an implementation of watershed algorithm. This algorithm is based on immersion simulations, where the valleys of the surface are progressively flooded with liquid. This powerful method provides high accuracy and high speed of segmentation [76, 77]. The result is the original AFM map with a superimposed segmentation map, in which each pixel belongs to one grain or separates two of them. An example of an original map, with a superimposed segmentation mask and inverted segmentation mask, are illustrated in Figures 2.30(a), 2.30(b) and 2.30(c), respectively. Through this procedure, statistical values on grains can be achieved. By default, the algorithm marks valleys; anyway, it is possible to mark upward grains ticking off the option 'Invert height' [69].

The pre-processing procedure involves the choice of several parameters [69]. A right choice of the parameters creates a mask that perfectly matches the map under investigation. In Section 3.1 a deep analysis on how a non accurate choice of parameter can affect the statistical characteristics of the grains is performed. All parameters with their range and a brief description of how they work in the algorithm are listed in Table 2.1.

Different inaccuracies can occur during the identification: grains can be incorrectly merged in a single one, an individual grain can be split in several ones and experimental noise can be identified as a very small grain. The first two cases can be minimized with optimized segmentation parameters.

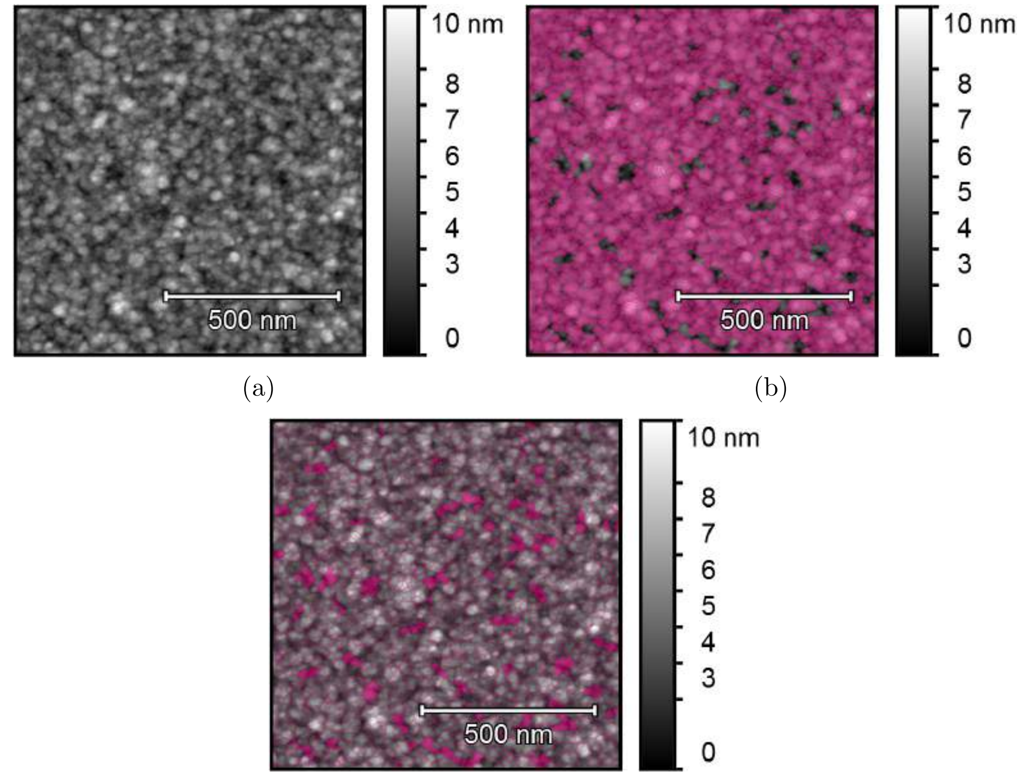

(a)

(b)

(c)

Figure 2.30: a) AFM morphology map of nc-SiO_xN_y C sample 0h annealed; b) the same map with a superimposed segmentation mask; c) the mask is inverted to facilitate the reading of the map.

Table 2.4: List of segmentation parameters with their ranges and a brief description of how they work [69].

Parameter	Brief Description
Gaussian smoothing (GS) (0 - 20) px	Applies a Gaussian smoothing to the grains. A zero value means no smoothing.
Add gradient (AG) (0 - 100) %	Adds relative weight of local gradient to data. Large values mean areas with large local slope tend to become grain boundaries.
Add curvature (AC) (0 - 100) %	Adds relative weight of local gradient to data. Large values mean locally concave areas tend to become grain boundaries.
Barrier level (BL) (0 - 100) %	Relative height level above which pixels are never assigned to any grain.
Prefill level (PL) (0 - 100) %	Relative height level up to which the surface is prefilled, obliterating any details at the bottoms of deep valleys.
Prefill from minima (PFM) (0 - 100) %	Relative height level up to which the surface is prefilled from each local minimum.

To remove the latter, a threshold on the grain size and position has to be applied, after all parameters are set [76]. For this reason, a filter on the area of the identified grains can be applied. In particular, grains with a surface less than the one of a circle with radius equal to the tip radius must be removed. Therefore, a recommended threshold can be:

$$A > \pi r^2 \cdot \frac{(N \cdot M)}{(x \cdot y)} \tag{2.38}$$

where A is the area in pixel of the grains, r is the tip radius, while N and M, x and y are the sizes of the map in pixels and meters, respectively [76]. This can set an inferior limit to the resolution of the map, due to both experimental noise and the convolution of the tip. Another filter can be applied to remove from the statistical analysis regions with low height values, in which resolution can be worse [76]. It has been shown that this filtering process does not remove significant part of the signal [76].

After the segmentation parameters and the threshold are set, several statistical quantities related to the grains can be extracted [69]. For example, the total number of marked grains (NoG), the equivalent square size (or mean grain size MGS) and the equivalent disc diameter (EDD) of the grains can be calculated. MGS approximates a grain to a square and measure its side, while EDD is the diameter of a disc that has the same projected area as the grain, that is [69]:

$$A_{\text{grain}} = [\text{MGS}]^2 = \pi \left[\frac{\text{EDD}}{2}\right]^2 \tag{2.39}$$

Segmentation together with HHCF analyses lead to several statistical properties of the AFM maps. By means of roughness parameters, lateral correlation length and both grains mean number and size, a complete overview of sample morphology can be reached. In this way, the grain dimensions and their arrangement is deeply investigated.

2.2.11 Electrical characterization

The electrical characterization of the samples at the nano-scale can be performed by means of conductive AFM (c-AFM), which was described in detail in Section 2.2.5. A typical setup of acquisition was shown in Figure 2.20. In this mode, it is possible to acquire simultaneously topography and current maps. This double acquisition allows to control and exclude possible artifacts related to the topography [41]. In fact, an increase of current can be associated to a wider contact area. This phenomenon can occur when the tip enters a dip during the scanning. If there is no correlation between height and current profiles, the presence of this kind of artifacts can be excluded [41].

After a scanning session, there is always a surface charge collection in the scanned area. This effect impedes consecutive acquisitions in the same area. For this reason, it is recommended to repeatedly change the scan area. Effects of surface charge accumulation are depicted in Figures 2.31(a) and 2.31(b). The acquisition of this map was possible thanks to the stability of the AFM Park. An area of 1 μm^2 was previously scanned on a nc-SiO$_\text{x}$N$_\text{y}$ sample; then, a larger area of 4 μm^2 was investigated. In Figure 2.31(b) it is possible to locate the area previously scanned, which is not conductive anymore because of the presence of surface charge. A link between scanning and oxidation of the sample can be excluded, because these areas remain not conductive with both positive and negative voltages, the latter not promoting oxidation process on this nc-SiO$_\text{x}$N$_\text{y}$ sample (Figures 2.31(c) and 2.31(d)).

At last, local current-voltage measurements can be carried out through AFM. During these acquisitions a variable bias is applied between the tip and the sample and the current flowing between them can be recorded. In this way the electrical behavior in different points of the maps can be investigated.

It is advisable to employ voltages as low as possible, but high enough to generate detectable currents [78]. With this choice, degeneration of the tip and spikes of high current can be avoided.

By means of all these tools, a thorough study of morphological and electrical properties at the nano-scale can be achieved in *a*- and nc-SiO_xN_y thin layers. All the experimental results are presented in details in Chapter 3.

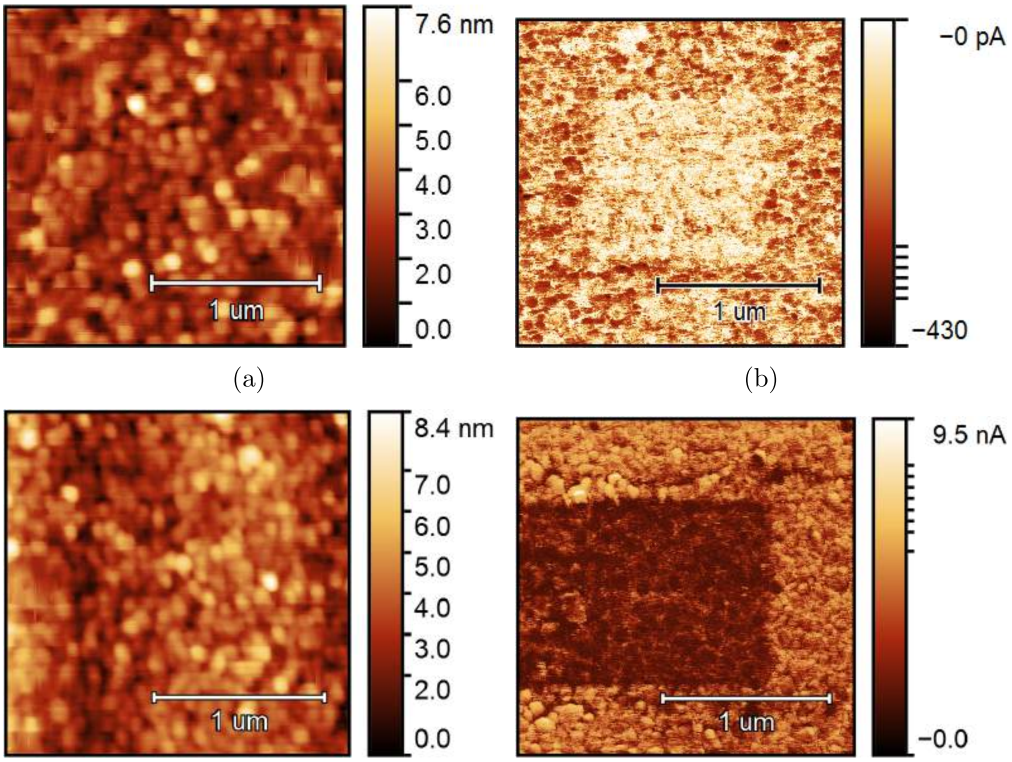

(a) (b)

(c) (d)

Figure 2.31: a) Conductive-AFM acquisition of sample E 3h annealed with an applied bias of -0.4 V of topography and b) current maps. The central area (white zone) in the current map is not conductive anymore, due to a previous scanning. c) c-AFM acquisition of the same sample topography and d) current maps, when a positive voltage (0.4 V) is applied. The black zone is not conductive anymore for a previous scanning on this area. The scale in the current maps is nonlinear.

Chapter 3

Results and Discussion

In the present chapter the experimental results will be reported.

First of all, in Section 3.1 the choice of suitable parameters for morphological studies has been investigated, in order to verify its stability and consistency for $\mathrm{SiO_xN_y}$ thin layers. Secondly, morphological properties of nc-$\mathrm{SiO_xN_y}$ samples will be described in Section 3.2.1, while their electrical characterization at the nano-scale will be analyzed in Section 3.2.2. Thereafter, morphological and electrical properties of a-$\mathrm{SiO_xN_y}$ samples will be illustrated in Sections 3.3.1 and 3.3.2, respectively. At last, the discussion of all the results will be carried out in Section 3.4.

3.1 Morphological AFM analyses: choice of suitable parameters

Due to the fact that Segmentation is a very recent tool, a previous investigation of this new technique had to be done. Both a- and nc-$\mathrm{SiO_xN_y}$ are constituted by very little grains (orders of tens of angstroms or less). In this perspective, it is quite difficult to understand if the choice of segmentation parameters is suitable or not, staring at the mask superimposed on the map. Then, this questions came up in mind: are the mean grain size (MGS) and the number of the grains (NOG) stable with little modifications of these parameters near the set values? How much do they vary far from these values?

To answer these questions five maps of the sample 4 and one for each sample 3 - 1 of a-$\mathrm{SiO_xN_y}$ (500×500 $\mathrm{nm^2}$) were selected. A set of segmentation parameters was selected, considered the most suitable for these maps. This set is listed in Table 3.1. After segmentation a threshold of 2 $\mathrm{px^2}$ is applied, in order to avoid the smallest grains due to experimental noise.

Table 3.1: List of segmentation parameters selected for a-SiO$_\mathrm{x}$N$_\mathrm{y}$.

Parameter	**Value**
Gaussian smoothing (GS)	3.99 px
Add gradient (AG)	100%
Add curvature (AC)	0%
Barrier level (BL)	100%
Prefill level (PL)	0%
Prefill from minima (PFM)	12.35%

These parameters have been varied one at a time, of various percentages with respect to the initial value (Table 3.2). Different percentage variations were used for each parameter, since some appeared to be most influential than others on statistical grain qualities.

Table 3.2: List of all the variation ranges of the parameters in percentages. The parameters are listed in Table 3.1.

Parameter	**Variation range** (%)
GS	[±1, ±50)
AG	[-0.5, -25]
AC	[+0.5, +25]
BL	[-0.5, -55]
PL	[+0.5, +15]
PFM	[±1, ±50]

After a single variation of each parameter, both NOG and MGS (Equation 2.39) were reported and their percentage variation with respect to the initial value (corresponding to the set of parameters in Table 3.1) were obtained. These steps were reproduced for each map of a-SiO$_\mathrm{x}$N$_\mathrm{y}$ samples under investigation. As an example, the plots of two different parameters for a map of sample 4 are reported in Figures 3.1(a) and 3.1(b).

The parameters show the same trend when the analysis is repeated on different maps of the same sample. It follows that segmentation method is reproducible when investigating a single sample. Moreover, the same trend of the parameters is exhibited also for different samples (sample 1-4). Then, reproducibility can be extended to all this kind of materials. For each segmentation parameter setup, the percentage variation of both Number of Grains and Mean Grain Size were estimated. Then, the average and the standard deviation on the five different maps of sample 4 were calculated. All these values are reported in Figures 3.2(a) to 3.3(c) as a function of the percent-

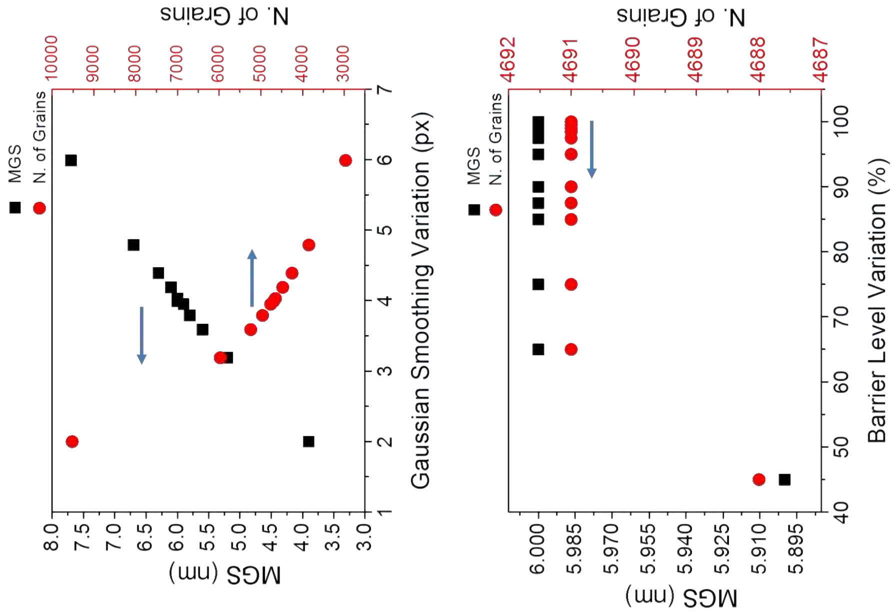

(a) (b)

Figure 3.1: MGS and NOG as functions of a) Gaussian Smoothing and b) Barrier Level variations.

age variation of each single parameter. It follows that segmentation is more sensible to the variation of some parameters rather than others.

In fact, for a variation of the GS parameter below 20% around the selected value, the variation of the MGS is under 15%, whereas that of NOG is under 30% (Figure 3.2(a)). Moreover, when the parameter AG is varied under 15% around the selected value, there is a variation of MGS under 6% and of NOG under 9%. For further deviations of this parameter (up to 25%), the variation of MGS and NOG seems to remain stable (Figure 3.2(b)). The change in AC parameter under 12% leads to a variation under 4% and 5% of MGS and NOG, respectively (Figure 3.2(c)). A very different trend can be appreciated for the BL parameter. In fact, the variation of MGS and NOG is minimal (less than 0.1%) even for a great changes in BL parameter, over 50% (Figure 3.3(a)). A little variation ($< 5\%$) of the PL parameter leads to a variation of about 20% in both MGS and NOG (Figure 3.3(b)). Lastly, a variation under 15% of the parameter produces a little variation ($< 1 - 2\%$) of MGS and NOG (Figure 3.3(c)).

In Table 3.3 all percentage variations of mean grain size when the parameters differ of 5% from the set values are listed. From these trends, it follows that Gaussian Smoothing, Add Gradient and Prefill Level parameters give the widest variation of MGS and NOG, even for little variations of the parameters.

Table 3.3: List of all ranges of parameter variations in percentages that lead to a maximum deviation of 5% of MGS and NOG.

Parameter	**MGS variation** (%)
GS	3.1
AG	1.2
AC	3.1
BL	0
PL	17.6
PFM	0.5

The parameter that mostly influences the analysis is the Prefill Level (PL). This parameter represents a height threshold, below which everything is filled. This is very useful on samples that show wide distributions of the recorded z values, such as nanowires [76]. However, *a*- and nc-$\mathrm{SiO_xN_y}$ thin layers have not a broad z distribution, as they feature low roughness values. The employment of PL values different from zero for this kind of samples is not recommended as it would lead to high errors (Table 3.3).

The other two parameters that mostly affect the value of MGS are the Gaussian Smoothing (GS) and the Add Gradient (AG) ones. A variation of these parameters of 5%, with respect to the optimal set, results in a variation of 3.1%. The contribution of the other parameters is below 1.5% for a variation of 5% from the optimal value (PL variations are not included in this estimation). The contribution of an incorret choice of the parameters is estimated to be below 4% for a variation of the parameters of 5%.

In conclusion, due to what has been previously shown, the segmentation analysis seems to be stable and consistent for this kind of structures.

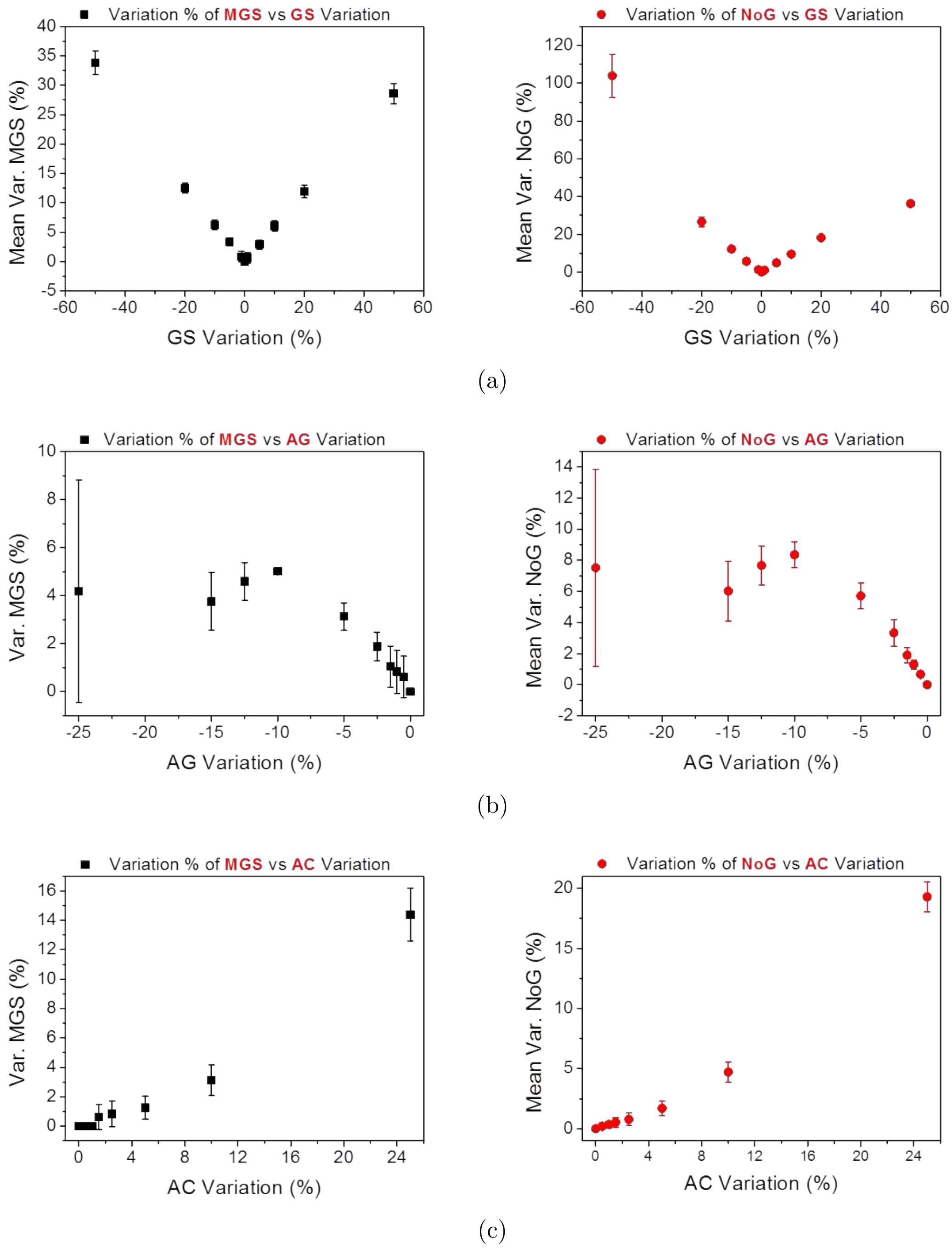

(a)

(b)

(c)

Figure 3.2: MGS and NOG percentage variations as functions of a) Gaussian Smoothing, b) Add Gradient and c) Add Curvature percentage variations of sample 4.

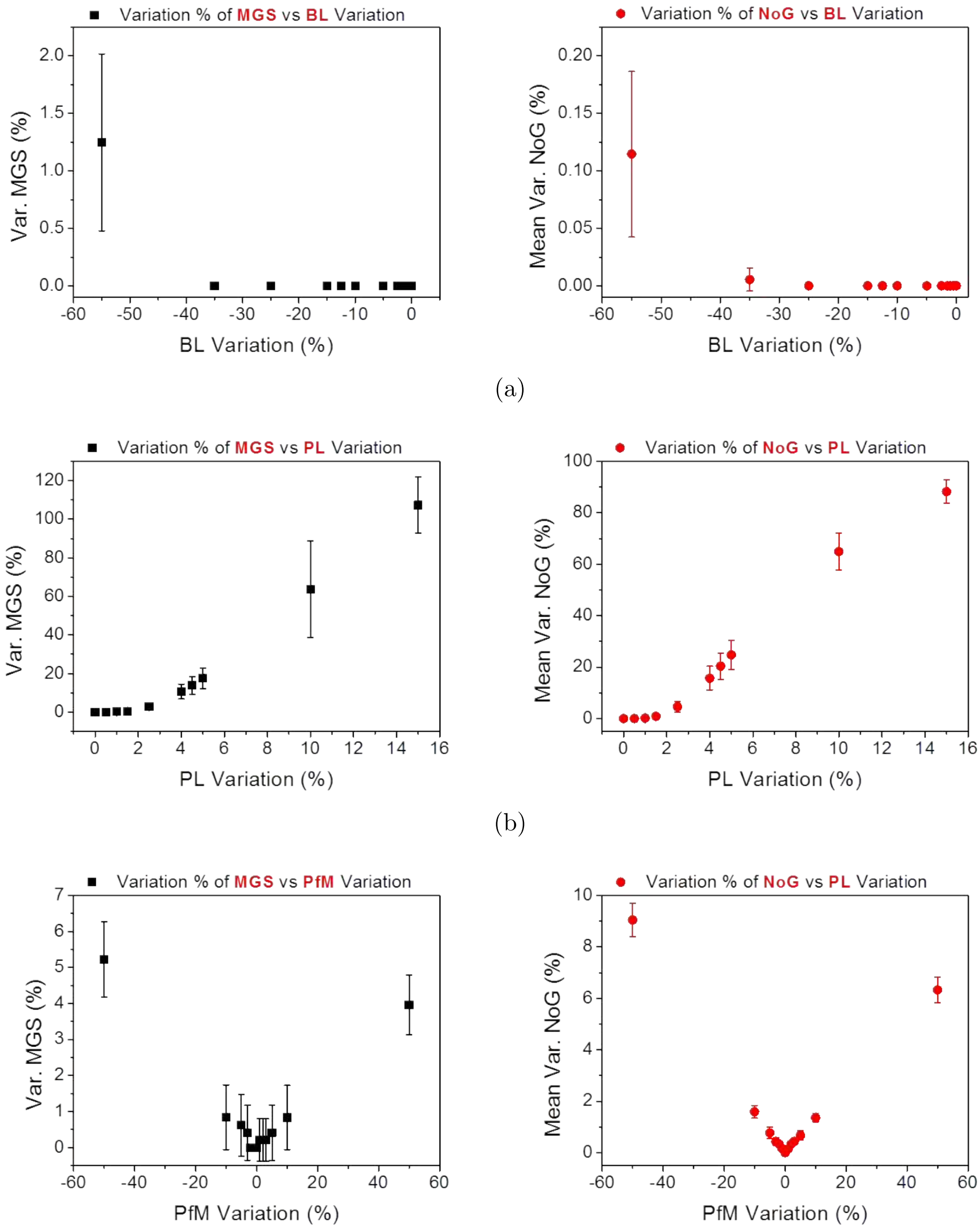

(a)

(b)

(c)

Figure 3.3: MGS and NOG percentage variations as functions of a) Barrier Level, b) Prefill level and c) Prefill From Minima percentage variations of sample 4.

3.2 nc-SiO_xN_y

To collect complete information on their morphological and electrical properties, nc-SiO_xN_y thin layers were investigated by AFM techniques in different modes of operation. Several maps were acquired in attractive tapping mode (Section 2.2.4) for different samples in order to acquire information about their morphology (roughness, lateral correlation length, equivalent disc diameter). On the other hand, repulsive regime in tapping mode was employed to observe differences in the surface composition. Then, c-AFM measurements were performed to investigate the local conductivity of the samples, followed by IV characteristic in different points of the map. All these scanning and analysis aim to understand how both annealing time and different N_2O dilution during deposition affect nano-scale morphological and electrical properties of the samples.

3.2.1 Morphological and Structural Analysis

To investigate the morphology of nc-SiO_xN_y thin films, several maps for each sample C (0h, 3h 6h annealed) were acquired. Maps are 1×1 μm^2 large with a resolution of 512×512 px^2. These maps were acquired with Park NX10 AFM. The best five maps for each sample were selected in order to be analyzed. Maps with tip-sample instabilities, that the software tool was not able to correct, were discarded. As an example, one map for each sample C is depicted in Figures 3.4(a), 3.4(b) and 3.4(c). All maps underwent a process of segmentation. The parameters employed are listed in Table 3.4.

Table 3.4: List of all segmentation parameters employed for C nc-SiO_xN_y samples.

Parameter	**Value**
GS	4.00 px
AG	70%
AC	70%
BL	100%
PL	0%
PFM	12%

After this process, a threshold of 4 px^2 and a filter for the minimum value of +1 nm from the bottom were applied. In order to make the reading easier, a map of sample C 0h annealed with a superimposed inverted mask is illustrated in Figure 3.16. The pink areas of the mask represent portions avoided

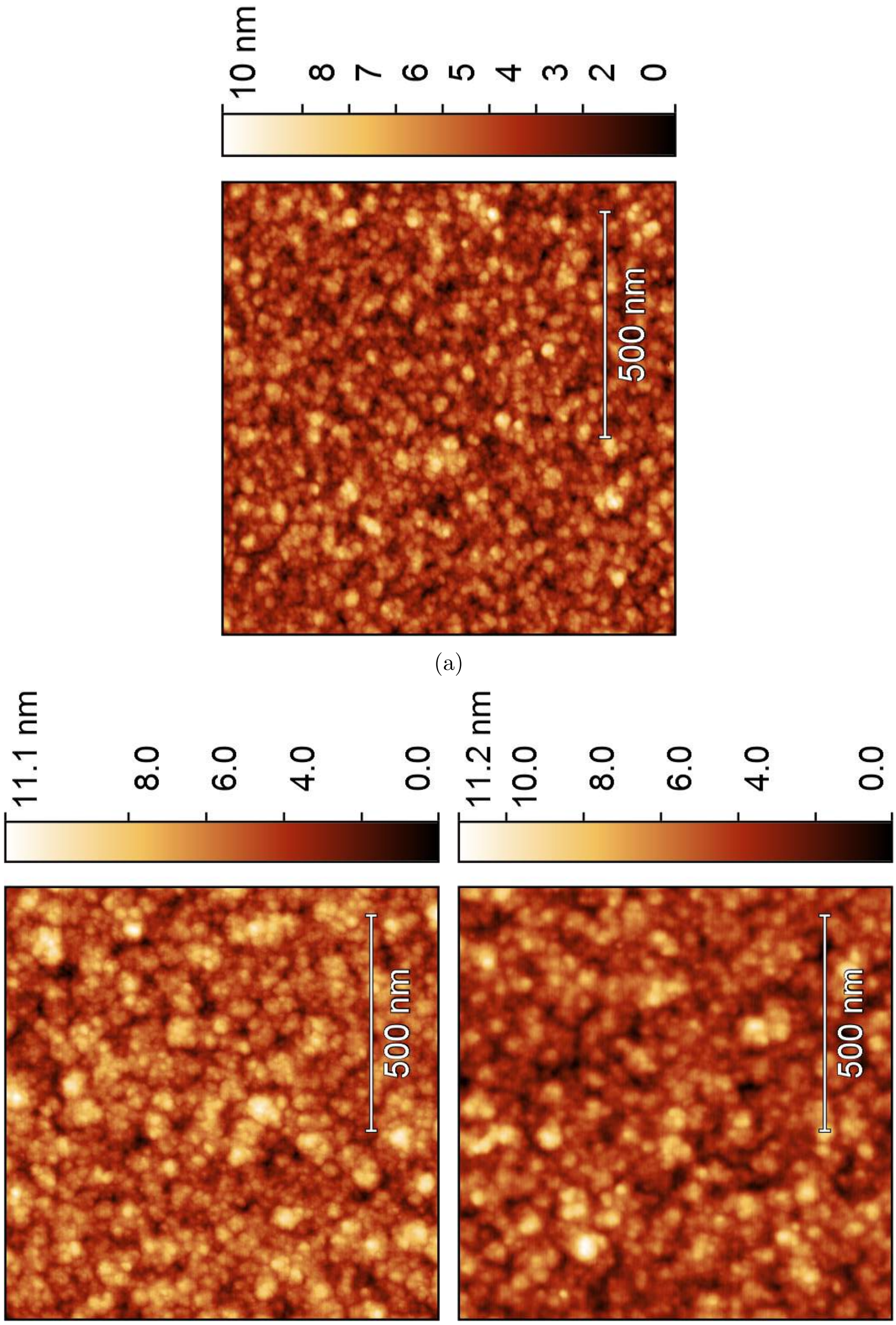

(a)

(b)

(c)

Figure 3.4: AFM acquired topography maps in attractive non-contact mode of sample C a) as-deposited, b) 3h and c) 6h annealed, respectively. The scan area is $1 \times 1 \mu m^2$ with a resolution of 512×512 px^2.

from the two filters, whereas the pink lines locate single grains, separating them from the surrounding ones. From each mask, equivalent disc diameter (EDD) distributions were extracted. This quantity is correlated to the area of the grains through the expression in Equation 2.39 in Section 2.2.10. The mean value of EDD with its standard deviation was evaluated for each sample C. All these values are listed in Table 3.5.

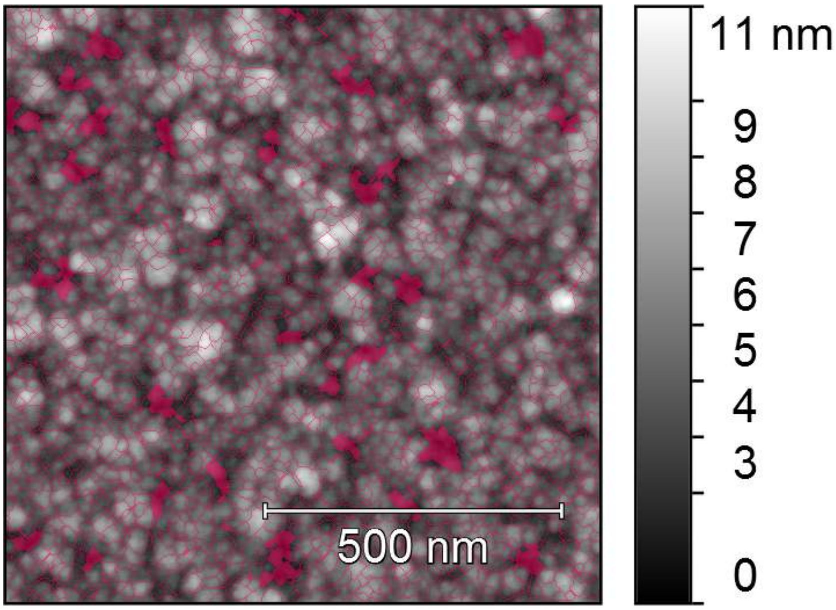

Figure 3.5: Inverted mask superimposed on a map of Sample C 3h annealed of nc-SiO$_x$N$_y$. The parameters of the mask are listed in Table 3.4.

Table 3.5: Mean values with its standard deviation of EDD for nc-SiO$_x$N$_y$ samples C. The errors reported are only the statistical ones.

Sample C	**EDD (nm)**
0h	16.42 ± 0.06
3h	17.12 ± 0.06
6h	19.34 ± 0.08

These values exhibit an increase of the EDD of the grains from the as-deposited sample to the 6h annealed, maintaining the same concentration of N_2O during the deposition. It can be concluded that the dimensions of the grains become larger with introduction of the thermal treatment. The extension of the annealing duration leads to a further increment of the grain dimensions.

Thereafter, HHCF was obtained for each sample C. This function, which is mathematically expressed by Equation 2.31, was fitted with the exponential expression for self-affine surfaces (Equation 2.37). Through this process, roughness parameter R_{HHCF}, lateral correlation length ξ and roughness exponent α were extracted for each map. Then, the mean values and standard deviations of these parameters were calculated for each nc-SiO$_\mathrm{x}$N$_\mathrm{y}$ sample C. Figure 3.6 shows HHCF experimental data (black dots) and their relative fit (red line) for sample C 3h annealed.

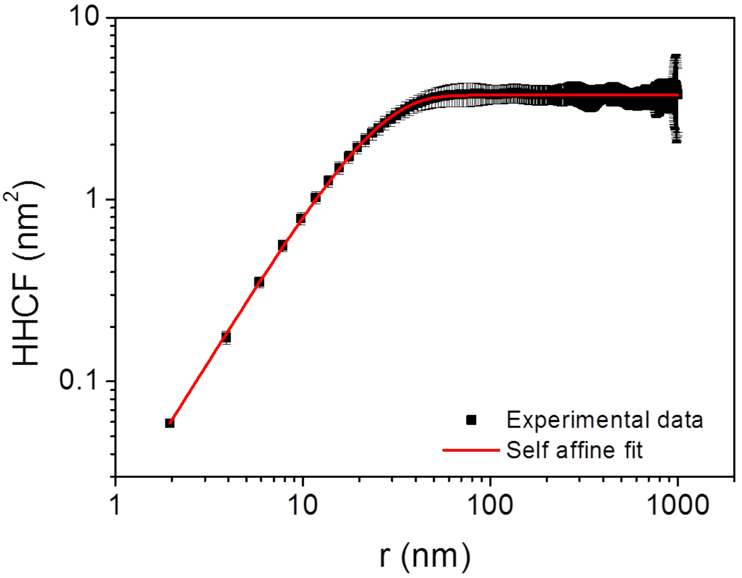

Figure 3.6: HHCF experimental data (black dots) and fitted curve (red line) for sample C 3h annealed of nc-SiO$_\mathrm{x}$N$_\mathrm{y}$. The plot is in logarithmic scales.

R_{HHCF}, ξ and α mean values with standard deviations are collected in Table 3.6 for samples C 0h, 3h and 6h annealed.

Table 3.6: Mean values with of roughness parameter R_{HHCF}, lateral correlation length ξ and roughness exponent α for all nc-SiO$_\mathrm{x}$N$_\mathrm{y}$ samples C.

Sample	**R$_{\mathrm{HHCF}}$ (nm)**	**ξ (nm)**	**α**
0h	1.204 ± 0.001	18.5 ± 0.2	0.866 ± 0.006
3h	1.369 ± 0.001	23.8 ± 0.2	0.829 ± 0.003
6h	1.476 ± 0.002	26.6 ± 0.4	0.903 ± 0.009

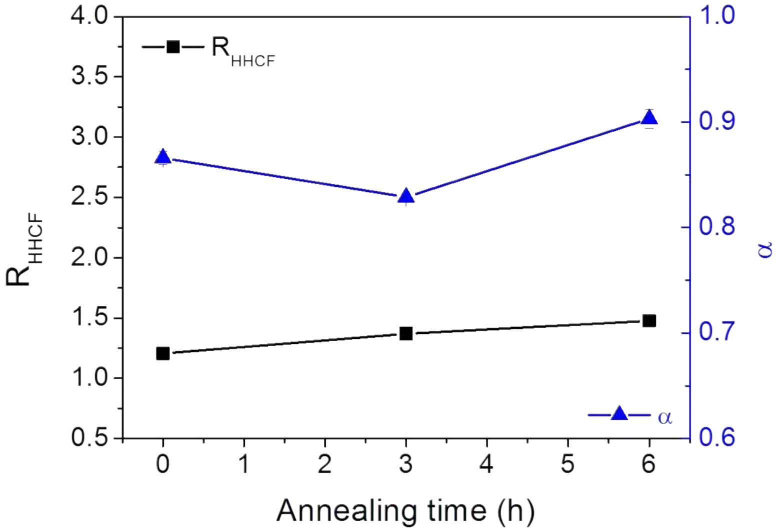

Figure 3.7: R_{HHCF} (black squares) and α (blue triangles) are plotted as functions of the annealing time for samples C. Lines are introduced as guide for the eye.

It is possible to deduce from these values that the roughness parameter R_{HHCF} raises with the increasing of the annealing time. This fact indicates that thermal treatment affects the grain heights due to a rearrangement of the atoms on the surface. Even the lateral correlation length ξ becomes larger with the extension of the annealing process duration. Since this parameter is related to how the grain structures repeat themselves at a certain distance, its variation can be an indicator of a different arrangement of the surface grains. At last, the values of the roughness exponent α remain approximately constant, with a little raise with higher annealing times. All these parameters, R_{HHCF}, ξ and α are plotted as function of the annealing time in Figure 3.7.

The plot on top of Figure 3.8 shows ξ and EDD trends as a function of the annealing time. Both parameters increase with longer annealing times, but ξ grows more rapidly than the dimension of grains. This characteristic reveals the presence of a clustering process of the structures. In plot at the bottom of Figure 3.8 the difference between ξ and EDD as a function of the annealing time is reported. The increasing trend of this quantity with higher annealing times proves a greater clustering process of the grains after the annealing. In conclusion, the thermal treatment causes changes in the surface properties of nc-SiO$_x$N$_y$. Higher annealing times raise the surface

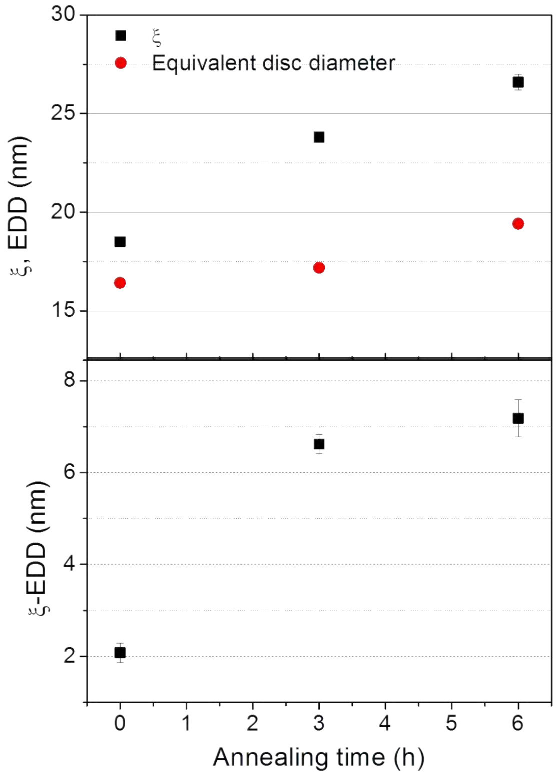

Figure 3.8: Top: ξ and EDD as a function of the annealing time of samples C. Bottom: $\xi-$EDD as a function of the annealing time of the same samples.

roughness and produce variations in the arrangement of the grains, due to a different clustering process.

To achieve some information on the compositional properties of the surface, tapping mode AFM maps in repulsive range were acquired with NT-MDT Solver P47H Pro AFM for all samples. The scan areas were 1×1 μm^2 large with a resolution of 512×512 px^2. As an example, both morphology and phase maps for sample C 3h annealed are reported in Figures 3.9(a) and 3.9(b), respectively. Whereas, the maps of sample E 3h annealed are shown in Figures 3.9(c) and 3.9(d). Phase maps exhibit zones with different phase lags. This difference is noticed between grains and grain boundaries. Phase lag during phase acquisition can be related to the differences in the composition of the surface, since they are related by the expression in Equation 2.28 [60]. As any difference in height can lead to a variation of the phase, a possible correlation between topography and phase has to be excluded. For this reason, height profiles were extracted for sample C 3h annealed and sam-

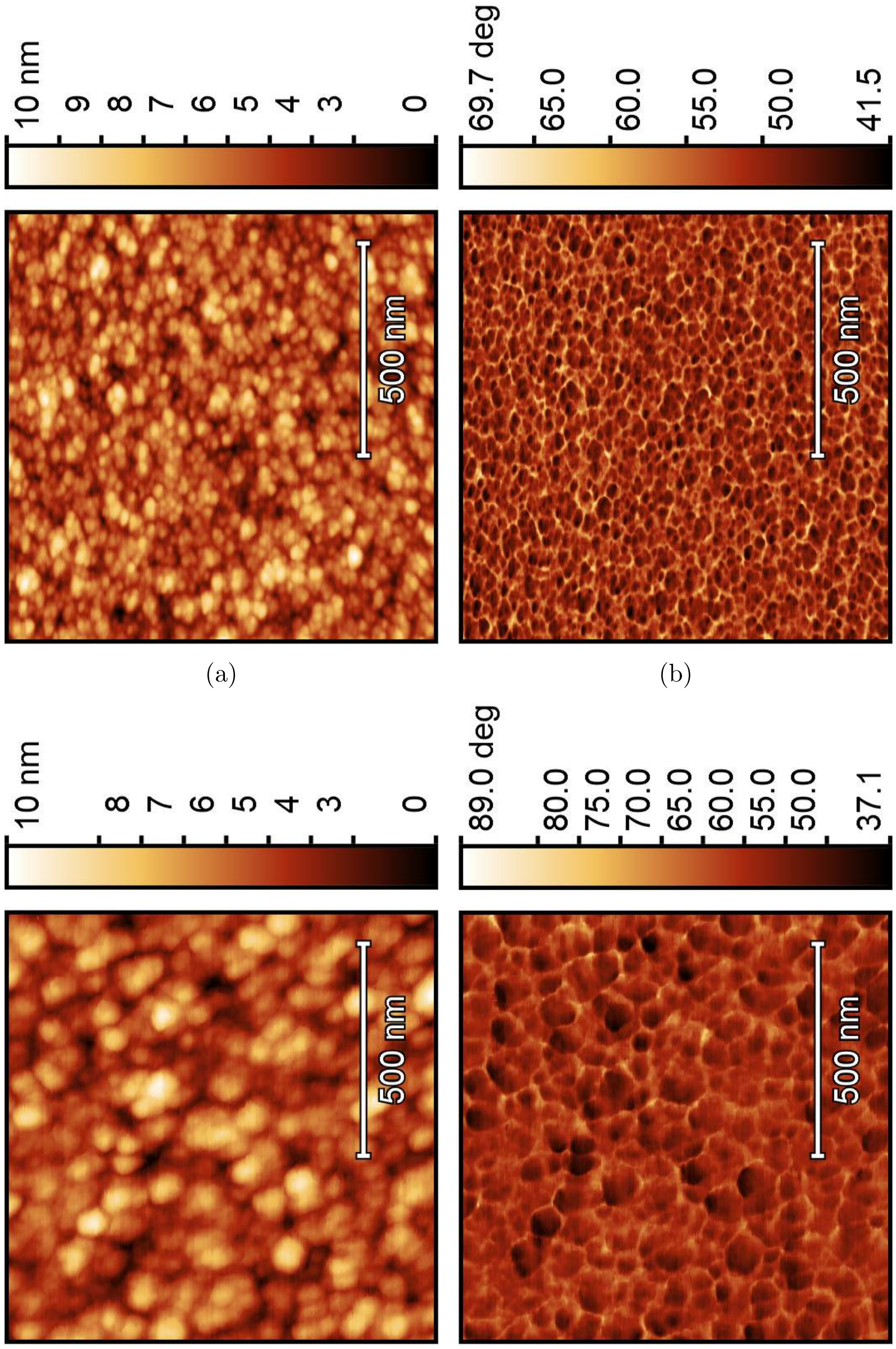

(a) (b)

(c) (d)

Figure 3.9: a) Morphology and b) phase maps of sample C 3h annealed using repulsive tapping mode AFM. c) Morphology and d) phase maps of sample E 3h annealed in repulsive mode AFM.

ple E 3h annealed. This profiles are shown in Figures 3.10(a) and 3.10(b), respectively. The comparison between height and phase contrast in Figures 3.10(a) and 3.10(b) shows that the phase variations cannot be ascribed only to morphology variations, since the peaks in the height profile do not always correspond to down spikes in the phase profile. Therefore, according to what found in [60, 79], it is possible to conclude that phase variation could be related to local compositional variation of the sample and that different compositions are present on the surface of nc-SiO_xN_y samples.

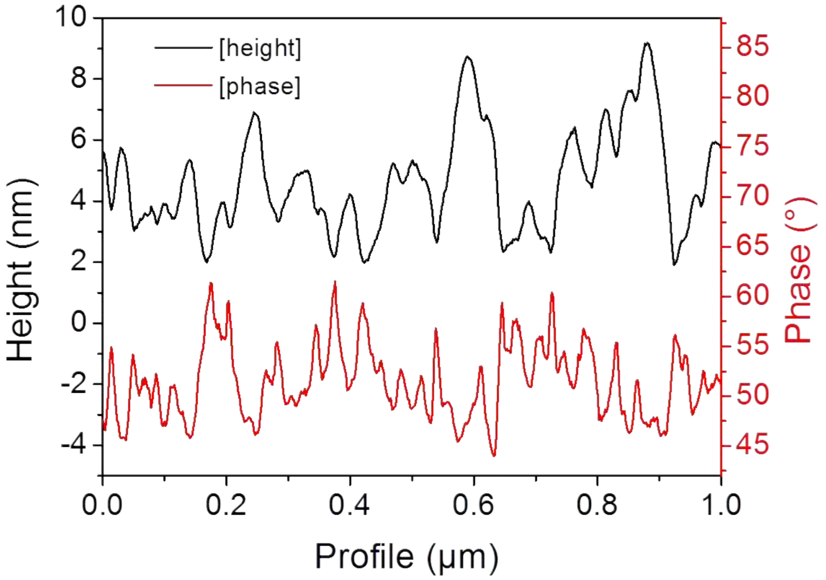

(a)

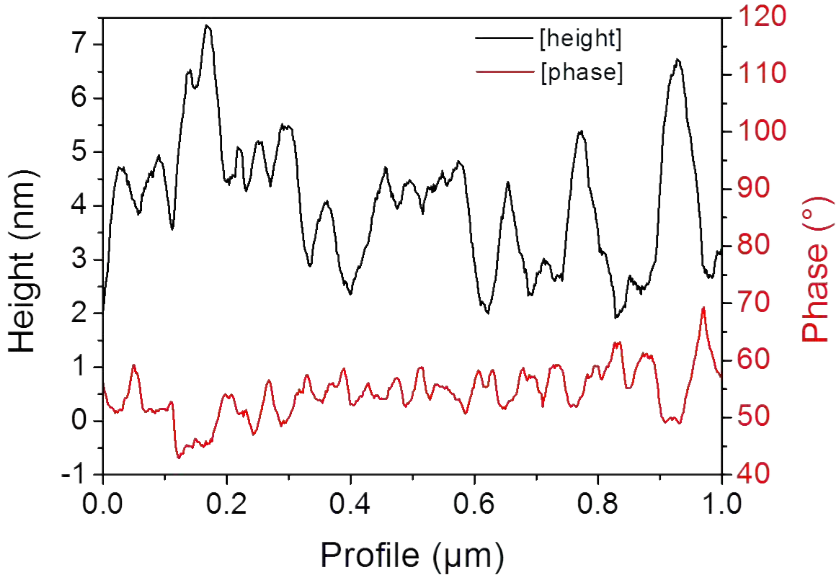

(b)

Figure 3.10: Height and phase profiles of a) sample C 3h annealed and b) sample E 3h annealed of nc-SiO$_x$N$_y$.

3.2.2 Electrical Characterization

c-AFM maps in contact mode were acquired, in order to estimate any variation of the electrical properties at the nano-scale of the nc-$\mathrm{SiO_xN_y}$ thin layers with different content of oxygen or different annealing time. Samples C were deposited by PECVD with a N_2O dilution in silane of 9.09%, while sample E was deposited with 47.4% dilution of the same precursor gas (Table 2.1 in Section 2.1.1). For the scanning, three samples were investigated: sample C both 3h annealed and as-deposited, and sample E with a 3h annealing. Two maps 1×1 μm^2 for each sample with a positive and a negative voltage were acquired through Park NX10 AFM. The resolution of these maps was 512×512 px^2. The voltages applied were different for each sample, since they were selected to create a measurable current.

In Figures 3.11(a) – 3.11(d) both topography and current maps of sample C 3h annealed are shown with different applied voltages of 0.1 and -0.1 V, respectively. The c-AFM measurements reveal the presence of more conductive grains with respect to others less conductive, in a non conductive surrounding. The most conductive regions reach currents of almost 10 nA with both positive and negative voltages. It must be noted that this behavior occurs in both positive and negative applied bias with similar current variations for the same applied bias.

Figures 3.12(a) to 3.12(d) show topography and current maps of the sample C as-deposited with an applied bias voltages of 1.5 and -1.5 V, respectively. With respect to sample C 3h annealed, higher voltages had to be applied in order to have enough current flowing between the tip and the sample. Secondly, the conductive grain distribution is more uniform and the conduction of grains is similar in almost all grains. The currents measured are less intense with respect to the annealed sample, even if higher voltages were applied. With a negative applied bias, currents drop drastically about an order of magnitude.

Figures 3.13(a) to 3.13(d) illustrate the topography and current images of sample E 3h annealed with applied bias voltages of 0.4 and -0.4 V (sample deposited with a higher $\mathrm{R_{N_2O}}$). Even in this case, the sample is less conductive with respect to sample C 3h annealed and the distribution of the grain conductivity seems more uniform. Moreover, negative applied voltages generate lower currents at equal voltage values.

In Table 3.7 maximum values of local conductance of all samples investigated with c-AFM technique are listed with both positive and negative applied voltages. The highest conductance is reached by the sample C 3h annealed. A steep decrease of 2-4 orders of magnitude is observed for as-deposited samples. In addition, a decrease of two to three orders of magnitude appears when the oxygen content in the sample is increased.

The electrical properties were investigated in different points of the surface by IV characteristics measured with a bias voltage varied in different ranges for all three samples. The plots in Figures 3.14(a), 3.14(b) and 3.14(c) show different electrical behaviors of sample C 3h annealed, sample C as-deposited and sample E 3h annealed, respectively. After thermal treatment sample C shows the most conductive behavior in the several points investigated and has the greatest variation of electrical behavior in different points. This confirms the presence of different conduction zones in its current maps. This variability is not as wide for the other two samples, which exhibit a lower local variation of IV characteristics. Current-voltage characteristics for these samples show the typical exponential trend of the sandwich structure metal/semiconductor/metal, that is tip/nc-SiO$_x$N$_y$/contact to the ground [78, 80]. This ensemble is commonly called a pair of back-to-back Schottky barriers [80].

Table 3.7: Maximum values of local conductance G (S) as evaluated by c-AFM of nc-SiO$_x$N$_y$ samples (C 3h, C as-deposited and E 3h) with both positive and negative applied voltages.

	C 3h	**C 0h**	**E 3h**
Positive	$0.9 \cdot 10^{-7}$	$7 \cdot 10^{-10}$	$2 \cdot 10^{-9}$
Negative	$1 \cdot 10^{-7}$	$4 \cdot 10^{-11}$	$6 \cdot 10^{-10}$

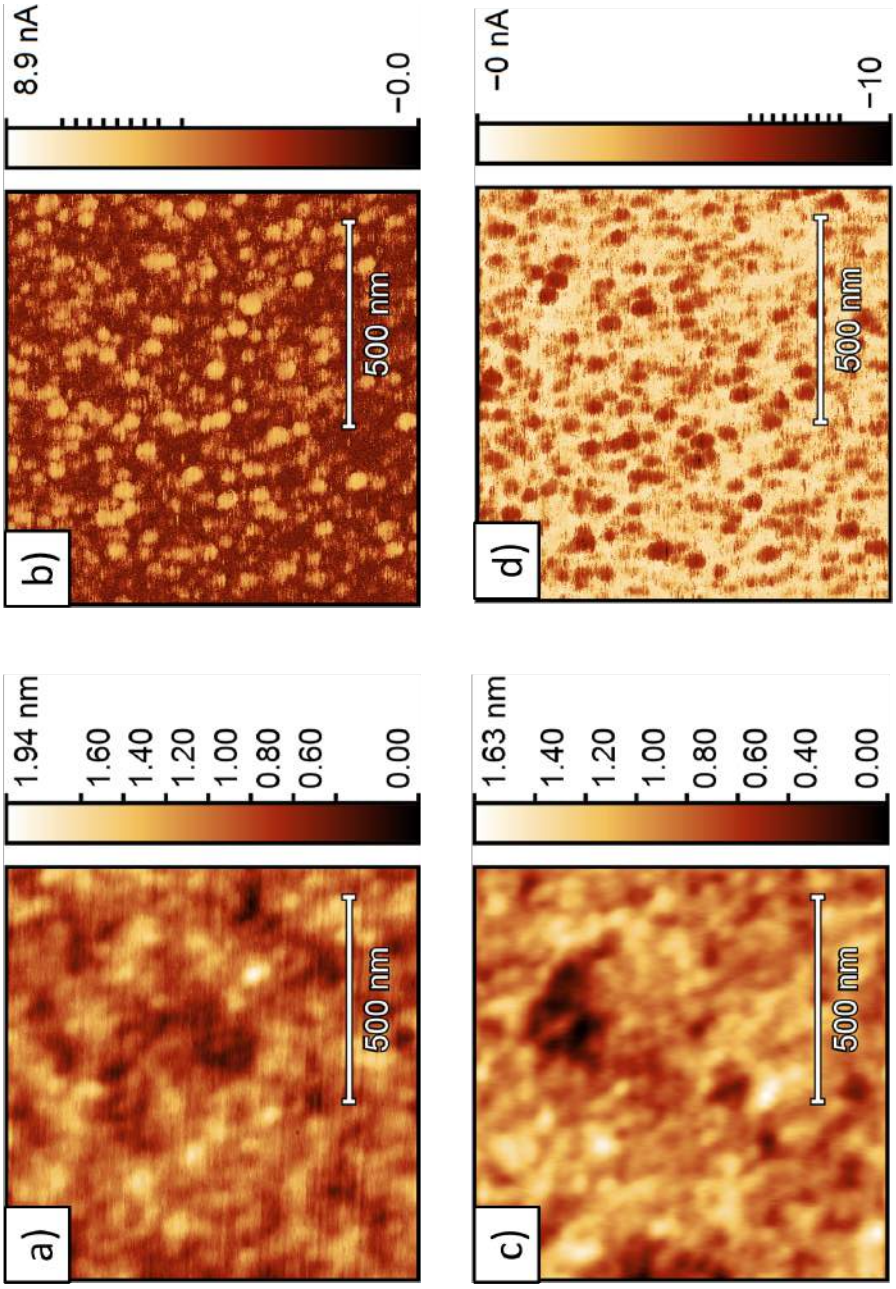

Figure 3.11: a) Height and b) current maps of sample C 3h annealed with an applied bias of 0.1 V. c) Height and d) current maps of the same sample in which a voltage of -0.1 V is applied. The range of current values is nonlinear.

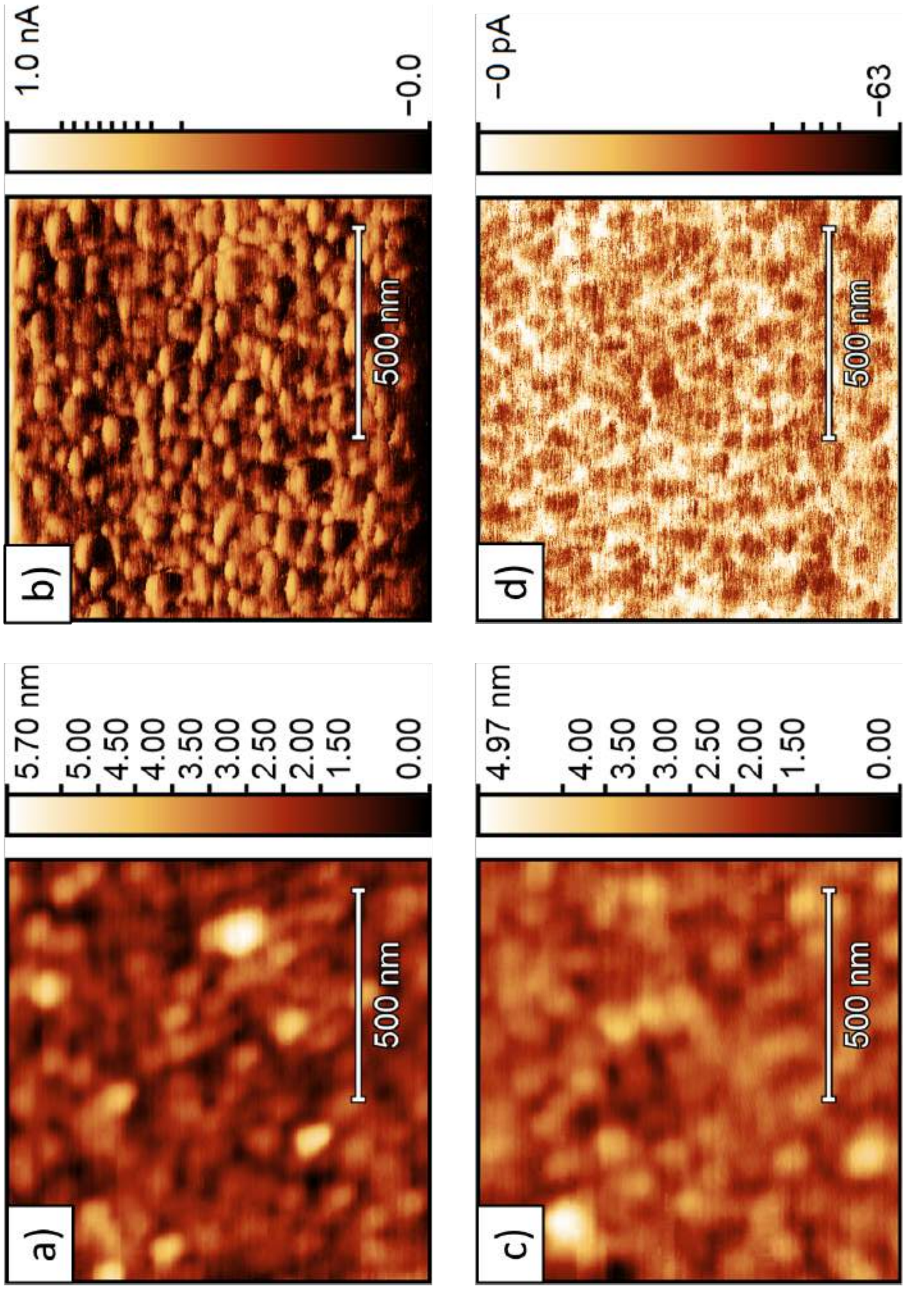

Figure 3.12: a) Height and b) current maps of sample C as-deposited with an applied bias of 1.5 V. c) Height and d) current maps of sample C 0h in which a voltage of -1.5 V is applied. The range of current values is nonlinear.

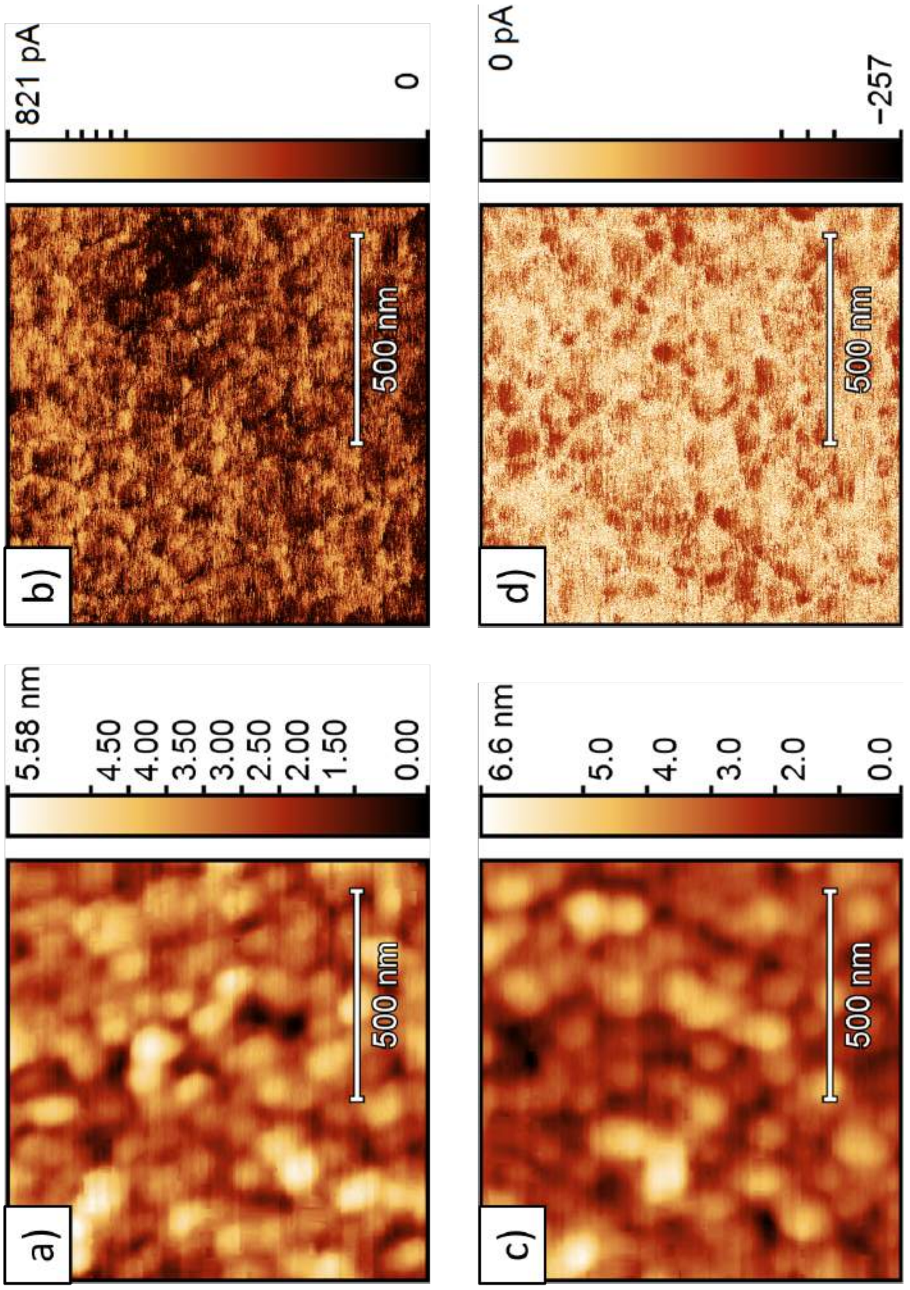

Figure 3.13: a) Height and b) current maps of sample E 3h annealed with an applied bias of 0.4 V. c) Height and d) current maps of the same sample in which a voltage of -0.4 V is applied. The range of current values is nonlinear.

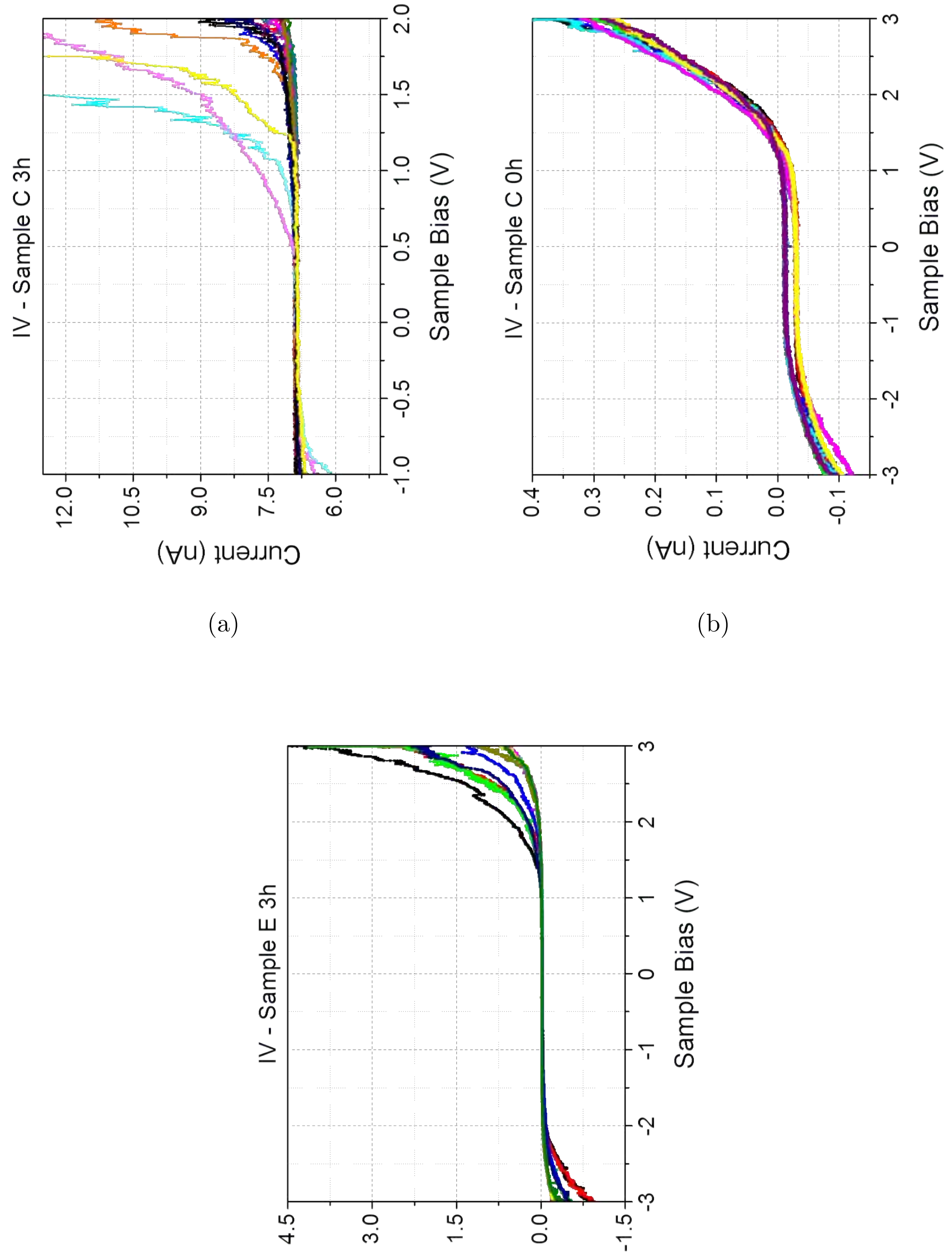

(a) (b)

(c)

Figure 3.14: IV characteristic curves in different points of a) sample C 3h annealed, b) sample C as-deposited and c) sample E with a 3h annealing, respectively.

3.3 *a*-$\mathrm{SiO_xN_y}$

In order to achieve a complete analysis, *a*-$\mathrm{SiO_xN_y}$ thin layers were investigated using different AFM modes of operation. The samples under analysis, 1 to 4, differ only in the electrode distance during the deposition, from 22 to 55 mm, respectively (Table 2.2 in Section 2.1.2). Several maps in attractive and repulsive tapping mode (Section 2.2.4) were acquired for all the samples in order to achieve information about morphology (roughness, lateral correlation length, mean grain diameter) and composition, respectively. Then, investigation on conductivity of sample 3 was obtained by c-AFM measurements and IV characteristics in different points of the surface were acquired (Section 2.2.5).

3.3.1 Morphological and Structural Analysis

To investigate the morphology of *a*-$\mathrm{SiO_xN_y}$ thin films, ten maps for each sample (1 to 4) 500×500 nm^2 were acquired with a resolution of 512×512 px^2. Initially, 1×1 μm^2 maps with a resolution of 1024×1024 px^2 were acquired with Park NX10 AFM. Each map has been cut in four parts. Through this procedure, 500×500 nm^2 maps with half resolution were captured. The best ten maps were chosen for the statistical analysis, while maps less resolved or with tip-sample instabilities were discarded. A map for each sample is shown in Figures 3.15(a), 3.15(b), 3.15(c) and 3.15(d). All maps were processed by segmentation, with parameters listed in Table 3.8.

Table 3.8: List of all segmentation parameters set for *a*-$\mathrm{SiO_xN_y}$ samples. The parameters are defined as in Table 2.4.

Parameter	**Value**
GS	4.00 px
AG	65%
AC	0%
BL	100%
PL	0%
PFM	12.35%

After this process, a threshold of 2 px^2 and a filter for the minimum value of +1.20 nm from the bottom were applied. The resulting inverted mask superimposed to the map is shown in Figure 3.16. The pink areas are the portions of the maps cut from the threshold, while the pink lines segment different grains. From each mask, both number of grains (NOG) and equivalent disc diameter (EDD) were extracted. EDD is linked to MGS defined in Section 2.2.10 through the following expression:

$$[\mathrm{EDD}] = \frac{2\,[\mathrm{MGS}]}{\sqrt{\pi}} \tag{3.1}$$

A mean value and its error of EDD and NOG were evaluated for each a-SiO$_x$N$_y$ sample. All values are reported in Table 3.9.

Table 3.9: Mean value and errors of the equivalent disc radius and the number of grains for all a-SiO$_x$N$_y$ samples.

Sample	**EDD (nm)**	**NOG**
1	7.8 ± 0.2	3400 ± 200
2	8.0 ± 0.1	3280 ± 90
3	7.8 ± 0.2	3500 ± 200
4	7.9 ± 0.2	3320 ± 60

From these values, it is possible to conclude that the equivalent disc diameter (EDD) and the number of grains (NOG) for different samples of a-SiO$_x$N$_y$ thin layers does not vary within the experimental error. Therefore, the electrode distance in the deposition does not affect the dimension of the grains and their density on the surface.

Gwyddion roughness parameters R^*, R_q and HHCF were extracted from each map. Roughness parameters are the mean values calculated on columns/ rows of statistical parameters R_a and RMS, expressed in Equations 2.29 and 2.30. HHCF was fitted with the exponential expression in Equation 2.37. From this fit it was possible to evaluate the roughness parameter R_{HHCF}, the lateral correlation lenght ξ and the roughness exponent α for each map. Therefore, the mean values with experimental errors of all these parameters can be calculated for each a-SiO$_x$N$_y$ sample. An example of experimental data (black dots) and fit (red line) of HHCF for sample 2 is illustrated in Figure 3.17.

These statistical parameters are listed in Table 3.10 for all a-SiO$_x$N$_y$ samples.

It can be deduced that all three roughness parameters R_q, R^* and R_{HHCF} are compatible within the errors for each sample. First of all, this means that one can indifferently employ one of these parameters alone in order to evaluate the roughness of a surface. Secondly, the estimate of roughness is consistent, since these parameters are calculated with different mathematical paths. As can better be seen in Figure 3.18(a), roughness of all a-SiO$_x$N$_y$ thin layers remains almost constant for different samples. Therefore, the

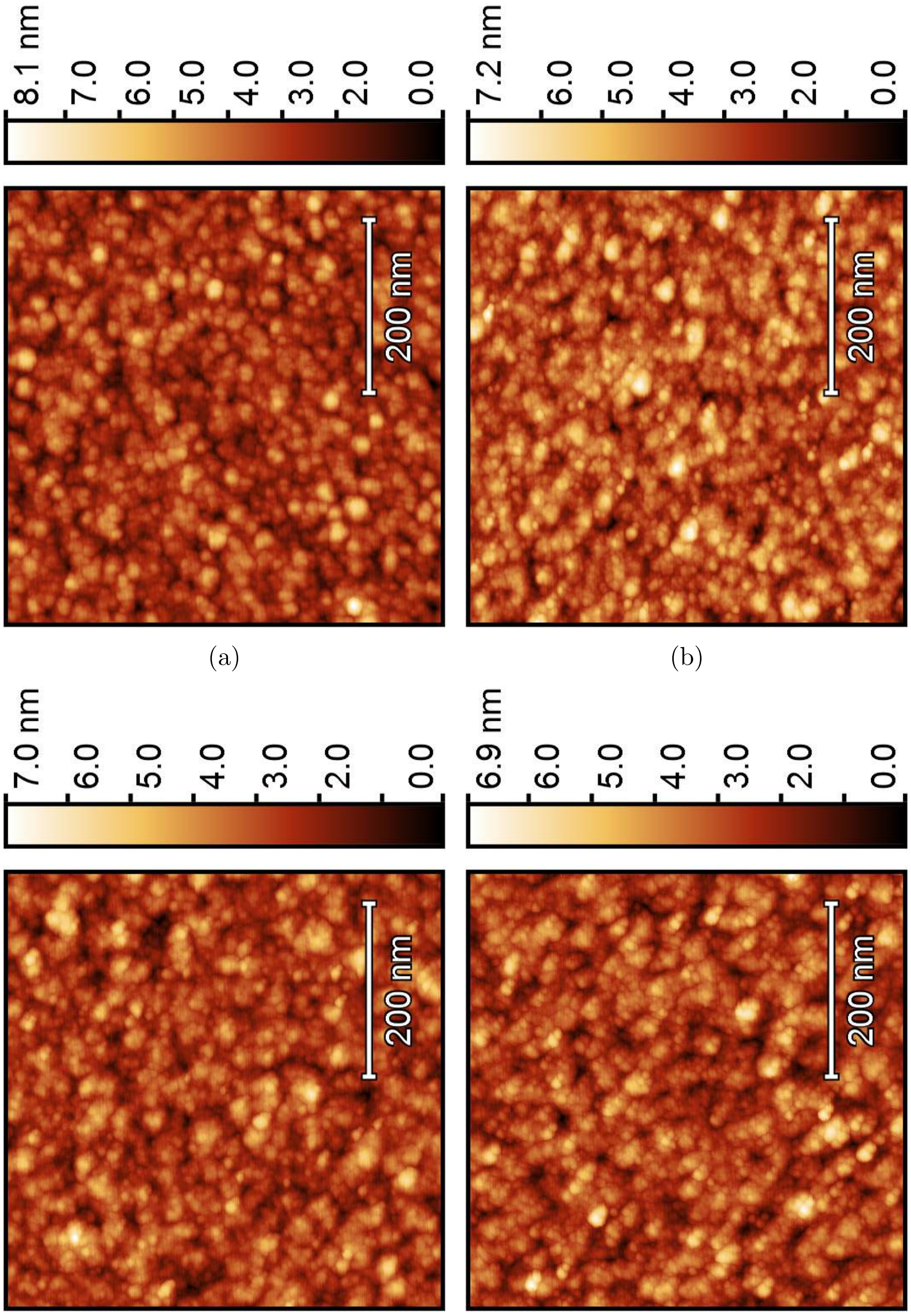

(a)

(b)

(c)

(d)

Figure 3.15: AFM maps acquired in attractive mode of a) sample 1, b) sample 2, c) sample 3 and d) sample 4, respectively. The scan area is $500 \times 500\text{nm}^2$ with a resolution of 512×512 px^2. The samples are described in Table 2.2 in Section 2.1.2.

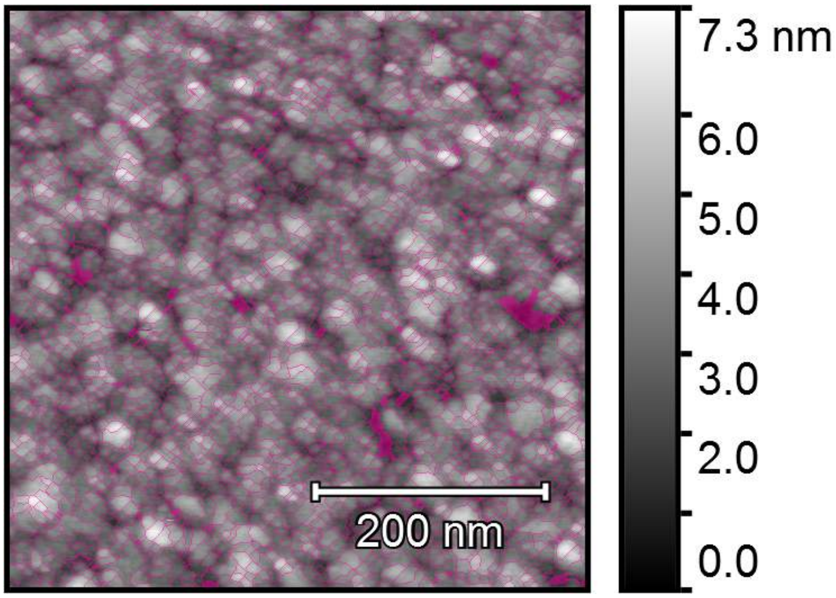

Figure 3.16: Inverted mask applied on a map of Sample 3 of a-SiO$_x$N$_y$ with parameters of Table 3.8.

Table 3.10: Mean values with experimental error of roughness parameters (R_q, R^* and R_{HHCF}), lateral correlation length ξ and roughness exponent α for all a-SiO$_x$N$_y$ samples.

Sample	**R$_q$ (nm)**	**R* (nm)**	**R$_{HHCF}$ (nm)**	**ξ (nm)**	**α**
1	0.83 ± 0.02	0.8 ± 0.1	0.8487 ± 0.0007	11.1 ± 0.1	0.863 ± 0.008
2	0.87 ± 0.04	0.9 ± 0.2	0.8849 ± 0.0004	12.13 ± 0.06	0.844 ± 0.003
3	0.83 ± 0.05	0.8 ± 0.2	0.8497 ± 0.0009	12.5 ± 0.1	0.834 ± 0.007
4	0.85 ± 0.03	0.8 ± 0.1	0.8584 ± 0.0007	12.1 ± 0.1	0.831 ± 0.007

distribution of the recorded heights is essentially not affected by the electrode distance during the deposition. This conclusion cannot be done for the lateral correlation length ξ and the roughness exponent α, as illustrated in Figure 3.18(b). Indeed, ξ has an increase (up to an electrode distance of 40 mm) and then a decrease (black squares in Figure 3.18(b)); while α decreases as the electrode distance increases (red dots in Figure 3.18(b)). Since ξ is correlated to the mean grains arrangement, it can be derived that different distances of electrodes during deposition do not affect the mean grain size, but give rise to a different clustering of the grains on the surface. The little decrease of α with the increase of the deposition electrode distance implies that surfaces that are locally rougher are grown with larger electrode

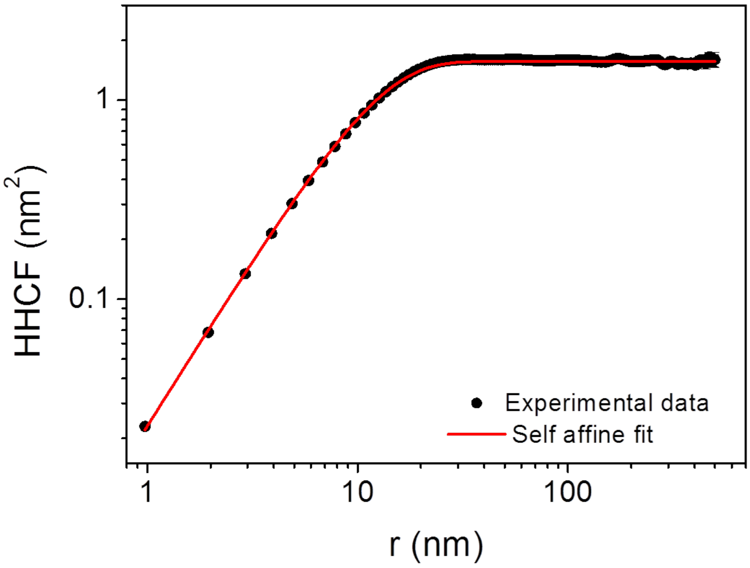

Figure 3.17: HHCF experimental data (black dots) and fitted curve (red line) for sample 2 of a-SiO$_x$N$_y$. The plot is in semi-logarithmic scale.

distances.

It can be concluded that the variation of electrode distance during the deposition of a-SiO$_x$N$_y$ thin layers does not vary the mean grain size and the roughness of the surface, while it affects the arrangement and clustering of grains.

In order to clarify the structural properties of the grains at the surface, tapping mode AFM maps in repulsive range were acquired with NT-MDT Solver P47H Pro AFM and then investigated for all samples. Areas of 1 × 1 μm^2 were scanned with a resolution of 512 × 512 px^2. As an example, morphology and phase maps for sample 1 are reported in Figures 3.19(a) and 3.19(b), respectively. Phase lag in phase acquisition is correlated to the different atomic composition of the surface, through the expression in Equation 2.28 [60]. It can be observed that the grains generate a different phase lag with respect to the grain boundaries. In order to exclude a possible correlation between the topography and the phase maps, height and phase profiles were extracted. A profile of height and phase is shown in Figure 3.19(c). A correlation cannot completely be excluded, since phase peaks positions seem to correspond to those of heights down spikes. Anyway, different heights peaks in topography correspond to down spikes of the same depths. It is possible to conclude that, even if a correlation between topog-

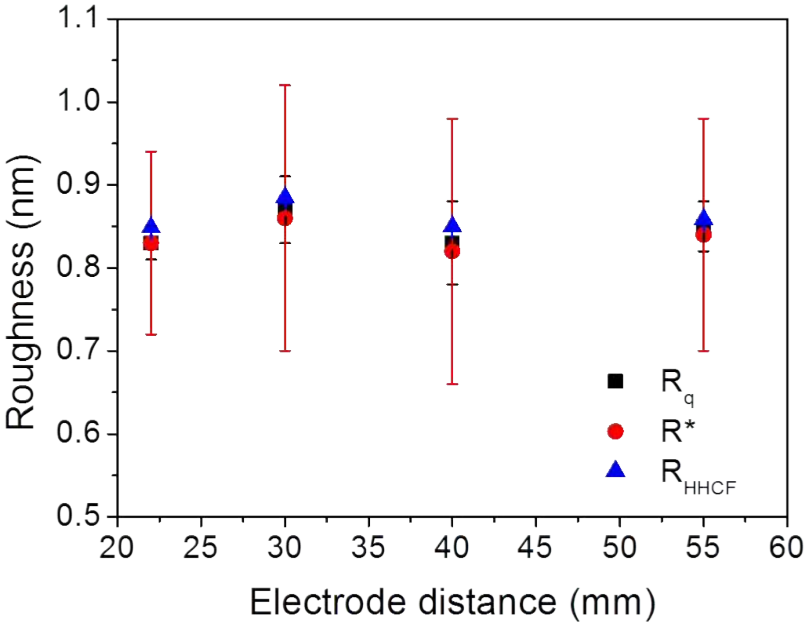

(a)

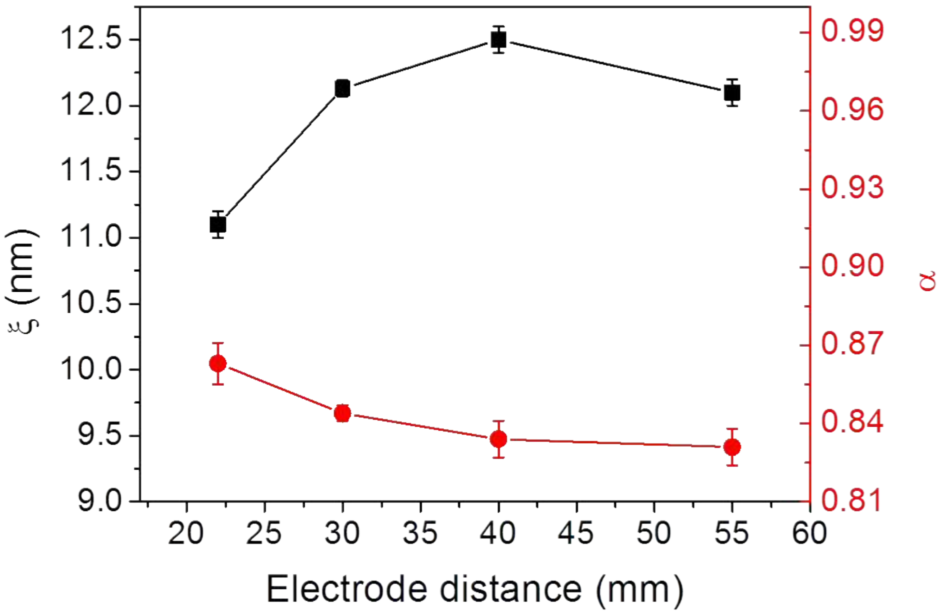

(b)

Figure 3.18: Plots of a) mean values of roughness parameters R_q (black squares), R^* (red circles) and R_{HHCF} (blue triangles), b) lateral correlation length ξ (black squares) and roughness exponent α (red dots) as functions of the electrode distance during deposition. Lines are used as guides for the eye.

raphy and phase maps cannot be completely ruled out, phase maps contain information on the surface composition.

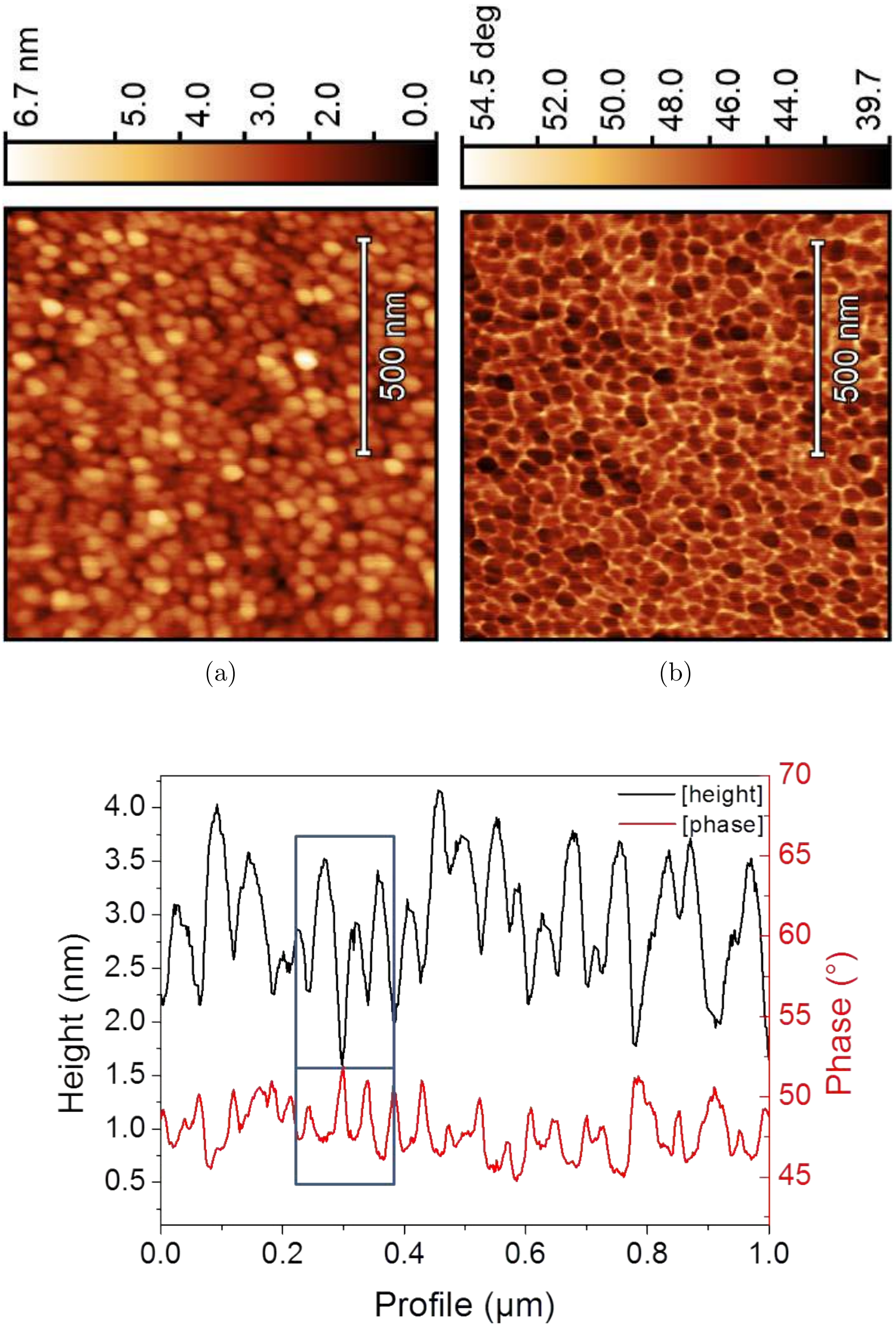

(a) (b)

(c)

Figure 3.19: a) Morphology and b) phase maps of sample 1 using repulsive tapping mode AFM. c)Height and phase profiles of sample 3 of a-SiO$_x$N$_y$.

3.3.2 Electrical Characterization

To evaluate the electrical properties at the nano-scale of the a-SiO$_x$N$_y$ thin layers, c-AFM maps in contact mode were acquired. For the scanning, sample 3 was chosen, as it demonstrated the best passivation quality among all the samples (Figure 2.7(b) in Section 2.1.2) [46]. Different maps $1 \times 1\ \mu m^2$ with several voltages were acquired by Park NX10 AFM with a resolution of 512×512 px^2. For this sample, two different bias voltages, one positive and one negative were applied to achieve current maps. The voltages employed were high enough to generate a measurable current.

In Figures 3.21(a) and 3.21(b) both topography and current maps of sample 3 are shown with an applied voltage of +6 V. On the other hand, Figures 3.21(c) and 3.21(d) are topography and current maps of the same sample with an applied bias of -3 V. In the first current map, there are more conductive grains and less conductive ones, within a non conductive matrix. The conductance varies from 0 to $2.5 \cdot 10^{-10}$ S. The sample appears to be more conductive when a negative bias is applied. In fact, in this case (Figure 3.21(d)) the conductance ranges between $(0 - 1.4) \cdot 10^{-9}$ S. Even with negative bias voltages, more conductive grains appear together with less conductive ones in a non conductive matrix.

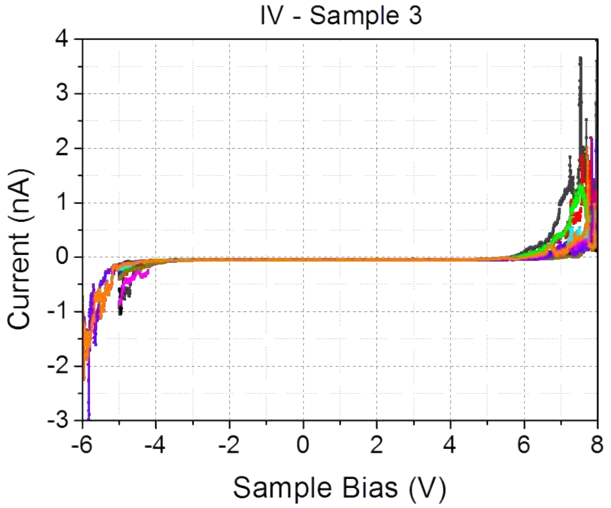

Figure 3.20: IV characteristic curves in different points of sample 3.

In order to analyze the electrical behavior in different points of the surface, IV characteristic curves were measured with a bias voltage varied in the range of (-6 – 8) V. The plots in Figure 3.20 exhibit different electrical behaviors in different points of the surface, confirming the different conduction zones that are present in the current maps.

With respect to nano-crystalline samples, some correspondences and differences can be pointed out. A large variability of the local conductance is shown in Figures 3.21(b) and 3.21(d), with the presence of more conductive grains with respect to others less conductive. As a proof, IV characteristics acquired in various points of the map exhibit very different trends (Figure 3.20). This behavior was also shown in sample C 3h annealed of nc-SiO$_x$N$_y$. With regard to the maximum conductance values and the asymmetrical behavior of the current with positive and negative bias, *a*-SiO$_x$N$_y$ appears to be similar to sample C 0h and E 3h of nc-SiO$_x$N$_y$, which show lower conductance values (Table 3.7).

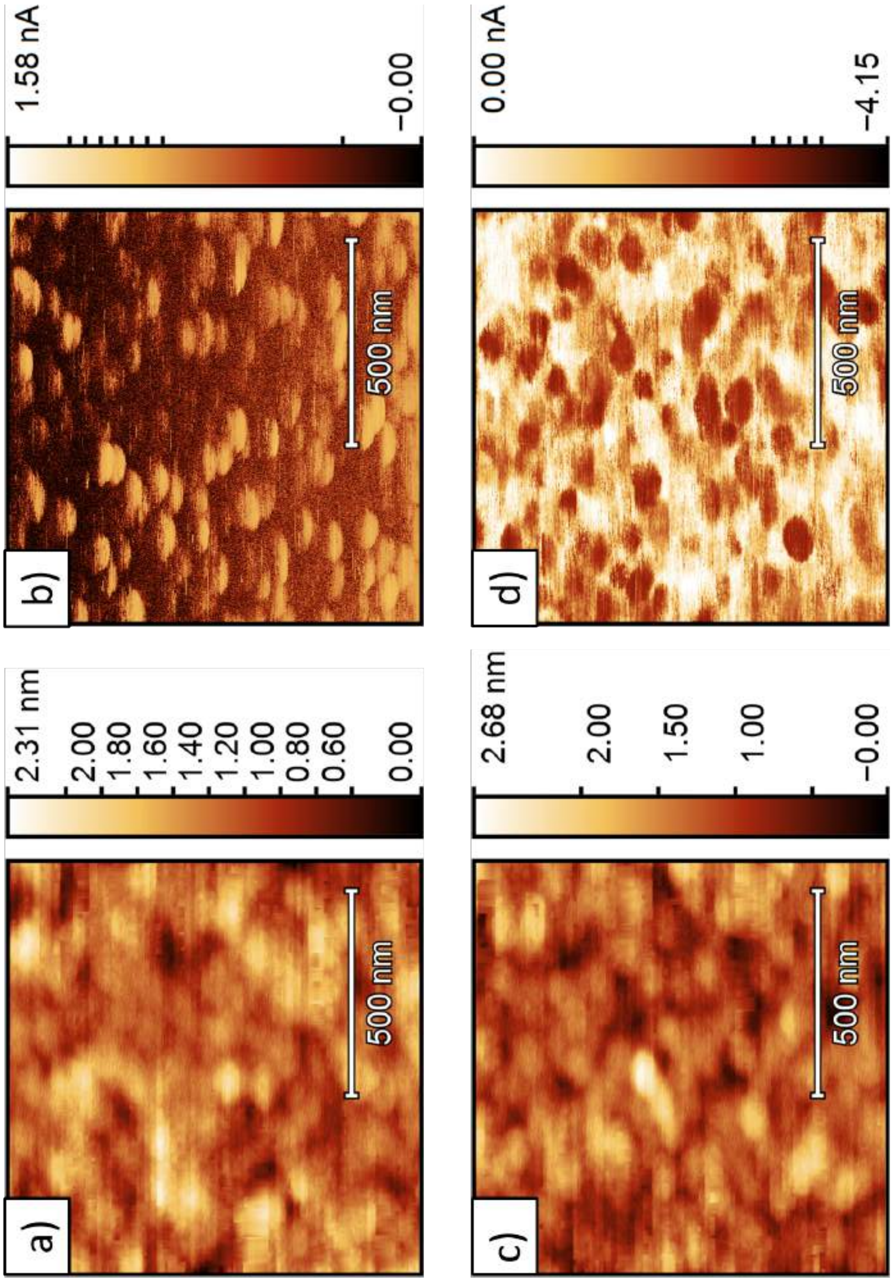

Figure 3.21: a) Height and b) current maps of sample 3 with an applied bias of 6V. c) Height and d) current maps of sample 3 in which a voltage of -3 V is applied. The scale of current maps is nonlinear.

3.4 Discussion

Morphological and electrical properties at the nano-scale are investigated in both nc- and *a*-$\mathrm{SiO_xN_y}$ thin layers by several AFM techniques. First of all, a thorough study of the new segmentation tool of Gwyddion software was obtained. This method is reproducible in several maps of the same sample, since the trend of mean grain size and number of grains as function of the variation of a single parameter is the same. The reproducibility of the parameters trends can be extended to different samples of similar structures. Some parameters are more influential than others on the statistical properties of the surface. The most meaningful variations for little deviations of the parameters from the initial value are shown for the Gaussian Smoothing, Add Gradient and Prefill Level parameters. The error coming from the choice of the parameters can be estimated to be below 4%. It follows that segmentation is a stable and consistent method for the statistical analysis of the grains for this kind of structures.

Differences in morphology and electrical properties were analyzed in nc-$\mathrm{SiO_xN_y}$ samples, when oxygen content and annealing time are varied. The thermal treatment deeply affects the properties of these thin films. Previous studies showed that the annealing process gives rise to an oxygen relocation within the layers, leading to a non-homogenous oxygen distribution [31]. Moreover, thermal annealing promotes a recrystallization of the layers of hydrogenated nanocrystalline silicon [81]. Nanocrystals formation due to annealing also contributes to the variations observed in the structure and electrical properties of the layers. In fact, the grain-like structure surface varies with the introduction of a thermal treatment. First of all the dimension of the grains raises with longer annealing times, with equivalent disc radius ranging from 16.42 to 19.34 nm for sample C. The lateral correlation length ξ also increases upon annealing, ranging between 18.5 to 26.6 nm. Since ξ is greater than the dimension of the grains, a clustering of the grains is present. Moreover, the faster increasing of ξ with higher annealing times with respect to the grain dimension depicts a bigger clustering process after the annealing. Therefore, annealing generates a different clustering of the grains.

The thermal treatment affects the electrical properties as well. Indeed, the sample annealed produces higher currents with lower bias voltages applied, with a maximum value of local conductance of $1 \cdot 10^{-7}$ S for sample C 3h annealed with a bias of -0.1 V. Electrical properties of nc-$\mathrm{SiO_xN_y}$ thin layers change drastically with different concentrations of $\mathrm{N_2O}$ during the deposition. Maintaining the same annealing time, samples with higher $R_{\mathrm{N_2O}}$ become conductive only with higher applied biases and the local conductance maximum drops to $6 \cdot 10^{-10}$ S with a bias of -0.4 V. Both annealing and different R_{N_2O} affect the current distribution of the grains, which is more uniform in both as-deposited and high R_{N_2O} samples. This could be related to a higher disorder promoted by an increase of the O content within the layers.

a-SiO_xN_y thin films properties were investigated, varying the electrode distance during the deposition. Both roughness and the dimension of grains do not change with different electrode distances, with mean grain size ranging between 7.8 and 8 nm. On the other hand, the lateral correlation length first increases and then slightly decreases with higher electrode distances, ranging between $11.1 - 12.5$ nm. The roughness exponent decreases as the electrode distance increases, revealing less locally smooth surfaces. a-SiO_xN_y thin layers does not reveal good electrical properties, as expected. Indeed, the conductance ranges between $0 - 1.4 \cdot 10^{-9}$ S for sample 3 with a bias of -3 V.

Drastic differences both morphological and electrical in the two series of the samples can be observed. In fact, nc-SiO_xN_y has greater grain dimensions with respect to the amorphous ones, with an equivalent disc diameter which is more than twice the amorphous one. Even the grain arrangement changes; the lateral correlation length for nano-crystalline samples is higher with respect to the amorphous series, due to a higher clustering process. At last, a-SiO_xN_y thin layers show little surface conductive properties, while nano-crystalline ones, especially samples annealed with the lowest R_{N_2O} are good conductors. It can be concluded that the crystallinity fraction significantly affects electrical properties of thin layers, as nc-SiO_xN_y show conductance values that drastically drop with both a higher dilution of N_2O and in samples as-deposited. This drop is exhibited also by the amorphous sample 3. Moreover, the distribution of conductive grains becomes less uniform in the sample with the highest crystallinity fraction (sample C 3h annealed), with the presence of scattered more conductive grains within a less conductive surrounding. The narrow distribution of the local conductivity in samples C 0h and E 3h is confirmed by the little range of IV characteristics acquired in different points of the samples. Furthermore, sample C 3h annealed is the only sample that shows a symmetric behavior with both positive and negative voltages, reaching a maximum value of conductance of $1 \cdot 10^{-7}$ in both cases.

Conclusions

This thesis reports on morphological and electrical analyses on both intrinsic amorphous and p-doped nano-crystalline silicon oxy-nitride (a-$\mathrm{SiO_xN_y}$ and nc-$\mathrm{SiO_xN_y}$, respectively) by means of Atomic Force Microscopy (AFM) techniques.

The framework of the present thesis is the energetic challenge, in particular the need to improve renewable energies, with a special attention on photovoltaics (PV). In this context we have focused on the silicon heterojunction (SHJ) solar cells. These devices are made with several thin layers of different materials, with an absorber made of crystalline silicon (c-Si). In order to diminish the surface states, that act as recombination centers, passivation layers are introduced in the structure. In this way, a heteroemitter stack is composed of a doped film on the top (that corresponds to one side of the pn junction together with the absorber) and a passivation intrinsic layer at the bottom [6]. In the current technology, the heteroemitter stack is made of hydrogenated amorphous silicon (a-Si:H). With this composition, SHJ solar cells with intrinsic thin layer have already reached an efficiency of 25.6% in 2014 [8, 30].

Since PV aims to the achievement of higher efficiency values with a simultaneous reduction of costs in view of the industrial production, new materials with better properties have been studied as substitutes for the thin films in the heteroemitter stack. In this perspective, $\mathrm{SiO_xN_y}$ turned out to be a promising material as window layer or passivation layer in SHJ solar cells. The greater drawback of a-Si:H, the material that is currently employed, is its great parasitic light absorption, that causes a decrease in the cell efficiency [9]. This effect can be reduced with the employment of a wider band gap material, i.e. $\mathrm{SiO_xN_y}$. In fact, the optical band gap of a-$\mathrm{SiO_xN_y}$ layers can be widened up to 2.2 eV, thanks to the incorporation of both oxygen and nitrogen in the material [9]. The combination of intrinsic and doped a-$\mathrm{SiO_xN_y}$ thin films in the heteroemitter stack has already shown high values of open circuit voltage (733 mV) [9]. Moreover, the substitution of the doped amorphous layer with a nano-crystalline one can boost the solar cell efficiency, since this material creates a lower contact resistance with the transparent conductive oxide on the top of it [13, 31]. Notwithstanding the interesting properties of *a*- and nc-SiO_xN_y thin layers, a thorough study of the connection between the deposition conditions and properties of the materials, as well as a model of electric transport is still lacking. In this perspective, this thesis aims to investigate SiO_xN_y thin films in their morphological and electrical properties at the nano-scale.

Nc- and *a*-SiO_xN_y thin layers are deposited by Plasma Enhanced Chemical Vapor Deposition (PECVD) at the Department of Physics of the University of Konstanz (UKN). In nc-SiO_xN_y thin layers, the dilution of N_2O as a precursor gas during deposition has been varied; moreover, the samples have undergone different annealing times. On the other hand, all deposition parameters have been kept constant in *a*-SiO_xN_y samples, with the exception of the electrode distance during PECVD deposition.

A previous analysis of nc-SiO_xN_y thin layers has shown that the crystalline fraction increases with the addition of a thermal treatment, saturating after 3h of annealing [31]. On the other hand, crystallinity suffers of a decrease with higher N_2O dilutions. Higher dilutions lead to a linear increase of oxygen content, while nitrogen content remains constant. Therefore, the annealing process promotes nanocrystals formation with Si-rich and O-rich areas, while higher oxygen content due to higher N_2O dilutions leads to a greater disorder, with a drop in conductivity [31]. Samples of nc-SiO_xN_y with different oxygen contents, as-deposited or annealed, have been investigated in this thesis, in order to evaluate the effects of thermal treatment and different N_2O dilutions on nano-scale morphological and electrical properties.

A previous study on *a*-SiO_xN_y thin layers has shown that the sample deposited with an electrode distance of 40 mm exhibited the best passivation quality, reaching a minority carrier lifetime of 296 μs [46]. The effect of the electrode distance of morphological properties of these samples has been analyzed.

A statistical study of the morphology of the sample has been performed, acquiring AFM maps in non-contact mode in attractive range. A complete characterization of the surface of the different layers has been achieved, with the determination of the surface roughness, the roughness exponent and the lateral correlation length, as well as the equivalent disc diameter.

A previous check on the software for the morphological analysis, called segmentation, has been made. With this tool, it is possible to identify the grains on the map, through an initial setting of several parameters, achieving information about their mean diameter and number. The results of how the divergence of each parameter from the most suitable ensemble affects the grain properties have been investigated. After this analysis, segmentation turns out to be a reproducible method for different maps of the same sample and for different samples with similar structures. Moreover, it exhibits stability and consistency, since the error belonging to a wrong choice of parameters is below 4%.

Moreover, nano-scale electrical characterization of the samples has been achieved with conductive-AFM (c-AFM) acquisitions. C-AFM maps allow for obtaining a local conductivity map with high spatial resolution.

The main results achieved on nc- and a-SiO_xN_y thin layers are the following ones. The thermal treatment deeply affects the surface structure of nano-crystalline layers. Indeed, both the dimensions of grains and the lateral correlation length increase with higher annealing times. Since lateral correlation length values rise faster with respect to the equivalent disc diameter, the annealing process produces clustering of the grains.

The thermal treatment, as well as the different oxygen content affect the electrical properties of the sample. The annealed sample with the lower N_2O dilution shows the highest maximum local conductance. The sample showed conductive areas both with positive and negative applied bias. On the contrary, the as-deposited sample and the sample with higher O content and annealed at 3h showed a conductance with a negative bias that drops of several orders of magnitude. Moreover, current maps of the sample with a lower oxygen content annealed for 3h reveal the presence of conductive grains within a low conductivity surrounding area. This wide local conductivity distribution is confirmed by current-voltage characteristics, in which dissimilar trends on different points of the map are exhibited. However, as-deposited samples as well as layers with higher O content exhibit a more uniform conductivity distribution.

In a-SiO_xN_y thin layers, both roughness and equivalent disc diameter do not vary as the electrode distance increases. Whereas, the lateral correlation length first raises and then slightly decreases with greater values of the electrode distances. The roughness exponent decreases as function of the electrode distance, exhibiting less locally smooth surfaces as the distance increases. The amorphous samples are characterized by a low local conductivity, exhibiting an asymmetric behavior with positive and negative bias. Nevertheless, a wide distribution of local conductivity is shown, with inhomogeneities present in c-AFM maps likely due to O clustering. Further analyses are planned in order to evaluate the correlation between the distribution of the oxygen and the local conductance.

In conclusion, the thermal treatment and the oxygen incorporation in nc-SiO_xN_y thin films deeply affect both morphology and nano-scale electrical properties of the samples. The annealing process promotes clustering and enhances conductivity. As it is known that it promotes cristallinity [31], the appearance of conductive grains is likely related to crystalline regions. However, the increase of O content causes the increase of crystal disorder, which affects conductivity. Moreover, the electrode distance during the deposition of *a*-SiO_xN_y samples modifies grain clustering on the surface. These samples show low electrical conductivity, with the presence of more conductive grains at the surface.

The improved knowledge of the nano-scale morphological and electrical properties of SiO_xN_y layers achieved in this thesis adds new insight into the material properties, such as clustering and electrical transport. In addition, it gives information on the best deposition setup in order to obtain suitable materials for SHJ solar cells application. This step is fundamental since it paves the way for an industrial production of SHJ solar cells with nc- and *a*-SiO_xN_y thin layers as the heteroemitter stack.

Appendix

This section reports several artifacts that can occur during AFM maps acquisitions. In the first part from Figure 3.22(a) to 3.24(c) many artifacts due to the tip degradation are shown, from the most common triangles to strange features.

In addition, Figures from 3.25(a) to 3.25(c) show distortions due to the thermal drift or wrong scan speed are illustrated, from .

Figures 3.26(a) and 3.26(b) show the height acquisition and its correspondent phase map, in which a piece of foulness or dust has been captured from the tip and appears repeatedly on the image of the sample.

Last but not least, a masterpiece of instability of the acquisition probably due to a temporary software problem.

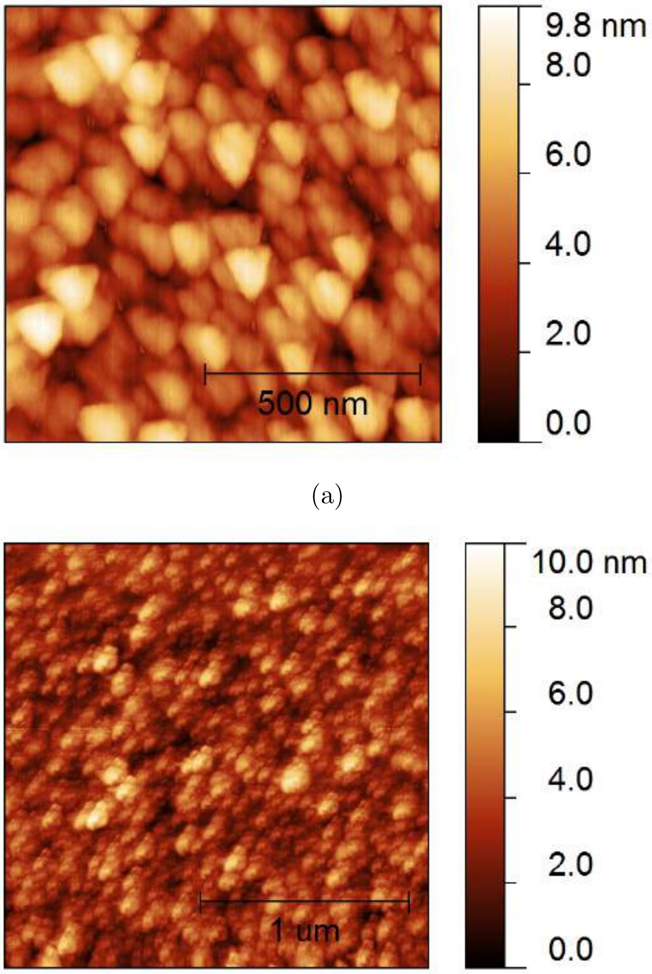

(a)

(b)

Figure 3.22: Artifacts due to the tip degradation Part 1. a) Common triangle artifact. b) “Picturesque” artifact.

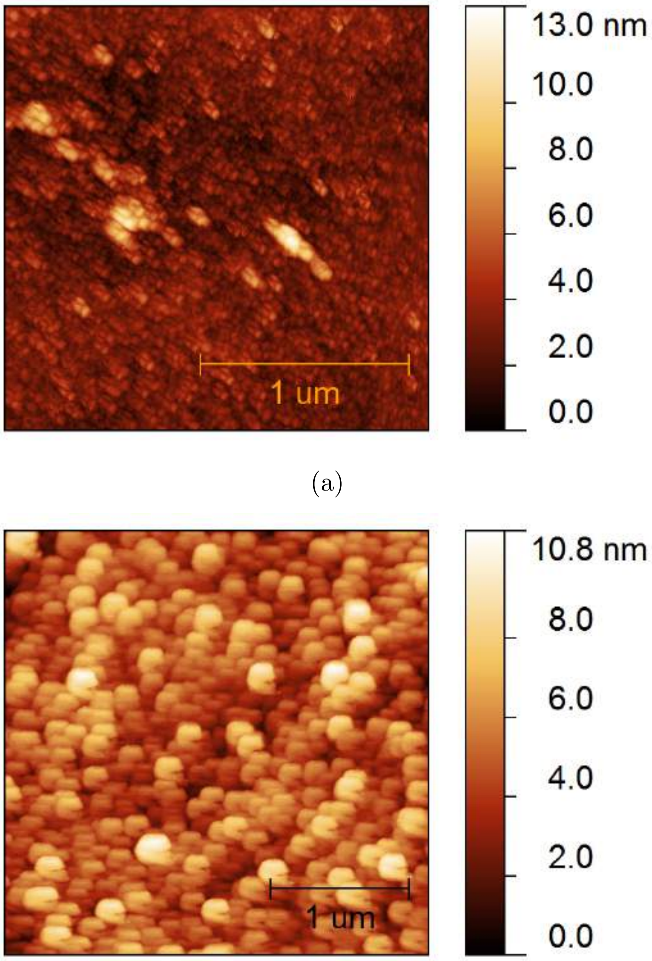

(a)

(b)

Figure 3.23: Artifacts due to the tip degradation Part 2. a) “Beetle” artifact. b) “Pacman” artifact.

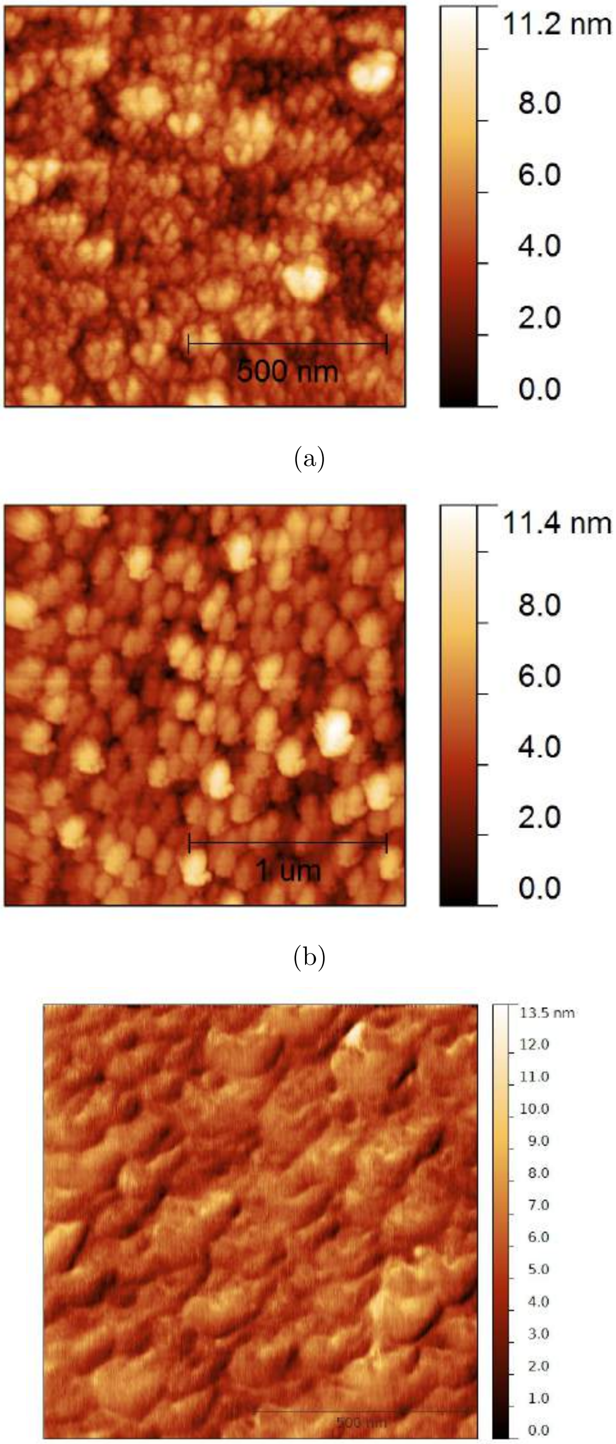

(a)

(b)

(c)

Figure 3.24: Artifacts due to the tip degradation Part 3. a) “Flower” doubling. b) “Popcorn” artifact. c) “Heart” artifact.

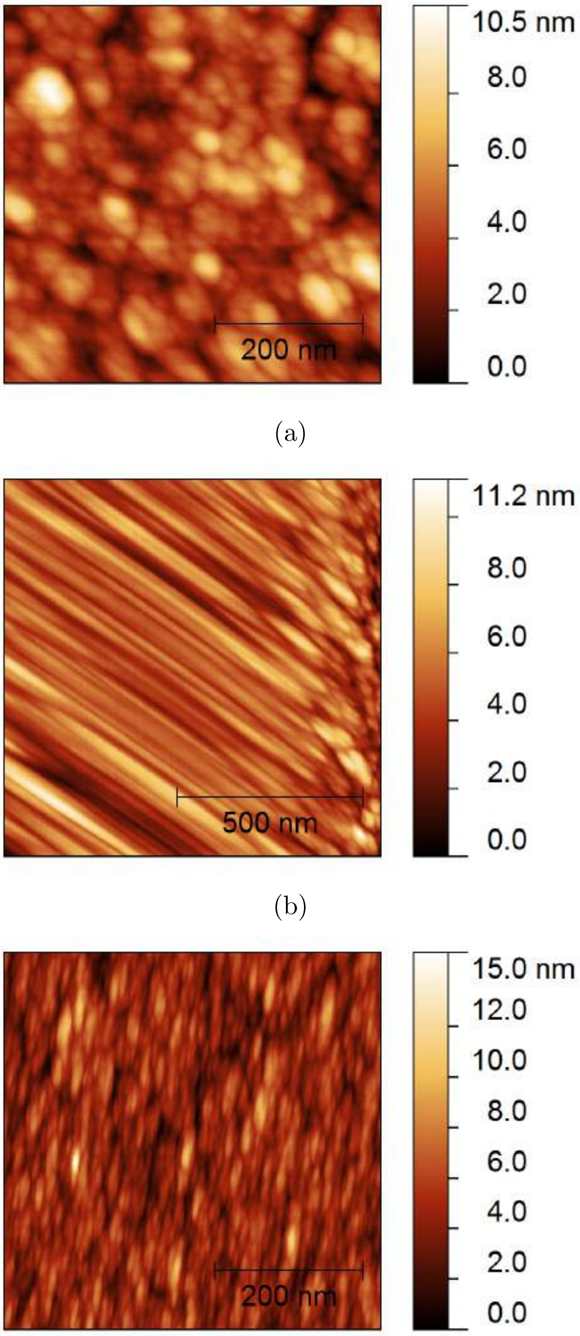

(a)

(b)

(c)

Figure 3.25: a) Common initial drift due to thermal effects. b) Exaggerated drift after few good lines of scanning. c) Slim grains along the y axis.

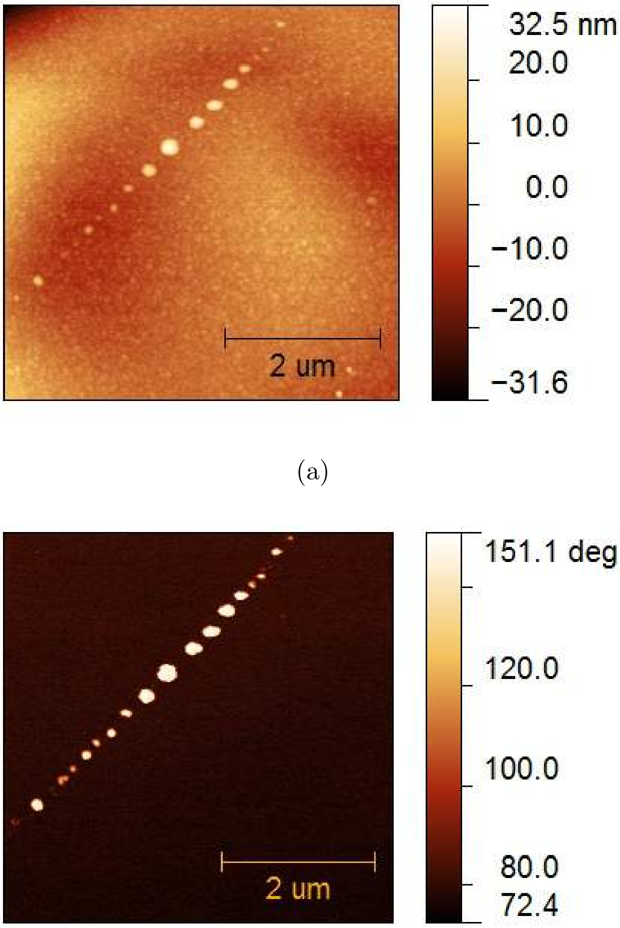

(a)

(b)

Figure 3.26: a) Height and b) phase maps in which a piece of dust has unfortunately met the AFM tip.

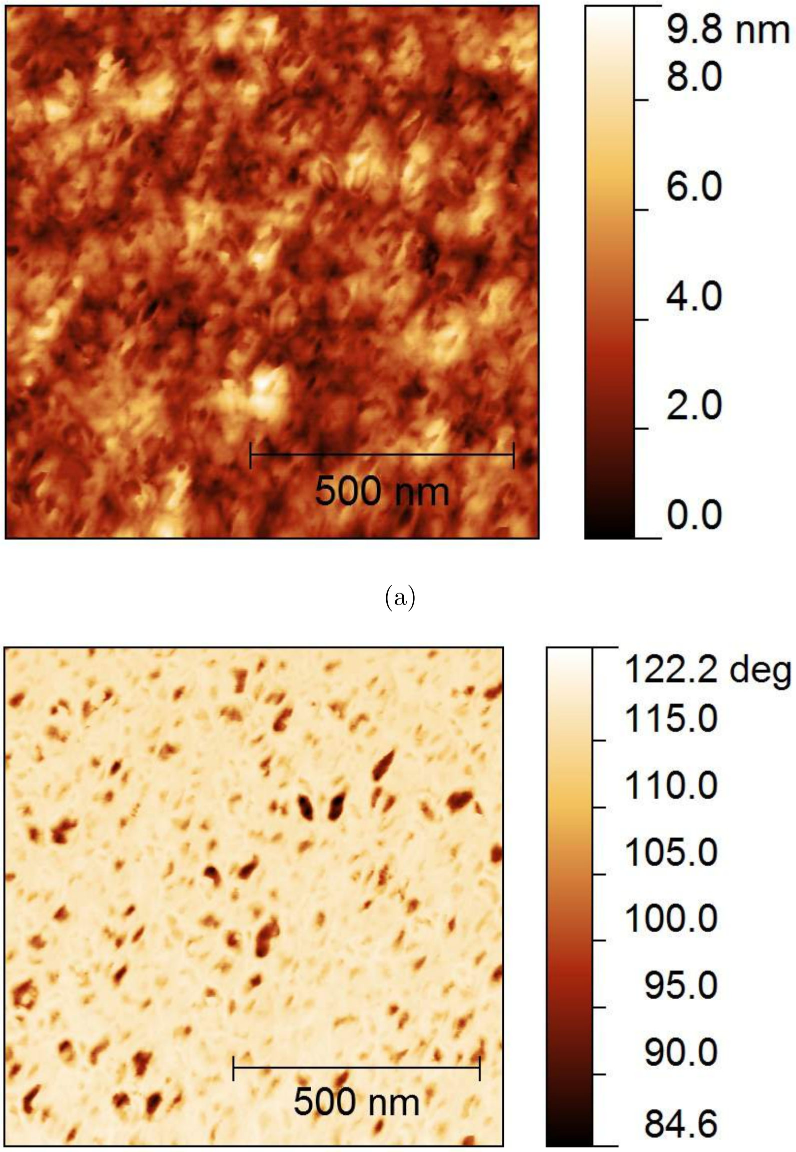

(a)

(b)

Figure 3.27: a) Height acquisition and b) its correspondent phase map with an instability of an “alien” shape.

Acknowledgements

Vorrei ringraziare le persone che mi sono state vicino in questo percorso.

Un sentito ringraziamento alla Professoressa Daniela Cavalcoli, che mi ha supportato costantemente con gentilezza e pazienza. Un ringraziamento va alla Photovoltaic Division del Department of Physics dell'University of Konstanz per la preparazione dei campioni da me studiati.

Un sentitissimo grazie alla Dottoressa Martina Perani per aver condiviso le sue conoscenze, aver supervisionato tutto il mio lavoro e per aver piacevolmente condiviso con me i lunghi tempi dedicati alle misure.

Vorrei ringraziare la mia famiglia e i miei amici, vicini e lontani, per avermi sostenuto emotivamente durante questi anni di universitá.

Infine, un ringraziamento particolare va a Lorenzo, per avermi aiutato a superare tutti i momenti difficili e essermi stato accanto pronto a consigliarmi ogni volta che ne avevo bisogno.

Bibliography

[1] L. Meyer, R. K. Pachauri, et al. *Climate Change 2014: Synthesis Report.* Cambridge University Press, 2015.

[2] M. Marquis and P. Tans. *A primer on climate change, in: Fundamentals of Materials for Energy and Environmental Sustainability.* ed. by D. S. Ginley and D. Cahen, Cambridge University Press, 2012.

[3] T. F. Stocker, D. Qin, G. K. Plattner, et al. *Climate Change 2013: The Physical Science Basis. Contribution of Working Group I to the Fifth Assessment Report of the Intergovernmental Panel on Climate Change.* Cambridge University Press, 2013.

[4] Q. Schiermeier et al. Energy alternatives: Electricity without carbon. *Nature*, (454):816 – 823, 2008.

[5] O. Edenhofer, R. P. Madruga, Y. Sokona, et al. *Renewable Energy Sources and Climate Change Mitigation: Special Report of the Intergovernmental Panel on Climate Change.* Cambridge University Press, 2012.

[6] S. De Wolf, A. Descoeudres, Z. C. Holman, and C. Ballif. High-efficiency Silicon Heterojunction Solar Cells: A Review. *Green*, 2:7 – 24, 2012.

[7] M. A. Green. Potential for low dimensional structures in photovoltaics. *Mater. Sci. Eng. B-Solid.*, (74):118 – 124, 2000.

[8] Panasonic HIT® Solar Cell Achieves World's Highest Energy Conversion Efficiency of 25.6% at Research Level. `http://news.panasonic.com/press/news/official.data/data.dir/2014/04/en140410-4/en140410-4.html`, 2014.

[9] N. Brinkmann, D. Sommer, G. Micard, G. Hahn, and B. Terheiden. Electrical, optical and structural investigation of plasma-enhanced chemical-vapor-deposited amorphous silicon oxynitride films for solar cell applications. *Sol. Energ. Mat. Sol. C.*, (108):180 – 188, 2013.

[10] A. Lambertz, V. Smirnov, T. Merdzhanova, K. Ding, S. Haasand G. Jost, R. Schropp, F. Finger, and U. Rau. Microcrystalline siliconoxygen alloys for application in silicon solar cells and modules. *Sol. Energy Mater. Sol. C*, (119):134 – 143, 2013.

[11] L.V. Mercaldo, P.D. Veneri, E.M. Esposito, I. Usatii, and R. Versace. Development of mixed phase p-SiO$_x$ by VHF-PECVD for thin film Si solar cells. *Proc. 28th EUPVSEC, Paris*, pages 2588 – 2591, 2014.

[12] T. Müeller, S. Schwertheim, and W.R. Fahrner. Crystalline silicon surface passivation by high-frequency plasma-enhanced chemical-vapor-deposited nano-composite silicon suboxides for solar cell applications. *J. Appl. Phys.*, (107):014504, 2010.

[13] S. Olibet. *Properties of interfaces in amorphous/crystalline silicon heterojunctions.* PhD thesis, Institut de Microtechnique Université de Neuchâtel, 2009.

[14] National Oceanic and Atmospheric Administration (NOOA). Greenhouse Gases. `http://www.ncdc.noaa.gov/monitoring-references/faq/greenhouse-gases.php`, 2015.

[15] European Renewable Energy Council (EREC). Renewable energy in Europe: markets, trends, and technologies, 2010.

[16] S. A. Mann, M. J. de Wild-Scholten, V. M. Fthenakis, W. G. J. H. M. van Sark, and W. C. Sinke. The energy payback time of advanced crystalline silicon PV modules in 2020: a prospective study. *Prog. Photovoltaics: Research and Applications*, 22:1180 – 1194, 2014.

[17] European Commission. Communication from the Commission to the European Parliament, the Council, the European Economic and Social Committee and the Committee of the regions: Energy technology developments beyond 2020 for the transition to a decarbonised European energy system by 2050, 2013.

[18] M. A. Green. *Solar Cells: Operating Principles, Technology, and System Applications.* Prentice Hall, Upper Saddle River, New Jersey 07458, 1982.

[19] J. Nelson. *The Physics of solar cells.* Imperial College Press, London, 2003.

[20] D. Ginley, M. A. Green, and R. Collins. Solar Energy Conversion Toward 1 Terawatt. `www.mrs.org/bulletin`, 2008.

[21] R. H. Bube. *Photovoltaic Materials.* Imperial College Press, London, 1998.

[22] `http://www.pvlighthouse.com.au/resources/courses/altermatt/The%20PV%20Principle/Voltage%20production.aspx`.

[23] N. W. Ashcroft and N. D. Mermin. *Solid State Physics.* Holt Rinehart & Winston, USA, 1976.

[24] E. H. Rhoderick and R. H. Williams. *Metal-Semiconductor Contacts.* Claredon Press, Oxford, 1988.

[25] W. Shockley and H. J. Queisser. Detailed Balance Limit of Efficiency of pn Junction Solar Cells. *J. Appl. Phys.*, 32:510 – 519, 1961.

[26] M. A. Green, K. Emery, Y. Hishikawa, and W. Warta. Solar cell efficiency tables (version 35). *Prog. Photovoltaics: Research and Applications*, 18:144 – 150, 2010.

[27] M. A. Green. *Third Generation Photovoltaics: Advanced Solar Energy Conversion.* Springer, Berlin, Heidelberg, New York, 2003.

[28] T. Saga. Advances in crystalline silicon solar cell technology for industrial mass production. *NPG Asia Mater.*, (2):96 – 102, 2010.

[29] T. Mishima, M. Taguchi, H. Sakata, and E. Maruyama. Development status of high-efficiency HIT solar cells. *Sol. Energ. Mat. Sol. C.*, 2010.

[30] `http://www.nrel.gov/ncpv/`, 2015.

[31] M. Perani, N. Brinkmann, A. Hammud, D. Cavalcoli, and B. Terheiden. Nanocrystal Formation in Silicon Oxy-Nitride Films for Photovoltaic Applications: Optical and Electrical Properties. *J. Phys. Chem. C*, (119):13907 – 13914, 2015.

[32] M. Perani, N. Brinkmann, M. A. Fazio, A. Hammud, B. Terheiden, and D. Cavalcoli. Annealing effects on SiOxNy thin films: optical and morphological properties. *Proceeding Thin Solid Films*, 2015, under review.

[33] R.M. De Ridder, K. Warhoff, A. Driessen, P.V. Lambeck, and H. Albers. Silicon oxynitride planar waveguiding structures for application in optical communication. *IEEE J. Sel. Topics Quantum Electron*, (4):930 – 937, 1998.

[34] K.J. Plucinski, I.V. Kityk, J. Kasperczyk, and B. Sahraoui. The structure and electronic properties of silicon oxynitride gate dielectrics. *Semicond. Sci. Technol.*, (16):467, 2001.

[35] R.J. Xie and N. Hirosaki. Silicon-based oxynitride and nitride phosphors for white LEDs-A review. *Sci. Tech. Adv. Mater.*, (8):588 – 600, 2007.

[36] S. Olibet, E. Vallat-Sauvain, L. Fesquet, C. Monachon, A. Hessler-Wyser, J. Damon-Lacoste, S. De Wolf., and C. Ballif. Properties of interfaces in amorphous/crystalline silicon heterojunctions. *Phys. Status Solidi A*, pages 1 – 6, 2010.

[37] `http://www.oxfordplasma.de/systems/100ll.htm`.

[38] J.-H. Park and T.S. Sudarshan. *Surface Engineering Series vol.2: Chemical Vapor Deposition.* ASM International, 2001.

[39] H. O. Pierson. *Handbook of Chemical Vapor Deposition: Principles, Technology, and Applications. Second Edition.* Noyes Publications, 1999.

[40] `http://www.oxford-instruments.com/products/etching-deposition-and-growth/plasma-etch-deposition/pecvd`.

[41] M. Perani. *Nanocrystalline Silicon Based Films for Renewable Energy Applications.* PhD thesis, University of Bologna, 2014.

[42] Y. Hishikawa, N. Nakamura, S. Tsuda, S. Nakano, Y. Kishi, and Y. Kuwuno. Interference-free determination of the optical absorption coefficient and the optical band gap of amorphous silicon thin films. *Jpn. J. Appl. Phys.*, (30):1008 – 1014, 1991.

[43] J. Tauc, R. Grigorovici, and A. Vancu. Optical properties and electronic structure of amorphous germanium. *Phys. Status Solidi*, (15):627 – 637, 1966.

[44] W. Scopel, R. Cuzinatto, M. Tabacniks, M. Fantini, M. Alayo, and I. Pereyra. Chemical and morphological properties of amorphous silicon oxynitride films deposited by plasma enhanced chemical vapor deposition. *J. Non-Cryst. Solids*, pages 88 – 95, 2001.

[45] K. Haga and H. Watanabe. A structural interpretation of Si-O-Si vibrational absorption of high-photoconductive amorphous a-SiOx:H films. *J. Non-Cryst. Solids*, (195):72 – 75, 1996.

[46] M. Perani, N. Brinkmann, M. A. Fazio, D. Cavalcoli, and B. Terheiden. EMRS Spring Meeting 2015 - Symposium C: Electrode distance induced changes in the growth of SiOxNy thin films for photovoltaic applications. `http://www.emrs-strasbourg.com`, May, 2015.

[47] P. Russell, D. Batchelor, and J. Thornton. SEM and AFM: Complementary Techniques for High Resolution Surface Investigations. *Digital Instruments/Veeco Metrology*, pages 1 – 12, 2004.

[48] G. Binnig and H. Roher. *Scanning Tunneling Microscopy - From birth to adolescence*. Nobel Lecture, 1986.

[49] `http://www.nobelprize.org/`.

[50] G. Binnig, C. F. Quate, and Ch. Gerber. Atomic Force Microscope. *Phys. Rev. Lett.*, (56):930 – 933, 1986.

[51] V. L. Mironov. *Fundamentals of scanning probe microscopy*. The Russian Academy of Sciences, 2004.

[52] B. Bhushan. *Handbook of Nanotechnology*. Springer, 2004.

[53] `http://www.ntmdt-tips.com/products/view/nsg10`.

[54] `http://www.ntmdt-tips.com/products/view/csg10-pt`.

[55] `https://www.brukerafmprobes.com/p-3774-rmn-25pt400b.aspxl`.

[56] `http://www.nanosensors.com/`.

[57] A. Cerreta. *Thesis: Surface Analysis with STM and AFM: Experimental and Theoretical Aspects of Image Analysis*. École Polytechnique Fédérale de Lausanne, 2013.

[58] `http://www.doitpoms.ac.uk/tlplib/afm/index.php`.

[59] R. García and R. Perez. Dynamic atomic force microscopy methods. *Surf. Sci. Rep.*, (47):197 – 301, 2002.

[60] R. García, R. Magerle, and R. Perez. Nanoscale compositional mapping with gentle forces. *Nature Mater.*, (6):405 – 411, 2007.

[61] `http://www.parkafm.com/index.php/park-spm-modes/standard-imaging-mode/217-true-non-contact-mode`.

[62] `http://www.parkafm.com/images/menu/afm\textunderscoretechnology/Non-Contact-AFM-vs.-Tapping-Mode-AFM.pdf`.

[63] NT-MDT. *INSTRUCTION MANUAL Solver PRO SPM.*

[64] S. N. Magonov and M.-H. Whangbo. *Surface Analysis with STM and AFM: Experimental and Theoretical Aspects of Image Analysis.* VCH, 1996.

[65] `http://www.ntmdt.com/spm-principles/`.

[66] `http://www.parkafm.com/index.php/company/news/press-release/`.

[67] `http://www.micro.feld.cvut.cz/home/34epo/cviceni/afm/nova.control\textunderscoreprogram.pdf`.

[68] `http://www.cim.unipr.it/html/XEP\textunderscore1\textunderscore7\textunderscore70manual[2010].pdf`.

[69] `http://gwyddion.net/download/user-guide/gwyddion-user-guide-en.pdf`.

[70] R. V. Gainutdinov and P. A. Arutyunov. Artifacts in Atomic Force Microscopy. *Russ. Microelectronics*, (30):219 – 224, 2001.

[71] F. M. Hoffman. An introduction to Fourier Theory. `http://www2.warwick.ac.uk/fac/sci/physics/research/cfsa/people/sandrac/lectures/basicfourierintro.pdf`.

[72] F. Detto. *Tesi: Silicio nanocristallino per applicazioni fotovoltaiche studiato mediante tecniche di Microscopia a Forza Atomica.* 2008.

[73] S. J. Fang, S. Haplepete, W. Chen, C. R. Helms, and H. Edwards. Analyzing atomic force microscopy images using spectral methods. *J. Appl. Phys.*, 82:5891 – 5898, 1997.

[74] M. Pelliccione and T. M. Lu. *Evolution of thin film morphology.* Springer, New York, 2007.

[75] Y. Zhao, G. C. Wang, and T. M. Lu. *Characterization of amorphous and crystalline rough surface: principles and applications.* Academic Press, San Diego, 2000.

[76] M. Perani, S. Carapezzi, G. R. Mutta, and D. Cavalcoli. Nanostructured Surfaces Investigated by Quantitative Morphological Studies. 2015, submitted.

[77] L. Vincent and P. Soille. Watershed in Digital Spaces: An Efficient Algorithm Based on Immersion Simulation. *IEEE Trans. Pattern Anal. Mach. Intell.*, 13:583 – 598, 1991.

[78] D. Cavalcoli, M. Rossi, A. Tomasi, and A. Cavallini. Degeneracy and instability of nanocontacts between conductive tips and hydrogenated nanocrystalline Si surfaces in conductive atomic force microscopy. *Nanotechnology*, (20):045702, 2009.

[79] A. Minj, D. Cavalcoli, A. Cavallini, P. Gamarra, and M.-A. di Forte Poisson. Strain distribution and defect analysis in III-nitrides by dynamical AFM analysis. *Nanotechnology*, (24):145701, 2013.

[80] B. Rezek, J. Stuchlík, A. Fejfar, and J. Kočka. Microcrystalline silicon thin films studied by atomic force microscopy with electrical current detection. *J. Appl. Phys.*, (92):587, 2002.

[81] A. Mattoni G. Fugallo. Thermally induced recrystallization of textured hydrogenated nanocrystalline silicon. *Phys. Rev. B*, (89):045301, 2014.